

Diplomarbeit

# Temperature Effects on the Stability and Mobility of DNA Origami Platforms and His-Tag pMHC on Supported Lipid Bilayers

zur Erlangung des akademischen Grades

Diplom-Ingenieur

im Rahmen des Studiums

Biomedical Engineering

ausgeführt am Institut für Angewandte Physik der Fakultät Physik

in der

Forschungsgruppe für Biophysik der Technische Universität Wien

unter der Anleitung von

Assoc. Prof. Dipl.-Ing.in Dr.in techn. Eva Sevcsik

und

Anežka Májková, MSc

durch

Georg Kögl, B.Eng.

Matrikelnummer: 12206170



Un

etreuer

Unterschrift Verfasser

Wien, 19.03.2026

# Zusammenfassung

Unterstützte Lipid-Doppelschichten (SLBs) bieten eine modulare und laterale Modellplattform für die Präsentation von membrangebundenen Liganden in rekonstituierten T-Zell-Aktivierungsassays. In dieser Arbeit wurde die zeitliche Stabilität der SLB-basierten Ligandenpräsentation für SLB-verankerte rechteckige DNA-Origami-Plattformen sowie Peptid-MHC-Komplexe (pMHC) untersucht. Die Experimente wurden bei 26 °C und 37 °C durchgeführt.

Die zeitliche Stabilität wurde über Beobachtungsfenster von ca. 120–200 Minuten nach dem Waschen der SLB-Wells analysiert, wobei in diesem Zeitraum drei bis vier Messungen pro SLB durchgeführt wurden. Mithilfe der zeitaufgelösten TIRF-Mikroskopie wurden (i) die laterale Diffusion mittels Einzelpartikelverfolgung und (ii) die normalisierte Gesamtfluoreszenzintensität als Proxy für die Oberflächenbedeckung quantifiziert. Darüber hinaus diente die Helligkeit einzelner Moleküle als Kontrollparameter für die Tracking-Qualität und potenzielle Aggregationseffekte.

Über alle Bedingungen hinweg blieben die Diffusionskoeffizienten innerhalb des Beobachtungsfensters zeitlich stabil, was darauf hindeutet, dass die Ligandenmobilität über die Zeit erhalten bleibt und dass auf experimentell relevanten Zeitskalen keine fortschreitende Immobilisierung oder kein Verlust der Membranfluidität auftritt. Die Gesamtfluoreszenzintensitäten waren entweder stabil oder zeigten nur allmähliche, gut auflösbare Veränderungen, was eher mit einer insgesamt robusten Oberflächenpräsentation als mit einem schnellen Ligandenverlust übereinstimmt. Außerdem spricht das Fehlen ausgeprägter zeitabhängiger Helligkeitszunahmen gegen erhebliche aggregationsbedingte Artefakte und für die Zuverlässigkeit der Mobilitätsmessungen.

Zusammen zeigen diese Ergebnisse, dass die untersuchten SLB-basierten Membransysteme unter den getesteten Bedingungen eine ausreichend stabile und lateral mobile Ligandenpräsentation über die für Folgeexperimente relevanten Zeitskalen bieten. Diese zeitliche Robustheit untermauert ihre Eignung als standardisierte Plattformen für T-Zell-Aktivierungsassays, bei denen kontrollierte Oberflächendichten und anhaltende Ligandenmobilität unerlässlich sind, um Aktivierungsschwellen und die Bildung immunologischer Synapsen unter physiologisch relevanten Bedin-

gungen zu untersuchen.

# Abstract

Supported lipid bilayers (SLBs) provide a modular, laterally fluid biointerface for presenting membrane-tethered ligands in reconstituted T cell activation assays. In this thesis, the temporal stability of SLB-based ligand presentation was assessed for SLB-anchored rectangular DNA origami platforms as well as peptide-MHC (pMHC) complexes. Experiments were performed at 26 °C and 37 °C.

Temporal stability was analyzed over observation windows of approximately 120-200 minutes following washing of SLB-wells, with typically three to four measurements acquired per SLB during this time period. Time-resolved TIRF microscopy was used to quantify (i) lateral diffusion via single-particle tracking and (ii) normalized bulk fluorescence intensity as a proxy for surface coverage. In addition, single-molecule brightness served as a control metric for tracking quality and potential aggregation effects.

Across conditions, diffusion coefficients remained temporally stable within the observation window, indicating that ligand mobility is preserved over time and that no progressive immobilization or loss of membrane fluidity occurs on experimentally relevant timescales. Bulk fluorescence intensities were either stable or showed only gradual, well-resolved changes, consistent with overall robust surface presentation rather than rapid ligand depletion. Importantly, the absence of pronounced time-dependent brightness increases argues against substantial aggregation-driven artifacts, supporting the reliability of the mobility measurements.

Together, these results demonstrate that the investigated SLB-based membrane systems provide sufficiently stable and laterally mobile ligand presentation over the timescales relevant for downstream experiments in tested conditions. This temporal robustness supports their suitability as standardized platforms for T cell activation assays, where controlled surface densities and sustained ligand mobility are essential to probe activation thresholds and immunological synapse formation under physiologically relevant conditions.

# Acknowledgements

This thesis marks an important milestone in my academic path. I have gained a great deal of knowledge while working on this project, and it would not have been achievable without the support of several people.

First and foremost, I would like to thank Eva Sevcsik for giving me the chance to conduct my thesis within the Biophysics Group; without you, this work would not have been possible. I would also like to extend my profound gratitude to Anežka Májková, who welcomed me into the Microbiology Lab, taught me the microscopy, and patiently helped me with my countless questions. Thank you sincerely for leading me through my research, for the many thought-provoking discussions, your valuable feedback, and your warm and attentive supervision.

Furthermore, I would like to thank the rest of the Biophysics Group for welcoming me into your team and for creating such an enjoyable working atmosphere.

Finally, I want to thank my dear friend, Paula Gürtler, for proofreading my thesis, and all my other friends and family who provided much needed moral support.

# Eidesstattliche Erklärung

Ich erkläre an Eides statt, dass die vorliegende Arbeit nach den anerkannten Grundsätzen für wissenschaftliche Abhandlungen von mir selbstständig erstellt wurde. Alle verwendeten Hilfsmittel, insbesondere die zugrunde gelegte Literatur, sind in dieser Arbeit genannt und aufgelistet. Die aus den Quellen wörtlich entnommenen Stellen sind als solche kenntlich gemacht. Das Thema dieser Arbeit wurde von mir bisher weder im In- noch Ausland einer Beurteilerin/einem Beurteiler zur Begutachtung in irgendeiner Form als Prüfungsarbeit vorgelegt. Diese Arbeit stimmt mit der von den Begutachterinnen/Begutachtern beurteilten Arbeit überein.

Wien, 19.03.2026

---

Unterschrift Verfasser

# Contents

<b>Zusammenfassung</b>	<b>ii</b>
<b>Abstract</b>	<b>iv</b>
<b>Acknowledgements</b>	<b>v</b>
<b>Eidesstattliche Erklärung</b>	<b>vi</b>
<b>List of Figures</b>	<b>xi</b>
<b>List of Tables</b>	<b>xii</b>
<b>List of Abbreviations</b>	<b>xiii</b>
<b>1. Introduction</b>	<b>1</b>
<b>2. Theoretical Background</b>	<b>3</b>
2.1. Model Systems for T cell activation . . . . .	3
2.1.1. Membranes as model systems for ligand presentation . . . . .	3
2.1.2. Peptide-MHC complexes in reconstituted T cell activation assays	5
2.2. Biointerface engineering: supported membranes and DNA origami . .	8
2.2.1. Supported lipid bilayers . . . . .	8
2.2.2. DNA origami platforms for nanoscale ligand presentation . . .	13
2.3. Total Internal Reflection Fluorescence Microscopy . . . . .	16
2.3.1. Principle and surface selectivity . . . . .	16
2.3.2. Single Particle Tracking . . . . .	18
2.4. Biophysical readouts of SLB-based biointerfaces . . . . .	18
2.4.1. Lateral diffusion of membrane-tethered objects . . . . .	18
2.4.2. Fluorescence intensity as a proxy for surface density and bind- ing persistence . . . . .	19
2.4.3. Determinants and temperature dependence . . . . .	20

<b>3. Material and Methods</b>	<b>21</b>
3.1. DNA Origami . . . . .	21
3.1.1. DNA Origami Folding . . . . .	22
3.1.2. DNA Origami Purification . . . . .	22
3.2. pMHC complex . . . . .	22
3.3. Supported Lipid Bilayer Formation . . . . .	23
3.3.1. Vesicle Formation . . . . .	23
3.3.2. Bilayer Formation . . . . .	23
3.4. SLB Functionalization . . . . .	23
3.4.1. Functionalization of SLBs with pMHC Molecules . . . . .	23
3.4.2. Functionalization of SLBs with DNA origami Platforms . . . . .	24
3.5. Single-Molecule TIRF Imaging . . . . .	24
3.6. Experimental design and statistical units . . . . .	25
3.6.1. Single molecule localization and quantification of single-molecule brightness . . . . .	27
3.6.2. Quantification of Fluorophore Diffusion Changes . . . . .	28
3.6.3. Quantification of Temporal Fluorescence Intensity Changes . . . . .	30
<b>4. Results</b>	<b>32</b>
4.1. Temperature dependence of lateral diffusion . . . . .	32
4.1.1. L2V . . . . .	32
4.1.2. L1V . . . . .	35
4.1.3. pMHC . . . . .	37
4.2. Temporal stability of intensity . . . . .	39
4.2.1. L2V . . . . .	40
4.2.2. L1V . . . . .	41
4.2.3. pMHC . . . . .	42
4.3. Temporal trends in single-molecule brightness . . . . .	43
4.3.1. L2V . . . . .	44
4.3.2. L1V . . . . .	45
4.3.3. pMHC . . . . .	46
<b>5. Discussion</b>	<b>48</b>
5.1. Surface Density of Ligands . . . . .	48
5.1.1. L2V . . . . .	48
5.1.2. L1V . . . . .	49
5.1.3. pMHC . . . . .	49

5.2.	Lateral mobility and functional presentation . . . . .	49
5.2.1.	L2V . . . . .	49
5.2.2.	L1V . . . . .	50
5.2.3.	pMHC . . . . .	50
5.3.	Integrated interpretation of surface presentation and mobility . . . . .	50
5.4.	Methodological considerations and quality control . . . . .	51
5.4.1.	Quality control: single-molecule brightness . . . . .	51
5.4.2.	Excitation stability and normalization of intensity trends . . . . .	51
5.4.3.	Determination of ligand surface densities . . . . .	52
5.4.4.	Verification of sample temperature . . . . .	52
<b>6.</b>	<b>Conclusion &amp; Outlook</b>	<b>54</b>
6.1.	Conclusion . . . . .	54
6.2.	Outlook . . . . .	55
<b>A.</b>	<b>Supplementary Material</b>	<b>63</b>
A.1.	Temperature Plots . . . . .	63
A.2.	Laser Power Plots . . . . .	64
A.3.	Mean Single-Molecule Brightness Tables . . . . .	65
A.3.1.	26 Degrees . . . . .	65
A.3.2.	37 Degrees . . . . .	67
A.4.	DNA Origami Mixing Tables . . . . .	68
A.4.1.	L2V . . . . .	68
A.4.2.	L1V . . . . .	69
A.5.	Surface Density Plots at $t(0)$ . . . . .	70
A.5.1.	26 Degrees . . . . .	70
A.5.2.	37 Degrees . . . . .	73
A.5.3.	pMHC . . . . .	75
<b>B.</b>	<b>Use of AI</b>	<b>76</b>

# List of Figures

2.1.	Two views of a cell membrane. . . . .	4
2.2.	Recognition by T cells of peptides bound to MHC proteins. . . . .	6
2.3.	Structural organization of MHC class I and class II molecules . . . . .	7
2.4.	Schematic diagram of a solid supported phospholipid bilayer. . . . .	9
2.5.	Mechanisms of vesicle rupture . . . . .	10
2.6.	Chemical structures of lipids commonly used for supported lipid bi- layers. . . . .	11
2.7.	Complex formation of a poly-His tag with Ni-NTA . . . . .	12
2.8.	Chemical structures of cholesteryl-TEG and cholesterol. . . . .	13
2.9.	Self assembly of DNA origami. . . . .	14
2.10.	DNA origami platform 3D rendering. . . . .	15
2.11.	DNA origami layouts for nanoscale ligand presentation . . . . .	15
2.12.	Schematic representation of total internal reflection fluorescence (TIRF) microscopy . . . . .	17
4.1.	Absolute diffusion coefficients $D(t)$ for L2V DNA origami platforms at 26 °C and 37 °C. . . . .	33
4.2.	Trajectory-level mobility-class population fractions for L2V at 26 °C across all supported lipid bilayers. . . . .	34
4.3.	Trajectory-level mobility-class population fractions for L2V at 37 °C across all supported lipid bilayers. . . . .	35
4.4.	Absolute diffusion coefficients $D(t)$ for L1V DNA origami platforms at 26 °C and 37 °C. . . . .	36
4.5.	Diffusion population trends of L1V at 26 °C across all supported lipid bilayers. . . . .	36
4.6.	Diffusion population trends of L1V at 37 °C across all supported lipid bilayers. . . . .	37
4.7.	Absolute diffusion coefficients $D(t)$ for pMHC molecules at 26 °C and 37 °C. . . . .	38
4.8.	Diffusion population trends of pMHC at 26 °C across all supported lipid bilayers. . . . .	38

4.9. Diffusion population trends of pMHC at 37 °C across all supported lipid bilayers. . . . .	39
4.10. Pictures of SLB2 seeded with 400 ng L2V at 37 °C over time on 10.10.2025. . . . .	40
4.11. Normalized bulk fluorescence intensity $I_{\text{rel}}(t)$ for L2V DNA origami platforms at 26 °C and 37 °C. . . . .	41
4.12. Normalized bulk fluorescence intensity $I_{\text{rel}}(t)$ for L1V DNA origami platforms at 26 °C and 37 °C. . . . .	42
4.13. Normalized bulk fluorescence intensity $I_{\text{rel}}(t)$ for pMHC molecules at 26 °C and 37 °C. . . . .	43
4.14. Pictures of SLB1 seeded with 20 ng L2V at 26 °C over time on 09.10.2025. . . . .	44
4.15. Mean single molecule brightness $I_{\text{SM}}$ of L2V DNA origami platforms at 26 °C and 37 °C. . . . .	45
4.16. Mean single molecule brightness $I_{\text{SM}}$ of L1V DNA origami platforms at 26 °C and 37 °C. . . . .	46
4.17. Mean single molecule brightness $I_{\text{SM}}$ of pMHC at 26 °C and 37 °C. . . . .	47
A.1. Sample temperatures measured for the experiments with L2V and pMHC. . . . .	63
A.2. Sample temperatures measured for the experiments with L1V. . . . .	64
A.3. Surface power density of laser light in relation to the attenuation at the 02.12.2025. . . . .	64
A.4. Surface power density of laser light in relation to the attenuation at the 04.12.2025. . . . .	65
A.5. Estimated initial surface density $\rho(t_0)$ for L2V bulk fluorescence wells at 26 °C across imaged positions. . . . .	70
A.6. Estimated initial surface density $\rho(t_0)$ for L1V bulk fluorescence wells at 26 °C across imaged positions. . . . .	71
A.7. Estimated initial surface density $\rho(t_0)$ for pMHC bulk fluorescence wells at 26 °C across imaged positions. . . . .	72
A.8. Estimated initial surface density $\rho(t_0)$ for L2V bulk fluorescence wells at 37 °C across imaged positions. . . . .	73
A.9. Estimated initial surface density $\rho(t_0)$ for L1V bulk fluorescence wells at 37 °C across imaged positions. . . . .	74
A.10. Estimated initial surface density $\rho(t_0)$ for pMHC bulk fluorescence wells at 37 °C across imaged positions. . . . .	75

# List of Tables

3.1. Overview of measurement days and well allocation for L2V and pMHC.	27
3.2. Overview of measurement days and well allocation for L1V. . . . .	27
A.1. Mean single-molecule brightness values for L2V at 26 °C. . . . .	65
A.2. Mean single-molecule brightness values for L1V at 26 °C. . . . .	66
A.3. Mean single-molecule brightness values for pMHC at 26 °C. . . . .	66
A.4. Mean single-molecule brightness values for L2V at 37 °C. . . . .	67
A.5. Mean single-molecule brightness values for L1V at 37 °C. . . . .	67
A.6. Mean single-molecule brightness values for pMHC at 37 °C. . . . .	68
A.7. DNA origami mixing platform L2V . . . . .	68
A.8. DNA origami mixing platform L1V . . . . .	69

# List of Abbreviations

**AF647** Alexa Fluor™ 647

**APC** Antigen-presenting cell

**CDR** Complementarity-determining regions

**Cholesteryl-TEG** Cholesteryl-tri(ethylene glycol)

**CMVpp65** 65 kDa phosphoprotein of human cytomegalovirus

**DNA** Deoxyribonucleic acid

**DPBS** Dulbecco's phosphate-buffered saline

**EDTA** Ethylenediaminetetraacetic acid

**FoB** Folding buffer

**FRAP** Fluorescence recovery after photobleaching

**H-2K<sup>k</sup>** Murine MHC class I molecule H-2K<sup>k</sup>

**His tag** Polyhistidine tag

**HLA-A\*02:01** Human leukocyte antigen A\*02:01

**I-E<sup>k</sup>** Murine MHC class II molecule I-E<sup>k</sup>

**IMAC** Immobilized metal affinity chromatography

**LTC** Lab-Tek chamber

**MgCl<sub>2</sub>** Magnesium chloride

**MSD** Mean square displacement

**NaCl** Sodium chloride

**Ni-DGS-NTA** 1,2-dioleoyl-sn-glycero-3-[(N-(5-amino-1-carboxypentyl)iminodiacetic acid)succinyl] nickel salt

**PC** Phosphatidylcholine

**POPC** 1-palmitoyl-2-oleoyl-sn-glycero-3-phosphocholine

**PuB** Purification buffer

**SLB** Supported lipid bilayer

**SPT** Single-particle tracking

**ssDNA** Single-stranded deoxyribonucleic acid

**TIRF** Total internal reflection fluorescence

**Tris** Tris(hydroxymethyl)aminomethane

# 1. Introduction

The human body protects itself against harmful pathogens such as viruses and bacteria through a complex collection of cells and proteins working together, the immune system [1]. Specificity to an antigen in the adaptive immune system is provided by lymphocytes expressing a highly diverse set of antigen receptors that enable recognition of a broad range of pathogens [2]. T cells are a primary type of lymphocyte and recognize antigens through their membrane-bound T cell receptor (TCR) [3]. T cells are involved in most immune responses and their activation therefore represents a critical step in adaptive immunity [3].

While numerous studies have examined the process of T cell activation, the molecular mechanisms governing how T cells translate TCR engagement into activation remain an area of ongoing investigation [4]. In order to study these mechanisms under controlled conditions, several types of reconstituted model systems have been developed. Among these are experimental systems based on SLBs, which mimic essential physical characteristics of cell–cell interfaces and enable the presentation of ligands in a membrane-tethered and laterally mobile configuration [5], [6], [7].

Within the broader project in which this thesis is embedded, model membranes based on SLBs are used as modular biointerfaces on which different ligands can be presented to support downstream T cell activation assays [5], [6]. In the experiments considered here, SLBs consist of 98 % POPC and 2 % Ni-DGS-NTA lipids, providing a fluid membrane platform that allows membrane-tethered ligands to remain laterally mobile. Peptide–major histocompatibility complex (pMHC) molecules are attached to the bilayer via a polyhistidine tag that binds to Ni-DGS-NTA lipids. Besides pMHC complexes as the cognate ligand for the T cell receptor, SLB-anchored DNA origami nanostructures, which are tethered to the membrane through cholesterol modifications, are employed within the same assay framework. In particular, rectangular monovalently and bivalently fluorescently labeled DNA origami platforms (called L1V and L2V in this thesis) are used to organize pMHC molecules with nanoscale control on SLBs in T cell activation model systems [5], [6], [8].

For such experiments it is essential that the underlying membrane platform and the attached ligand modules form a stable and reproducible test system, because

the stability of the interface defines the baseline for interpreting ligand-density- or spacing-dependent effects. Earlier work in the project relied on murine MHC class II pMHC (I-E<sup>k</sup>) variants [9]; in contrast, the present work uses human MHC class I pMHC (HLA-A\*02:01). This change motivates renewed validation that these complexes can be incorporated into SLBs and presented reliably over experimentally relevant time scales and under different temperature conditions.

In addition, the stability of SLB-anchored DNA origami-based interfaces has not yet been systematically assessed in this experimental context. Since extended T cell activation assays require stable ligand presentation over long observation periods and may be performed at physiological temperature, it is necessary to verify that both the membrane platform and the different ligand modules remain stable under such conditions. In the present work, experiments are therefore conducted at 26 °C and 37 °C in 1× DPBS buffer, or in 1× DPBS supplemented with 10 mM MgCl<sub>2</sub> for DNA origami samples. Temporal stability is assessed over observation windows of approximately 120-200 minutes following washing of the SLB, during which typically three to four measurements are acquired per bilayer.

Accordingly, the present thesis focuses on establishing and validating the physical performance and stability of SLB-based membrane systems under conditions relevant for extended activation assays. Specifically, three systems are characterized as baseline platforms: SLB+pMHC, SLB+L1V, and SLB+L2V.

The work addresses the following research questions:

1. Do SLB-based membrane systems maintain stable lateral diffusion of membrane-tethered ligands over experimentally relevant timescales?
2. Does the ligand surface density remain stable over time under the investigated experimental conditions?

By addressing these questions, this work provides a defined and reproducible starting point for subsequent T cell activation studies, including assays that exploit DNA origami platforms for nanoscale ligand organization.

## 2. Theoretical Background

### 2.1. Model Systems for T cell activation

#### 2.1.1. Membranes as model systems for ligand presentation

Biological membranes are essential for cellular life. They regulate the transport of ions and molecules between the interior and exterior of the cell, the exchange of information and participate in a wide range of cellular processes. Biological membranes are highly fluid, complex and dynamic structures. A two-dimensional matrix of lipid molecules, arranged in a continuous bilayer approximately 5 nm thick and stabilized by hydrophobic interactions constitutes the scaffold of the membrane. This lipid bilayer acts as an effective barrier to the passage of most water-soluble molecules [3].

Cellular membranes contain a diverse set of proteins that mediate nearly all specific membrane functions in addition to lipids. They catalyze biochemical reactions, facilitate selective transport across the lipid bilayer and enable cells to sense and respond to stimuli. Membrane receptors in particular transmit information rather than material across the membrane, allowing cells to adapt their behavior to changes in their environment or signals from other cells [3]. The structure of a cell membrane can be seen in Fig. 2.1.

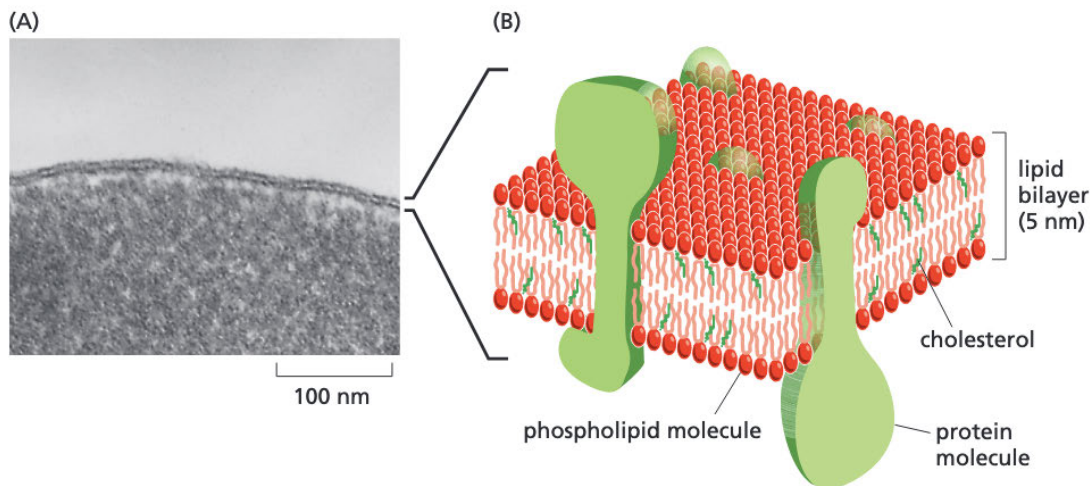


Figure 2.1.: **Two views of a cell membrane.** (A) An electron micrograph of a segment of the plasma membrane of a human red blood cell seen in cross section, showing its bilayer structure. (B) A three-dimensional schematic view of a cell membrane and the general disposition of its lipid and protein constituents. Adapted from [3].

Membranes are highly diverse in their composition, even within the same cell and their structure is dynamically adaptable to support processes such as molecular recognition, signaling and trafficking. Given their importance and their high complexity, a wide variety of model membrane systems had been developed. These model membrane systems aim to preserve the essential lipid-bilayer structure while simplifying the overall system. This strategy enables the investigation of individual components and the study of their organization and dynamics [10].

Model membrane systems span a broad design space that includes free-standing lipid vesicles, membranes on solid supports, and free-standing membranes. By choosing a specific architecture, different aspects of membrane structure and dynamics can be probed under controlled experimental conditions [10]. Solid-supported membranes in particular have attracted increasing interest, as they are compatible with surface-sensitive characterization techniques, advanced surface patterning approaches, and microfluidic liquid handling [11].

The investigation of membrane proteins function requires controlled model environments, because the membrane context strongly influences their physical behavior [12]. But not all protein classes can be used equally straight forward in every model architecture. A major limitation of solid-supported planar bilayers is the incorporation of transmembrane proteins, as their embedding through the membrane can lead to interactions with the underlying support, hindering lateral mobility and

impairment of the function [10].

### 2.1.2. Peptide-MHC complexes in reconstituted T cell activation assays

One use of these membrane model systems is to recreate the membrane interface of antigen presenting cells (APCs), which in turn enables the study of subsequent T cell activation in reconstituted assays [5], [6].

#### Peptide-MHC and T cell activation

Peptide-major histocompatibility complex (pMHC) molecules are membrane-bound ligand complexes that enable T cells to detect antigens. T cells recognize short antigenic peptide fragments displayed on MHC molecules on the surface of APCs. These peptides can originate either from intracellular proteins (like pathogen-derived proteins in infected cells) or from material that has been taken up by the APC from the extracellular matrix. In particular dendritic cells, which constitute a specific kind of APC, process such material and present peptide fragments at the plasma membrane [3], [13]. The peptide forms a complex with major histocompatibility complex (MHC) molecules, which are specialized host glycoproteins that transport peptide fragments to the cell surface and present them for T cell inspection [13].

T cell recognition of pMHC is facilitated by the T cell receptor (TCR), a membrane-spanning heterodimer composed of an  $\alpha$  chain paired with a  $\beta$  chain in most T cells. Extracellular variable and constant domains constitute each chain, hypervariable complementarity determining regions (CDRs) form the antigen-binding site that contacts the peptide-MHC complex [13]. Simultaneously, TCR co-receptors bind to MHC. The two main types of co-receptors are called CD4 and CD8. CD4 is present on both helper and regulatory T cells, while CD8 is present on cytotoxic T cells [3]. In summary, pMHC is the membrane-presented ligand for the TCR, and T cell recognition requires the formation of a ternary interface between MHC, peptide, and TCR. pMHC and TCR binding is shown conceptually in Fig. 2.2.

Two main MHC classes can be classified based on the origin of presented peptides and structure. As summarized in Fig. 2.3, class I MHC proteins predominantly present endogenous peptides, interact with CD8 co-receptors and consist of a transmembrane  $\alpha$  chain noncovalently associated with  $\beta_2$ -microglobulin, whereas class II MHC proteins present predominantly exogenous peptides, interact with CD4 co-receptors and form heterodimers of a noncovalently associated  $\alpha$  and  $\beta$  chain, each contributing an extracellular domain to the peptide-binding groove [3]. In vivo,

MHC molecules are therefore trans-membrane proteins, which poses a challenge for incorporation into supported bilayers (as mentioned in 2.1.1). In this thesis, pMHC class I complexes based on HLA-A\*02:01 (MHC) loaded with the CMV pp65-derived peptide were used as membrane-tethered ligands. To bypass the limitations of the normally trans-membrane molecules, recombinant pMHC carrying a C-terminal 12×His tag are used to enable reversible and oriented coupling to the surface of Ni<sup>2+</sup>-NTA-functionalized supported lipid bilayers (SLBs) (see Sec. 2.2.1).

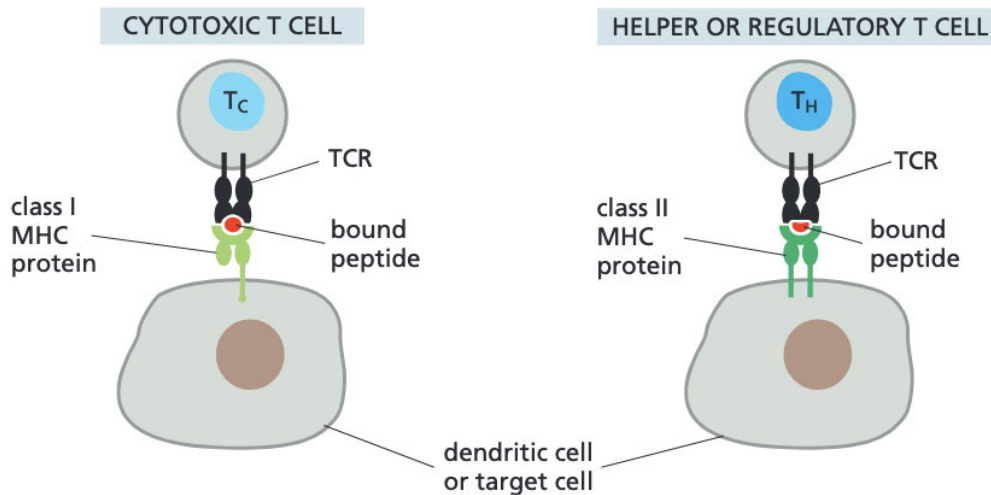


Figure 2.2.: **Recognition by T cells of peptides bound to MHC proteins.** Cytotoxic T ( $T_C$ ) cells recognize foreign peptides in association with class I MHC proteins, whereas helper T ( $T_H$ ) cells recognize foreign peptides in association with class II MHC proteins; regulatory T cells also recognize self or foreign peptides in association with class II MHC proteins. In all cases, the T cell recognizes the peptide–MHC complexes on the surface of an APC—either a dendritic cell or a target cell. Different types of dendritic cells activate naïve cytotoxic and helper T cells (not shown). Adapted from [3]

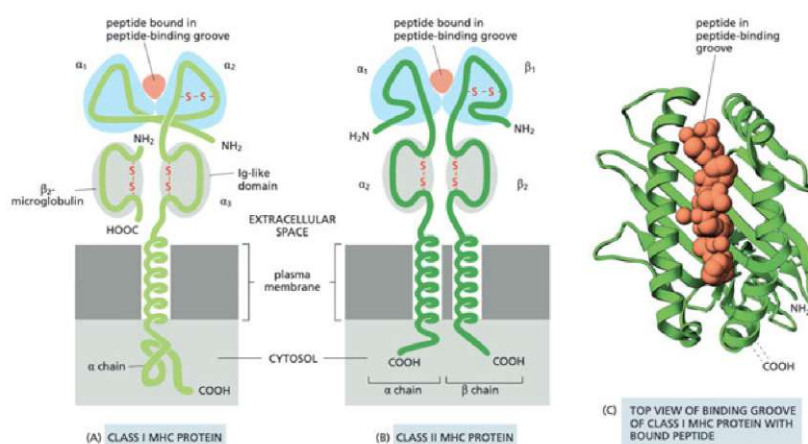


Figure 2.3.: **Structural organization of MHC class I and class II molecules.** Class I MHC proteins comprise a transmembrane  $\alpha$  chain associated with  $\beta_2$ -microglobulin, whereas class II MHC proteins are heterodimers of an  $\alpha$  and  $\beta$  chain that jointly form the peptide-binding groove. In this thesis, pMHC complexes of the MHC class I type were used. Adapted from [3].

### Use in Immunological Assays

Membrane-presented MHC ligands on planar bilayers have been a widely used model system in immune cell recognition research [14]. Planar bilayers simulate key aspects of membrane-based ligand presentation at cell-cell interfaces [14]. Early work by Brian and McConnell demonstrated that supported planar membranes functionalized with class I MHC (H-2K<sup>k</sup>) can activate cytotoxic T lymphocytes in vitro [15]. In this system, the amount of incorporated MHC could be tuned precisely via the lipid-to-protein ratio during vesicle production, which are then in turn used for forming planar bilayers [15].

Using SLBs as model for APC's membrane have been particularly powerful for studying T cell activation because they convert the inherently three-dimensional interaction environment into a two-dimensional contact zone. This dimensional reduction subsequently simplifies the detection of rapid, transient events, such as TCR-pMHC interactions, that are difficult to capture in 3D contexts [4]. SLBs provide experimental control over the surface density, identity, and mobility of membrane-tethered ligands like pMHC, while preserving the stimulatory potency of them [8], [16]. Imaging in two dimensions also enhances spatiotemporal resolution, enabling noninvasive single-molecule visualization compared to imaging in three dimensions [8]. These SLB-based model systems are highly compatible with TIRF microscopy, which selectively excites fluorophores within a small area at an interface (like glass slides), strongly reducing background noise [16], [17]. Impor-

tantly, such SLB-based assays enable the study of key physical aspects of signaling at cell-cell interfaces (2D presentation, lateral mobility, and emergent spatial organization), while reducing the native membrane complexity that can otherwise cloud quantitative interpretation [16]. SLBs and TIRF will be discussed in more detail in section 2.2.1 and 2.3 respectively.

DNA origami nanostructures provide an additional component to SLBs for presenting pMHC ligands with defined nanoscale geometry. By acting as rigid, laterally mobile scaffolds embedded in SLBs, DNA origami enables site-specific coupling of pMHC complexes and enable the spacing between ligands to be set with nanometer precision [8]. This makes it possible to directly relate the spatial position of membrane-tethered pMHC to TCR coupling and downstream T cell activation in reconstituted assays [8]. DNA origami will be further discussed in section 2.2.2.

## 2.2. Biointerface engineering: supported membranes and DNA origami

### 2.2.1. Supported lipid bilayers

As mentioned previously, SLBs are among the most common types of membrane systems that have been designed to model cellular membranes [11], [18].

SLBs consist of a complete phospholipid bilayer which is positioned onto the top of a hydrophilic solid support; i.e., quartz, glass, or oxidized silicon. These structures can mimic many of the properties of biologic membranes. For example, they can present proteins on their surface, while keeping them laterally mobile in the liquid bilayer. This lateral fluidity is facilitated by a 10-20 Å thick interstitial water layer located between the lower leaflet of the bilayer and the solid substrate. SLBs serve as a robust and modifiable platform for ligand presentation that may be analyzed using a number of different surface-sensitive methodologies, including fluorescence microscopy and atomic force microscopy [18], [19], [20]. The structural arrangement of an SLB is depicted in Figure 2.4.

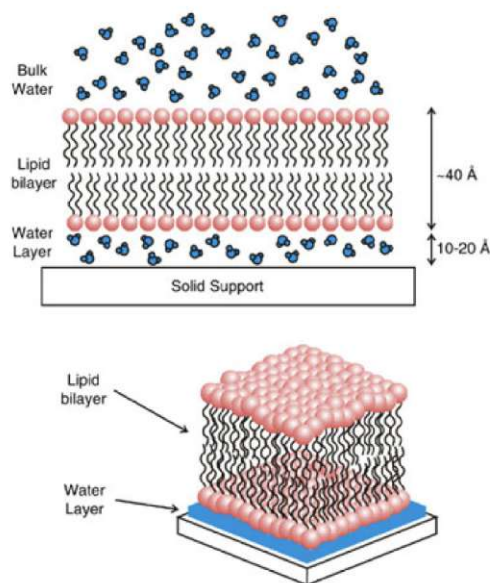


Figure 2.4.: **Schematic diagram of a solid supported phospholipid bilayer.**  
 The membrane is separated from the substrate by a 10–20 Å thick layer of water [18]. Figure taken from [18]

### Bilayer Production

There are several methods for producing SLBs (Supported Lipid Bilayers) - one of which includes transferring two monolayers of lipids sequentially onto a hydrophilic substrate via vertical and horizontal deposition processes [19]. Alternately, SLBs may also be prepared by spontaneous fusion of lipid vesicles that have been placed on a solid substrate. The process of forming SLBs from vesicles involves applying small unilamellar lipid vesicles to clean glass substrates in aqueous environments. Once the vesicles contact the substrate they adsorb to the hydrophilic substrate, and upon doing so they deform, rupture and spread across the surface of the substrate to form a flat membrane [11], [15]. The process of vesicle rupture is visualized in Figure 2.5.

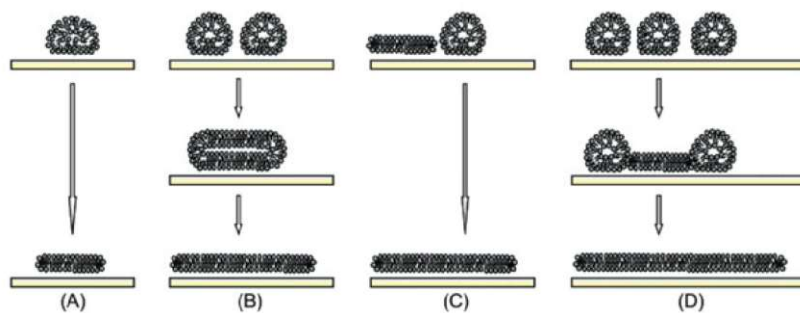


Figure 2.5.: **Mechanisms of vesicle rupture:** (A) an isolated adsorbed vesicle ruptures spontaneously, driven by its support-induced deformation; (B) neighboring adsorbed vesicles fuse and eventually rupture; (C) the active edge of a supported bilayer patch induces the rupture of a neighboring vesicle; (D) the cooperative action of several neighboring vesicles leads to the rupture of a first vesicle (at the critical vesicular coverage). The active edge thereby exposed triggers the rupture of adjacent vesicles [11]. Figure taken from [11]

### Bilayer Composition

Phosphatidylcholines (PCs) represent the dominant lipid class in eukaryotic cell membranes [21]. In investigations of T cell activation, 1-palmitoyl-2-oleoyl-sn-glycero-3-phosphocholine (POPC) is frequently chosen as the principal lipid for generating SLBs [6], [22]. The chemical structure of POPC can be seen in Figure 2.6 a). POPC is a chemically well-defined member of the PC family and remains in a liquid phase at ambient temperature [23], [24], a feature that is essential for allowing membrane-associated proteins to diffuse laterally within the SLB. Such mobility is required for diffusion-driven encounters between membrane components, including receptors and intracellular signaling molecules [25]. In addition to phospholipids, cholesterol is a central modulator of membrane properties and is present at high levels in eukaryotic membranes, where it supports membrane stability [26]. The chemical structure of cholesterol can be seen in Fig. 2.8. Another widely used lipid class comprises nickel-chelating lipids, such as Ni-NTA-DGS, which enable the attachment of recombinant proteins to the membrane surface [27]. The chemical structure of Ni-NTA-DGS can be seen in Figure 2.6 b). The corresponding ligand-coupling strategy is outlined in the section below.

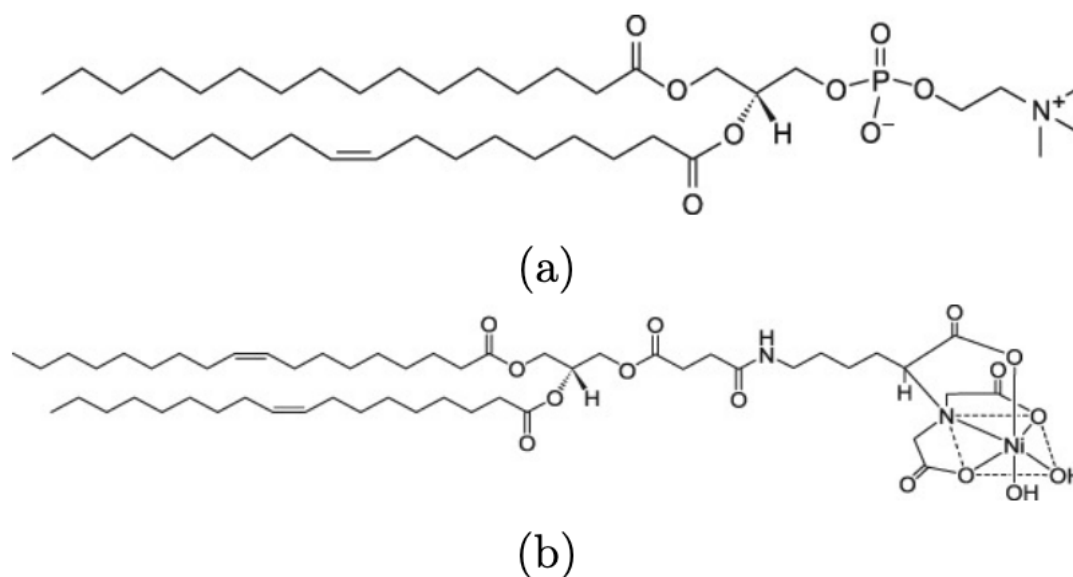


Figure 2.6.: **Chemical structures of lipids commonly used for supported lipid bilayers:** a) POPC [23], b) Ni-NTA-DGS [28].

### Ligand coupling to supported lipid bilayers

For the application of SLBs in immune assays, it is necessary to attach membrane-anchored ligands like proteins to them, preferably with a defined orientation, and with lateral fluidity preserved.

A practical challenge hereby is that the inclusion of transmembrane proteins in SLBs directly may result in reduced mobility, or loss of function through interactions with the substrate [10]. Therefore, transmembrane ligands like pMHC were used in recombinant, soluble form and linked to the lipid bilayer using an affinity tag so that the protein's transmembrane region would not be embedded in the SLB, thus allowing for a laterally mobile, membrane proximal display of the protein [9].

Histidine tagged proteins have been attached to fluid SLBs using nickel-chelating lipids through reversible  $\text{Ni}^{2+}$ /imidazole interactions [27]. The interactions between  $\text{Ni}^{2+}$  and histidine occur through a Lewis acid-base interaction where the imidazole ring of the histidine residue acts as the electron donor and the  $\text{Ni}^{2+}$  ion acts as the electron pair acceptor [29], [30] as shown in Fig. 2.7. The same type of interaction is responsible for the immobilization of polyhistidine tagged proteins during immobilized metal affinity chromatography (IMAC) [29], [30]. Pioneering work by Hochuli et al. showed that the affinity of histidine tagged proteins for  $\text{Ni}^{2+}$  chelating agents increases significantly as the number of histidine residues increases [31], thereby facilitating the widespread use of polyhistidine tags. The most commonly used His-tags contain six consecutive histidine residues and can be placed at either

the N- or C-terminal end of recombinant proteins [32]. Due to the rarity of long oligohistidine regions in native proteins, His-tags are highly specific for binding to  $\text{Ni}^{2+}$ -chelating lipids [33].

In SLB-based assays, the coupling of ligands to histidine tags is most often achieved by including a small amount of  $\text{Ni}^{2+}$ -NTA (or similar chelating group)-containing lipids into the bilayer, allowing for the histidine-tagged protein to associate in an oriented but laterally mobile manner [27], [29]. The  $\text{Ni}^{2+}$ -NTA lipid (i.e., Ni-NTA-DGS) can be added to membrane preparations as part of the mixed bilayer or vesicles preparation process; the ratio of  $\text{Ni}^{2+}$ -NTA lipids to the majority phospholipid (e.g., POPC) is typically controlled [34].

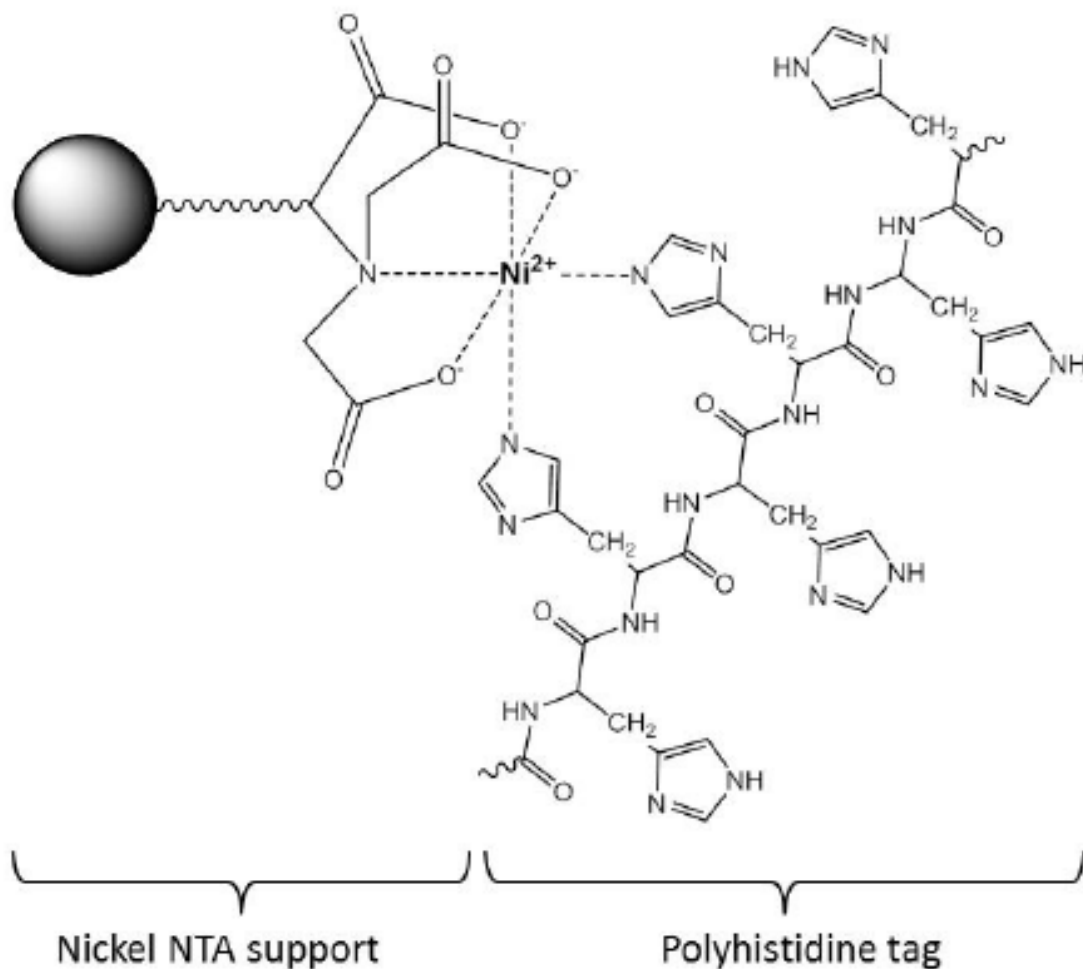


Figure 2.7.: **Complex formation of a poly-His tag with Ni-NTA.** Adapted from [35]

To attach DNA origami to SLBs, triethyleneglycol-cholesteryl have been used [5], [36], [37].

Due to its bulk hydrophobic backbone, cholesterol is capable of spontaneous in-

corporation into lipid bilayer matrices. This property is well utilized for anchoring functional molecules to membranes. It was demonstrated by Lopez that DNA oligonucleotides may be chemically modified using cholesterol at the terminal hydroxyl group resulting in cholesterol-DNA conjugates that will spontaneously incorporate into fluid phosphatidylcholine bilayer membranes [26]. One version that is most often employed utilizes a cholesteryl-tri(ethylene glycol) (cholesteryl-TEG) modification which is commercially available as modified nucleotides and has been employed in model membrane systems (such as SLBs) [37], [38]. The chemical structure of this modification is shown in Fig. 2.8. Additionally, it should be noted that the structural and dynamic characteristics of POPC bilayers are not significantly altered by the use of cholesteryl-TEG anchors and unlike unmodified cholesterol, do not cause lipid condensation when used in the conditions studied by Czogalla et al. [37]. DNA strands tagged with cholesterol allow for the stable orientation of DNA at membrane surface without relying on electrostatic attraction and also provide lateral mobility in fluid membranes allowing for diffusion mediated hybridization and programmable membrane modification [26].

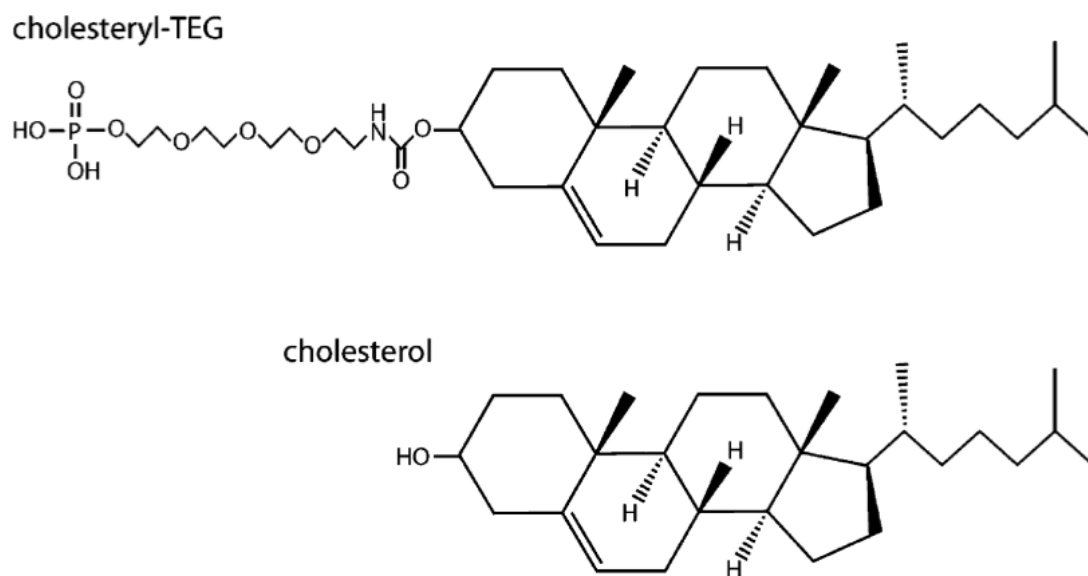


Figure 2.8.: **Chemical structures of cholesteryl-TEG and cholesterol.** Figure adapted from [38]

## 2.2.2. DNA origami platforms for nanoscale ligand presentation

### DNA nanotechnology

Deoxyribonucleic acid (DNA) is an attractive nanoscale building material because Watson-Crick base pairing enables predictable, sequence-programmed self-assembly

[39]. In DNA nanotechnology, this programmability is exploited to construct defined nanostructures by mixing designed strands. A prominent approach is DNA origami, introduced by Rothemund, in which a long single-stranded scaffold is folded into a prescribed shape by many short staple strands [40]. This self-assembly is illustrated in Fig. 2.9. Subsequent work extended DNA origami from two-dimensional to three-dimensional architectures [41], [42]. Importantly, addressable sites on DNA origami enable site-specific attachment of functional components, allowing proteins to be positioned with nanometer precision [43].

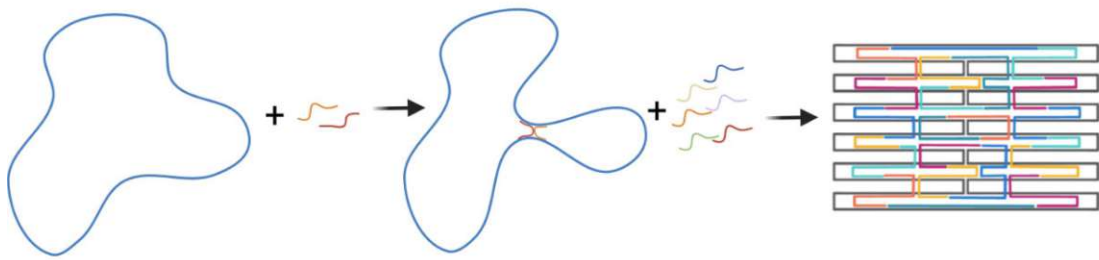


Figure 2.9.: **Self assembly of DNA origami.** A long singular scaffold strand is forced into a predefined shape by small staple strands. Figure adapted from [36].

### DNA origami in immune assays

Despite the low affinity of many physiological TCR-pMHC interactions, T cells can detect very small numbers of agonist pMHC molecules on APCs, motivating the question whether nanoscale receptor-ligand organization contributes to early signaling [6].

To address spatial effects in a defined and systematic manner, Hellmeier et al. developed an APC-mimicking biointerface in which rectangular DNA origami platforms are anchored to fluid-phase planar SLBs and functionalized with pMHC [5], [6]. An exemplary platform-geometry can be seen as a 3D rendering in Figure 2.10. The DNA origami served a dual purpose: it generated steric exclusion zones around individual ligands to isolate them as they cluster during T cell activation, and it permitted the directed preorganization of ligands with nanometer precision [5]. Monovalent platforms contained a single ligand modification site placed approximately at the center of the tile, whereas divalent platforms provided two ligand attachment sites with defined spacings of 10, 20, or 30 nm [5]. These geometries can be seen in Fig. 2.11.

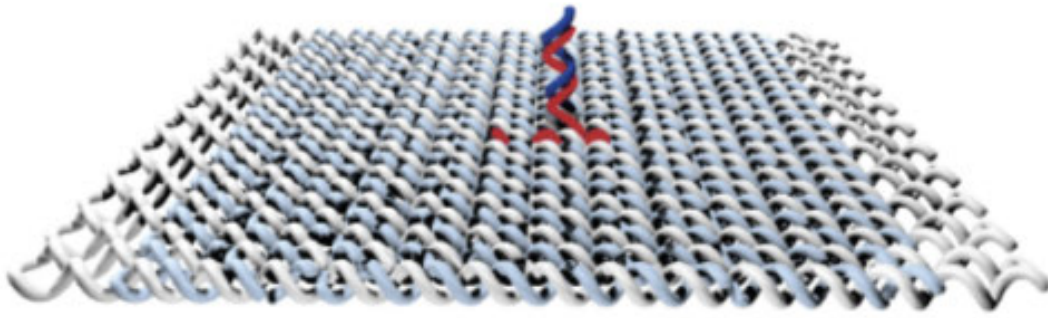


Figure 2.10.: **DNA origami platform 3D rendering.** Platform with a modification site allowing the addition of functional modifications like fluorophores, ligands, etc. Image taken from [5].

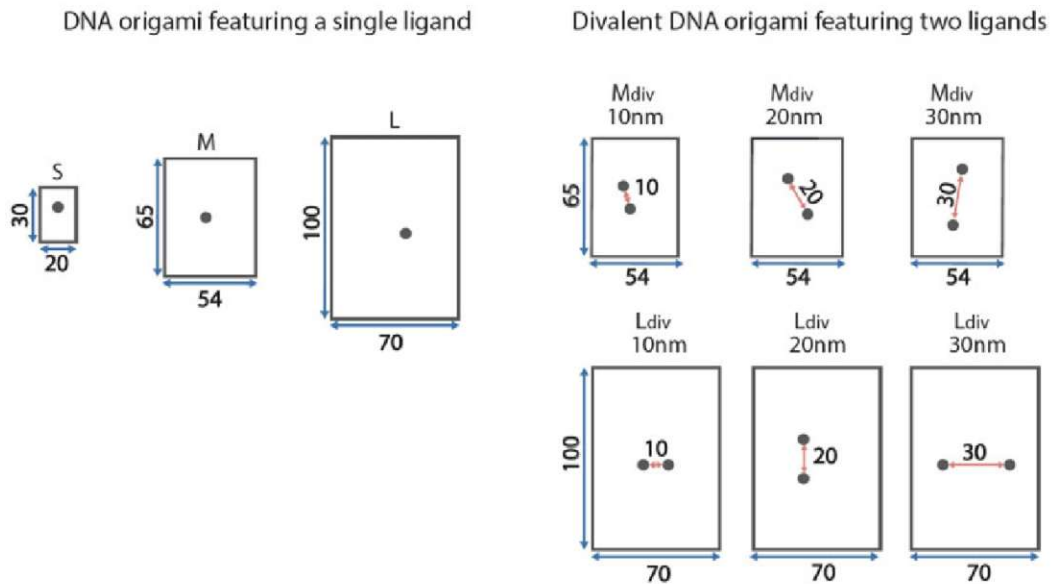


Figure 2.11.: **DNA origami layouts for nanoscale ligand presentation.** Schematic overview of the DNA origami platform designs and nomenclature used by Hellmeier et al. Platforms of different sizes (S, M, L) provide either one central ligand attachment site (monovalent) or two attachment sites (divalent) with defined spacings of 10, 20, or 30 nm. Distances are given in nm. Adapted from [5].

## 2.3. Total Internal Reflection Fluorescence Microscopy

### 2.3.1. Principle and surface selectivity

Total internal reflection fluorescence (TIRF) microscopy is an optical imaging technique that enables the selective excitation of fluorescent probes positioned in close proximity to a solid–liquid interface. Under TIRF illumination, fluorophores are excited exclusively within a very thin layer next to a solid surface, typically extending less than 100 nm. This spatial restriction of excitation arises from an evanescent electromagnetic field that develops when incident light undergoes total internal reflection at the interface. Consequently, fluorescence originating from regions farther away from the surface is largely suppressed. TIRF images therefore display substantially reduced background intensity, an absence of detectable out-of-focus fluorescence, and minimal photonic exposure of sample regions outside the illuminated plane [17].

The physical origin of total internal reflection lies in the refraction behavior of light at the boundary between two media with different refractive indices. When a light beam propagating in a medium with higher refractive index  $n_2$  (e.g. glass) impinges on an interface with a medium of lower refractive index  $n_1$  (e.g. water), total internal reflection occurs if the angle of incidence  $\theta$ , measured with respect to the surface normal, exceeds a material-specific critical angle  $\theta_c$ . This critical angle is given by

$$\theta_c = \sin^{-1}\left(\frac{n_1}{n_2}\right), \quad (2.1)$$

where the ratio  $n_1/n_2$  must be smaller than unity for total internal reflection to occur [17]. For incidence angles  $\theta < \theta_c$ , the excitation light is partially transmitted into the lower-index medium according to Snell’s law, whereas for  $\theta > \theta_c$ , the incident beam is completely reflected back into the higher-index medium.

A schematic illustration of the optical geometry underlying total internal reflection and the formation of the evanescent field is shown in Figure 2.12.

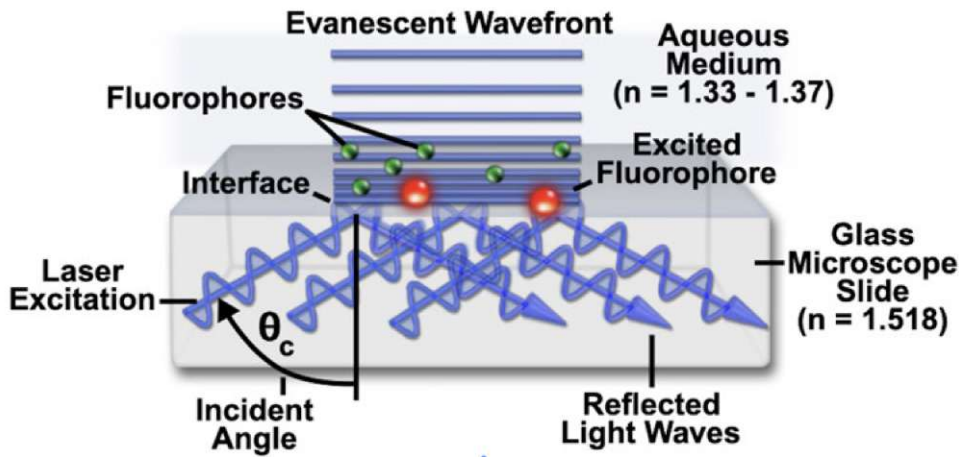


Figure 2.12.: Schematic representation of total internal reflection fluorescence (TIRF) microscopy. An excitation laser beam propagates within the glass substrate ( $n_2$ ) and impinges on the glass-aqueous interface at an incidence angle  $\theta$  exceeding the critical angle  $\theta_c$ . Under this condition, the light is totally internally reflected, giving rise to an evanescent electromagnetic field that penetrates only a short distance into the aqueous medium ( $n_1$ ). This evanescent field decays exponentially with distance from the interface and selectively excites fluorophores located within a few tens of nanometers above the surface, while fluorophores farther away remain unexcited [17]. Image taken from [44]

Although no propagating light enters the lower-index medium under total internal reflection, the electromagnetic field does not vanish abruptly at the interface. Instead, a non-propagating evanescent field is formed, which penetrates into the adjacent medium and decays exponentially with increasing distance from the surface. For a plane wave incident on an ideal planar interface, the intensity of this evanescent field as a function of the distance  $z$  normal to the interface is described by

$$I(z) = I(0) e^{-z/d}, \quad (2.2)$$

where  $I(0)$  denotes the intensity at the interface and  $d$  is the characteristic penetration depth of the evanescent field. The penetration depth is given by

$$d = \frac{\lambda_0}{4\pi\sqrt{n_2^2 \sin^2 \theta - n_1^2}}, \quad (2.3)$$

with  $\lambda_0$  being the wavelength of the incident light in vacuum [17].

As the incidence angle  $\theta$  is increased, the evanescent field penetration depth  $d$  correspondingly diminishes and typically remains comparable to, or smaller than,

the excitation wavelength, except in the immediate vicinity of the critical angle where  $d$  increases substantially. Consequently, fluorescence excitation is effectively confined to molecules located within several tens of nanometers from the interface, while fluorophores situated at larger distances experience negligible excitation. This spatial confinement of the excitation field constitutes the fundamental origin of the pronounced surface sensitivity of TIRF microscopy, enabling high-contrast imaging of structures associated with interfaces under conditions of minimal background signal. Given that SLBs have a thickness of only a few nanometers, they are entirely encompassed by the evanescent field, allowing fluorophores embedded within or attached to the bilayer to be selectively and efficiently excited [11].

### 2.3.2. Single Particle Tracking

Single Particle Tracking is a method to track trajectories of individual fluorophores in cell membranes or model systems of such [45]. Compared to other techniques like fluorescence recovery after photobleaching (FRAP) it does not rely on average motion of large ensembles of molecules, but determines motion of individual particles with nanometer-scale precision [45].

SPT relies on determining the positions of fluorophores in the x-/y-plane for each acquired image frame. The localizations obtained in individual frames are then connected to those in adjacent frames using a nearest-neighbor algorithm, which yields a for each fluorophore. Based on these trajectories, the mean square displacement (MSD) is calculated for a specified time lag  $t$ . The MSD can subsequently be used to estimate the diffusion coefficient  $D$  [45].

## 2.4. Biophysical readouts of SLB-based biointerfaces

In order to assess the physical performance and stability of SLB-based biointerfaces, this section introduces the two key experimental readouts used throughout this thesis: lateral diffusion of membrane-tethered objects and fluorescence intensity as a proxy for surface density.

### 2.4.1. Lateral diffusion of membrane-tethered objects

Like lipids, membrane proteins can diffuse laterally within the plane of the lipid bilayer—an essential dynamic feature for cellular signaling [3]. Measurements of membrane protein mobility provide important insights into membrane structure and the interactions between its components [25]. In two-dimensional membranes,

diffusion markedly increases the encounter frequency between ligands and receptors compared with freely diffusing ligands in solution, thereby promoting efficient initiation of signaling [25].

In the context of T cell activation, the lateral mobility of membrane-anchored pMHC and TCR is associated with higher apparent affinities and more rapid binding kinetics than those observed for their soluble forms, in better agreement with functional immune outcomes [46]. Additionally, diffusion supports the dynamic assembly of microclusters and their spatial reorganization into the immunological synapse, enabling sustained signal transduction [47].

Within this work, lateral diffusion serves as a key indicator for the functional integrity of the model membrane. A sufficiently high mobility over time indicates the absence of ligand immobilization or lateral aggregation (e.g., clustering or trapping in membrane domains or defects), both of which could impair T cell activation.

To assess lateral mobility in this study, single particle tracking (SPT) is employed (see section 2.3.2). From the acquired trajectories, diffusion coefficients can be derived and potential immobilization or clustering events identified.

#### **2.4.2. Fluorescence intensity as a proxy for surface density and binding persistence**

In SLB-based systems, fluorescence intensity provides an indirect but effective read-out for assessing the density and binding persistence of membrane-tethered ligands. This approach can be used in experimental setups where surface-bound molecules are fluorescently labeled and can therefore be quantitatively monitored over time.

Fluorescence measurements allow estimation of ligand surface coverage, either through calibration against supported bilayer standards or via relative comparisons under consistent imaging conditions. SLBs offer a uniform, laterally fluid platform well suited for quantitative fluorescence analysis, enabling the mapping of measured intensity to molecular surface density across a wide range of fluorophore concentrations [48].

In the context of this work, fluorescence intensity is used to monitor ligand loss or redistribution, which may indicate instability of the SLB or detachment of membrane-tethered proteins. For example, imaging of fluorescently labeled proteins can reveal “black holes” in the fluorescence signal that indicate membrane defects [7]. Moreover, SLBs are commonly functionalized with fluorescently labeled ligands, and ligand redistribution can be quantified via an accumulation or depletion of signal within a defined area [49]. Importantly, when ligands are attached via polyhistidine tags to Ni<sup>2+</sup>-chelating lipids, the interaction can be weak enough that bound pro-

teins detach during an experiment [49], leading to a decrease in fluorescence intensity over time.

Thus, fluorescence intensity serves as a complementary readout to diffusion measurements, providing information about the functional persistence of membrane-decorated ligands in SLB-based immune assay platforms.

### 2.4.3. Determinants and temperature dependence

In this thesis, temperature effects are evaluated with respect to the key readouts: lateral diffusion and fluorescence intensity. While previous T cell activation assays using the presented SLB-based system were performed at room temperature, future experiments should be conducted at 37 °C to more closely mimic physiological conditions.

According to the Saffman–Delbrück model, the lateral diffusion coefficient  $D$  of membrane-tethered molecules increases linearly with temperature:

$$D \propto \frac{T}{\eta_m} \quad (2.4)$$

where  $T$  is the absolute temperature and  $\eta_m$  the membrane viscosity [50]. Thus, higher temperatures are expected to accelerate diffusion, potentially enhancing receptor–ligand encounter rates and facilitating immunological synapse formation.

However, elevated temperatures may also compromise system stability. In particular, the non-covalent interaction between polyhistidine tags and Ni-DGS-NTA lipids becomes less stable at higher temperatures, increasing the likelihood of ligand desorption from the membrane. This effect was observed for the murine pMHC molecule I-E<sup>K</sup> bearing two His-tags using HBSS as an imaging buffer, which showed substantially higher dissociation rates from SLBs at 37 °C compared to room temperature [9]. Although these higher dissociation rates are suspected to be caused by HBSS buffer. That is why the temperature-dependent detachment should be investigated for human HLA-A\*02:01 pMHC complexes as well as for the DNA origami platforms without changing to HBSS buffer for imaging.

Consequently, both diffusion and fluorescence intensity measurements are required to assess whether the system retains sufficient molecular mobility and ligand density at 37 °C for effective T cell stimulation.

## 3. Material and Methods

### 3.1. DNA Origami

For the subsequent experiments, DNA origami platforms were prepared based on a previously established design by Hellmeier [5]. Two distinct platform geometries were employed in this work, both with lateral dimensions of  $70 \times 100$  nm and hereafter referred to as L-platforms. The DNA origami structures were designed using the M13mp18 scaffold strand [40] and assembled from a corresponding set of staple strands.

At predefined sites intended for ligand attachment on the top side of the platforms, selected staple strands were extended at their 3'-ends with single-stranded overhangs serving as binding sites. These overhangs included a short poly-thymidine linker proximal to the origami surface to provide spatial flexibility. Two platform variants were used: the L1V-platform, containing a single V' binding site (which is a oligonucleotide with the sequence GTGGAGTAGTGTCATGT), and the L2V-platform, containing two V' binding sites. Fluorophores used in this study, specifically Alexa Fluor 647, were functionalized with complementary V-tag oligonucleotides (with the sequence ACATGACACTACTCCAC), enabling sequence-specific hybridization to the V' sites on the platforms.

For membrane attachment, staple strands located at the bottom face of the origami structures were elongated with single-stranded extensions called Z' designed to hybridize with complementary cholesteryl-TEG-modified oligonucleotides incorporated into the SLB. These Z' strands have a sequence of 5' AGA GTC CTA GCA TAT TTA GCC 3' and attach to the complimentary strands of the cholesteryl-TEG-modified oligonucleotides, which have a sequence 5' -cholesterol-TEG- GGC TAA ATA TGC TAG GAC TCT 3'. There are eight such Z' single-strand extensions per platform, to enable stable binding to the cholesteryl-TEG. Following folding and purification, the DNA origami platforms were subsequently used to seed the SLBs.

### 3.1.1. DNA Origami Folding

DNA origami platforms were assembled in a single, one-pot folding reaction performed in a polymerase chain reaction (PCR) tube (Bio-Rad Laboratories). Each tube contained a DNA origami mixture composed of the ssDNA scaffold p7249 (tilibit nanosystems GmbH) and a pool of single-stranded staple oligonucleotides (Microsynth AG), supplemented with 10  $\mu\text{L}$  folding buffer (FoB) (50 mM Tris (ThermoFisher Scientific<sup>TM</sup>), 500 mM NaCl (ThermoFisher Scientific<sup>TM</sup>), 10 mM EDTA (ThermoFisher Scientific<sup>TM</sup>), 12.5 mM  $\text{MgCl}_2$ , and fluorophore-labeled strands (Integrated DNA Technologies). Detailed compositions of the origami mixtures are listed in Tables A.8 and A.7.

### 3.1.2. DNA Origami Purification

The samples were purified to remove excess staple strands. For purification, Ultrafiltration was used.

100 kDa Amicon<sup>®</sup> Ultra 0.5 mL centrifugal filters (Merck) were pre-rinsed by loading each unit with 500  $\mu\text{L}$  purification buffer (PuB) (5 mM Tris, 50 mM NaCl, 1 mM EDTA, 10 mM  $\text{MgCl}_2$ ) and centrifuging at  $5000 \times g$  for 5 min at room temperature. The flow-through was discarded, the filters were loaded with the sample, and, if required, topped up to 500  $\mu\text{L}$  with PuB. For purification, the 100 kDa Amicon<sup>®</sup> Ultra filters were centrifuged at  $7000 \times g$  for 5 min at room temperature. After removing the flow-through, the filters were again filled with PuB and centrifuged. In total, the sample underwent three purification cycles using this procedure. For recovery, the filters were inverted into a new tube containing 20  $\mu\text{L}$  PuB and centrifuged at  $5000 \times g$  for 4 min at room temperature. Platform concentrations were determined using a microplate reader. The sample was subsequently transferred to a 1.5 mL Eppendorf Biopur<sup>®</sup> tube and stored at  $-20^\circ\text{C}$ .

## 3.2. pMHC complex

The peptide-MHC (pMHC) complex used in this work was based on the human MHC class I allele HLA-A\*02:01 and loaded with the CMV pp65-derived peptide NLVPMVATV. The recombinant construct carried a C-terminal  $12 \times \text{His}$  tag. pMHC complex was fluorescently labeled with Alexa Fluor 647 using NHS-ester labeling chemistry. The protein was expressed in *E. coli* and purified by Vanessa Mühlgrabner (Medical University of Vienna).

## 3.3. Supported Lipid Bilayer Formation

### 3.3.1. Vesicle Formation

Lipid vesicles were generated from a defined mixture of phospholipids consisting of POPC and DGS-NTA(Ni) (Avanti® Polar Lipids, Inc.). The lipids were combined at a molar ratio of 98 % POPC to 2 % DGS-NTA(Ni). For the preparation of a 1× vesicle stock solution, lipids were transferred to a final concentration of 125  $\mu\text{M}$  into a glass vial and dried under a continuous nitrogen stream for 20 min to ensure complete removal of chloroform residues. The resulting lipid film was rehydrated with 1 mL of 10× Dulbecco’s phosphate-buffered saline (DPBS) (Sigma-Aldrich) and thoroughly mixed using a vortex mixer (IKA Labortechnik). After sealing the vial with Parafilm® (Amcor Limited), vesicle formation was induced by bath sonication (Emmi®D40, EMAG Technologies®) for 10 min at room temperature. To obtain a homogeneous vesicle population, the vesicle suspension was subsequently filtered through a 0.22  $\mu\text{m}$  filter (Whatman Puradisc™ 13mm from cytiva).

### 3.3.2. Bilayer Formation

SLBs were assembled in a Nunc™ Lab-Tek 8-well chamber (LTC) (Thermo Scientific™) using a glass coverslip as substrate. Prior to assembly, the coverslip was treated in a plasma cleaner (Harrick Plasma) for 2 min at room temperature to render the surface hydrophilic. The original glass bottom of the chamber was removed, and the plasma-cleaned coverslip was subsequently attached to the chamber using an addition-curing silicone adhesive (eco-sil extrahart, Picodent). After curing of the adhesive for about 10 min at room temperature, ensuring the adhesive dried completely, 200  $\mu\text{L}$  of the 1× vesicle suspension were added to each well.

Following the addition of 200  $\mu\text{L}$  of vesicle suspension to each well, the samples were incubated for 20 min at room temperature to allow bilayer formation. Subsequently, each well was thoroughly washed with DPBS to remove excess vesicles.

## 3.4. SLB Functionalization

### 3.4.1. Functionalization of SLBs with pMHC Molecules

For functionalization with pMHC molecules, each well was washed with 15 mL of DPBS. Thereafter, 430  $\mu\text{L}$  of buffer were removed from each well to adjust the volume to remaining 350  $\mu\text{L}$ . Subsequently, 100  $\mu\text{L}$  of pMHC solution at the desired concentrations of 20  $\text{ng}/\text{well}$  for bulk fluorescence measurements or 10  $\text{ng}/\text{well}$  for

single molecule localization and subsequent tracking or single molecule brightness analysis were added. The samples were incubated for 60 min at room temperature to allow binding of the His-tagged pMHC molecules to the Ni-NTA-functionalized SLBs. Finally, each well was washed again with 15 mL of 1×DPBS to remove unbound pMHC. Subsequently removing 430  $\mu\text{L}$  of supernatant to leave 350  $\mu\text{L}$  in each well.

### 3.4.2. Functionalization of SLBs with DNA origami Platforms

Each well was then washed with 15 mL of 1× DPBS supplemented with 0.1 % bovine serum albumin (BSA) to passivate the SLB. Subsequently, the liquid meniscus as well as 430  $\mu\text{L}$  of buffer were carefully removed. To incubate the BSA, it was left for 30 min at room temperature.

To enable membrane anchoring of the DNA origami platforms, 100  $\mu\text{M}$  cholesteryl-TEG-Z (biomers.net), complementary to the oligonucleotide sequences located at the bottom of the origami structures, diluted in 99.5  $\mu\text{L}$  of 1× DPBS, were added to each well and incubated for 15 min at room temperature before washing each well thoroughly with 15 mL of 1× DPBS containing 10 mM  $\text{MgCl}_2$ .

DNA origami platforms at the desired concentrations, diluted in 1× DPBS, were subsequently added to each well. The Lab-Tek chamber was covered with aluminium foil to protect the samples from light and incubated for 60 min at room temperature. Finally, each well was washed again with 15 mL of 1× DPBS supplemented with 10 mM  $\text{MgCl}_2$  to remove unbound origami structures. Subsequently removing 430  $\mu\text{L}$  of supernatant to leave 350  $\mu\text{L}$  in each well.

## 3.5. Single-Molecule TIRF Imaging

Single-molecule total internal reflection fluorescence (TIRF) microscopy was used to image membrane-associated DNA origami platforms and pMHC molecules under controlled temperature conditions. This approach enabled the selective excitation of fluorophores located in close proximity to the SLB, thereby allowing both single-molecule tracking and bulk fluorescence measurements.

For each measurement time point, image series were acquired at ten spatially distinct positions within each well to account for potential lateral heterogeneity of the SLB. This sampling strategy ensured robust averaging within individual wells. Images were acquired with an exposure time of 3 *ms*. Accounting for an additional camera readout delay of 7 *ms* between frames, this resulted in an effective frame rate of 100 *Hz*.

Measurements were performed on a custom-built optical setup based on an Axio Observer 7 microscope (Zeiss), equipped with an  $\alpha$  Plan-Apochromat oil-immersion objective (100 $\times$ , numerical aperture 1.46, DIC, UV/VIS/IR compatible). Excitation was provided by a 642 nm laser source (Coherent® Obis™ Galaxy Laser 1236445). Separation of excitation and emission light was achieved using a multiband dichroic mirror (Di01-R405/488/532/635-25x36, Semrock).

Fluorescence signals were detected using an electron-multiplying CCD camera (EMCCD, Andor iXon Ultra) with an effective pixel size of 160 nm in the object plane, operated at a sensor temperature of  $-60^\circ\text{C}$ . Instrument control, including laser selection, laser power settings, and imaging parameters, was performed using the LabVIEW-based software SDT-Control. Laser power was attenuated to 20% for measurements of L2V platforms and pMHC. For measurements of L1V platforms at  $37^\circ\text{C}$  the laserpower was attenuated to 40% (on 02.12.2025) and for  $26^\circ\text{C}$  it was at 100% (on 04.12.2025). Laserpower was only measured for L1V experiments on the 02.12. ( $37^\circ\text{C}$ ) and 04.12. ( $26^\circ\text{C}$ ), before and after imaging each. The laserpower on the 02.12. ranged from  $0.485 - 0.468 \text{ kW/cm}^2$  (values at 100%, see Figure A.3) with an attenuation of 40% this resulted in an effective laserpower ranging from  $0.194 - 0.187 \text{ kW/cm}^2$ . The laserpower on the 04.12. ranged from  $0.577 - 0.636 \text{ kW/cm}^2$  (see Figure A.4). The incidence angle required for TIRF illumination was adjusted using the LabVIEW program Servotisch and optimized individually for each measurement series.

Temperature control during imaging was achieved using a stage-top incubator system (ToKai HIT), allowing stable measurements at defined temperatures over extended acquisition periods.

Prior to imaging, both the objective lens and the glass bottom of the Lab-Tek chamber were cleaned with ethanol. A droplet of immersion oil (Carl Zeiss™ Immersol™ 518) was applied to the objective before mounting the sample.

### 3.6. Experimental design and statistical units

All quantitative analyses of the acquired image data were performed on a per-well basis. Each well of the Lab-Tek chamber was treated as an independent experimental unit, within which repeated measurements were acquired at multiple time points. Temporal trends were quantified separately for each well using linear regression models.

Two temperature conditions were investigated,  $26^\circ\text{C}$  and  $37^\circ\text{C}$ . Measurements were performed using defined amounts of molecules added per well, specified as

the total mass added per well (ng), rather than controlled surface densities. As a consequence, absolute surface coverage could vary between wells, and quantitative comparisons focused on relative temporal changes within individual wells.

For single-molecule tracking and the corresponding diffusion analysis, L1V and L2V DNA origami platforms were applied at a concentration of 20 ng per well. For pMHC molecules, diffusion measurements were carried out at concentrations of 20 ng and 10 ng per well. Wells prepared at these lower seeding concentrations will hereafter be referred to as single-molecule wells. Diffusion analyses were performed separately for each molecular system and concentration.

In addition, single-molecule brightness was analyzed over time as a quality-control readout to assess potential unresolved multi-emitter events (e.g., fluorophore aggregation) that could bias localization-based quantification. Mean single-molecule brightness was therefore evaluated per well and time point and summarized as well-wise temporal slopes. Brightness-coded scatter plots of individual diffusion coefficients (e.g.,  $D$  versus track length) were generated for each well and time point and are provided in the Appendix as diagnostic visualizations.

For measurements of fluorescence intensity, we employed higher seeding concentrations to achieve adequate signal strength. Specifically, L1V and L2V DNA origami platforms were seeded at 400 ng per well, and pMHC molecules at 20 ng per well. In the context of this thesis, wells prepared with these elevated concentrations are termed bulk wells. Bulk intensity and diffusion measurements were considered as separate experimental readouts and were analyzed independently.

For bulk fluorescence wells, an initial surface density estimate  $\rho(t_0)$  was derived from bulk intensity and single-molecule brightness (Eq. 3.4).

For L2V DNA origami platforms and pMHC molecules, measurements were conducted on two independent experimental days per temperature condition. On each day, two wells were analyzed per concentration, resulting in four wells per temperature and measurement type. For L1V DNA origami platforms, measurements were performed on a single experimental day per temperature condition, with two wells analyzed per concentration and temperature. All wells and seeding densities are summarized in Tabs. 3.1 and 3.2.

Temperature-dependent effects were assessed by comparing the distributions of well-wise regression slopes between conditions. This approach ensured that temporal changes within individual wells were quantified independently of absolute signal levels and enabled robust comparison between temperature conditions.

Date	$T$	Construct	Seeding (ng/well)	Readout	Wells	Notes
02.10.	26 °C	L2V	20	SPT / diffusion	SLB1, SLB2	single-molecule wells
02.10.	26 °C	L2V	400	bulk intensity	SLB1, SLB2	bulk wells
02.10.	26 °C	pMHC	20	SPT / diffusion / bulk intensity	SLB1, SLB2	single-molecule wells / bulk wells
09.10.	26 °C	L2V	20	SPT / diffusion	SLB1, SLB2	single-molecule wells
09.10.	26 °C	L2V	400	bulk intensity	SLB1, SLB2	bulk wells
09.10.	26 °C	pMHC	10	SPT / diffusion	SLB1, SLB2	single-molecule wells
09.10.	26 °C	pMHC	20	bulk intensity	SLB1, SLB2	bulk wells
03.10.	37 °C	L2V	20	SPT / diffusion	SLB1, SLB2	single-molecule wells
03.10.	37 °C	L2V	400	bulk intensity	SLB1, SLB2	bulk wells
03.10.	37 °C	pMHC	10	SPT / diffusion	SLB1, SLB2	single-molecule wells
03.10.	37 °C	pMHC	20	bulk intensity	SLB1, SLB2	bulk wells
10.10.	37 °C	L2V	20	SPT / diffusion	SLB1, SLB2	single-molecule wells
10.10.	37 °C	L2V	400	bulk intensity	SLB1, SLB2	bulk wells
10.10.	37 °C	pMHC	10	SPT / diffusion	SLB1, SLB2	single-molecule wells
10.10.	37 °C	pMHC	20	bulk intensity	SLB1, SLB2	bulk wells

Table 3.1.: **Overview of measurement days and well allocation for L2V and pMHC.** Each condition comprised two wells (SLB1 and SLB2). “SPT/diffusion” denotes single-molecule wells; “bulk intensity” denotes bulk wells.

Date	$T$	Construct	Seeding (ng/well)	Readout	Wells	Notes
04.12.	26 °C	L1V	20	SPT / diffusion	SLB1, SLB2	single-molecule wells
04.12.	26 °C	L1V	400	bulk intensity	SLB1, SLB2	bulk wells
02.12.	37 °C	L1V	20	SPT / diffusion	SLB1, SLB2	single-molecule wells
02.12.	37 °C	L1V	400	bulk intensity	SLB1, SLB2	bulk wells

Table 3.2.: **Overview of measurement days and well allocation for L1V.** Each condition comprised two wells (SLB1 and SLB2). “SPT/diffusion” denotes single-molecule wells; “bulk intensity” denotes bulk wells.

### 3.6.1. Single molecule localization and quantification of single-molecule brightness

Single-molecule brightness values were determined for each model system. These values were used (i) to estimate the seeded surface density at  $t_0$  from bulk intensity measurements and (ii) as a quality-control readout to probe potential unresolved multi-emitter events (e.g., fluorophore aggregation) over time.

Individual molecule localizations were obtained using the `sdt-python` package developed by Schrangl [51], which implements the 3D-DAOSTORM algorithm [52]. For each localization, the extracted parameters included the spatial coordinates ( $x, y$ ), frame index, spot size (Gaussian standard deviation), peak amplitude, local background, and the background-corrected integrated intensity.

To obtain a robust estimate of single-fluorophore brightness  $I_{SM}$  for density calculations, brightness was quantified from the last frames of L2V and pMHC image acquisitions (frames 90-99), where photo bleaching increases the fraction of single-emitter events. Originally only L2V platforms were used for the experiments, but single molecule brightness turned out to be hard to determine for L2V platforms, as each platform carries two fluorophores, while incomplete labeling results in a mixture of platforms with zero, one, or two fluorophores. This leads to different single molecule brightnesses for each individual localization, as it is not guaranteed, that only one fluorophore is localized. By using only last frames for analysis, the amount of doubly labeled platforms should be minimized to estimate single fluorophore-brightness. This problem motivated the use of single labeled platforms L1V, as they either present one or no fluorophore (which would not be localized), which leads to reliable single fluorophore brightness. For L1V frames 0-99 were used, as there was a low abundance of fluorophores in general visible, and last frames did occasionally not show any fluorophores.

For time-resolved assessment of aggregation-related brightness changes, mean single-molecule brightness was computed per well and time point of the corresponding acquisitions using an identical analysis pipeline across all time points. Brightness-coded diagnostic plots of individual diffusion coefficients (e.g.,  $D$  versus track length) were generated per well and time point and are provided in the Appendix.

### 3.6.2. Quantification of Fluorophore Diffusion Changes

Because lateral mobility is a functional requirement of APC-mimicking SLBs, diffusion was quantified as a readout of whether membrane-tethered ligands remain dynamically accessible over time; in this context, a systematic decrease in  $D(t)$  would be consistent with increasing immobilization (e.g., trapping/aggregation), whereas stable  $D(t)$  indicates preserved mobility over the measurement window.

The acquired single-molecule localizations were linked into trajectories, from which diffusion coefficients were extracted. Diffusion analysis was performed on the trajectory level, and two complementary readouts were derived: (i) a position-wise mean diffusion coefficient used for well-wise  $D(t)$  traces and regressions, and (ii) trajectory-pooled mobility-class fractions used for diffusion population trend plots.

The diffusion coefficient for individual trajectories was obtained from mean squared displacement (MSD) analysis under the assumption of two-dimensional Brownian motion. For each trajectory, the MSD was calculated as a function of the time lag

$t$  according to

$$\text{MSD}(t) = \langle [x(t + \Delta t) - x(t)]^2 + [y(t + \Delta t) - y(t)]^2 \rangle, \quad (3.1)$$

where the angular brackets denote averaging over all displacement steps within a trajectory. The diffusion coefficient  $D$  was determined from the initial linear regime of the MSD curve using the relation

$$\text{MSD}(t) = 4Dt + 4\sigma_{xy}, \quad (3.2)$$

where  $\sigma_{xy}$  accounts for the localization precision in the lateral plane. To minimize the influence of localization noise and deviations from ideal Brownian behavior at longer time lags,  $D$  was extracted exclusively from the first two MSD points of each trajectory. Only trajectories with a minimum track length of three localizations were included.

Particle linking between consecutive frames was performed using a nearest-neighbor approach with a maximum allowed displacement (search range) defined in units of pixels, following standard feature-linking concepts commonly used in particle tracking workflows [53]. For DNA origami platforms (L1V and L2V), a search range of 2.5 pixels was used, whereas for pMHC molecules a larger search range of four pixels was applied to account for their higher lateral mobility.

Trajectory extraction was not performed on the full set of recorded frames. In the initial frames of each image series, fluorophore surface density was frequently too high to reliably resolve individual molecules, leading to ambiguous localizations and trajectory overlap. As fluorophore photobleaching progressively reduced the number of visible emitters, localization and tracking reliability improved in later frames. To ensure robust single-molecule tracking, only subsets of frames were therefore included in the analysis. For DNA origami platforms, trajectories were extracted starting from frame 10, whereas for pMHC molecules tracking was initiated from frame 50. These frame-selection criteria were applied consistently across all wells and measurement time points.

For the well-wise diffusion time traces, trajectories were first grouped by imaged position within a well at each measurement time point. For each position, a mean diffusion coefficient was computed by averaging trajectory-wise  $D$  values, and the reported diffusion value  $D(t)$  corresponds to the average of these position-wise mean diffusion coefficients within the well.

In addition, diffusion population trends were quantified by pooling all trajectories across all imaged positions within a well at a given time point and classifying each

trajectory into mobility classes based on its diffusion coefficient. For DNA origami platforms, the class boundaries were defined as  $D < 0.05$  (immobile),  $0.05 \leq D < 0.10$ ,  $0.10 \leq D < 0.20$ ,  $0.20 \leq D < 0.30$ ,  $0.30 \leq D < 0.50$ , and  $D \geq 0.50 \mu\text{m}^2 \text{s}^{-1}$  (fast). For pMHC molecules, wider boundaries were used ( $D < 0.05$  (immobile),  $0.05 \leq D < 0.5$ ,  $0.5 \leq D < 1.0$ ,  $1.0 \leq D < 1.5$ ,  $1.5 \leq D < 2.5$ , and  $D \geq 2.5 \mu\text{m}^2 \text{s}^{-1}$  (fast)). For each time point, the fraction of trajectories in each mobility class was computed and its temporal trend was summarized by the slope of a linear regression (in % per minute).

### 3.6.3. Quantification of Temporal Fluorescence Intensity Changes

Because bulk fluorescence intensity scales with the amount of fluorophore present in the imaging plane, temporal intensity changes were used as a practical proxy for changes in ligand surface coverage and SLB integrity: under constant acquisition settings, stable intensity is expected for stable coverage, whereas systematic decreases are consistent with ligand loss and/or defect formation.

Temporal changes in fluorophore abundance were assessed by analyzing the mean fluorescence intensity within a bulk region of interest (ROI) as a function of time. For each image series, a spatially fixed ROI covering the illuminated field of view was defined. Mean pixel intensities were extracted on a frame-by-frame basis and subsequently averaged across all frames and imaged positions within a well to obtain a single mean intensity value per measurement time point.

To account for well-to-well variations in absolute signal levels, fluorescence intensities were normalized to the initial measurement time point according to

$$I_{\text{rel}}(t) = \frac{I(t)}{I(t_0)}, \quad (3.3)$$

where  $I(t)$  denotes the mean ROI intensity at time  $t$  and  $t_0$  the first acquired time point. Each well was treated as an independent experimental unit.

For bulk fluorescence wells, the initial surface density at  $t_0$  was estimated from the bulk intensity and the single-molecule brightness at  $t_0$ . Specifically, the background-corrected mean ROI intensity at  $t_0$  (denoted  $I_{\text{corr}}$  in units of counts per pixel) was divided by the single-molecule brightness  $I_{\text{SMI}}$  (counts per signal) and converted using the pixel area. The resulting surface density  $\rho$  was calculated as

$$\rho \left[ \frac{\text{signals}}{\mu\text{m}^2} \right] = \frac{I_{\text{corr}} \left[ \frac{\text{counts}}{\text{px}} \right]}{I_{\text{SMI}} \left[ \frac{\text{counts}}{\text{signal}} \right] \cdot 0.16^2 \left[ \frac{\mu\text{m}^2}{\text{px}} \right]}. \quad (3.4)$$

For each well, a linear regression of  $I_{\text{rel}}(t)$  as a function of time was performed, and the resulting slope was used as a per-well measure of temporal intensity change. Temperature-dependent effects were assessed by comparing the distributions of well-wise regression slopes between conditions using an unpaired two-sided statistical test.

## 4. Results

This chapter summarizes time-resolved TIRF microscopy measurements of single fluorescently and double fluorescently labeled membrane-associated DNA origami platforms (L1V and L2V) and pMHC molecules under 26 °C and 37 °C. The Results are organized by readout: (i) lateral mobility from single-molecule tracking (diffusion coefficients), (ii) bulk fluorescence intensity as a proxy for molecular abundance and (iii) single-molecule brightness as a quality-control metric to assess potential unresolved multi-emitter events.

### 4.1. Temperature dependence of lateral diffusion

Lateral mobility was quantified using diffusion coefficients obtained from single-molecule tracking. Two complementary diffusion readouts were analyzed: (i) well-wise mean diffusion coefficients  $D(t)$  derived from averages of position-wise mean trajectory diffusion coefficients, and (ii) trajectory-level diffusion population trends that report the fraction of trajectories in predefined mobility classes over time. For each well, temporal trends in  $D(t)$  were summarized by the slope of a linear regression against elapsed measurement time. Temperature effects were assessed by comparing the distributions of well-wise slopes between 26 °C and 37 °C. Diffusion results are reported for L2V, L1V, and pMHC in turn.

#### 4.1.1. L2V

Figure 4.1 shows  $D(t)$  traces and well-wise regressions for L2V platforms.

At 26 °C, diffusion coefficients were stable over time across wells (Fig. 4.1a). Time-averaged well-wise diffusion values (mean over time points) spanned  $D \approx 0.21$ - $0.26 \mu\text{m}^2 \text{s}^{-1}$ . Slopes were weakly positive on average ( $\bar{m} = 1.27 \times 10^{-4} \mu\text{m}^2 \text{s}^{-1} \text{min}^{-1}$ , mean,  $n = 4$ ) and did not differ significantly from zero (t-test:  $p = 0.110$ ).

At 37 °C, diffusion coefficients were higher overall (Fig. 4.1b), with time-averaged well-wise values (mean over time points) spanning  $D \approx 0.34$ - $0.47 \mu\text{m}^2 \text{s}^{-1}$ . Slopes were centered near zero ( $\bar{m} = 1.83 \times 10^{-5} \mu\text{m}^2 \text{s}^{-1} \text{min}^{-1}$ , mean,  $n = 4$ , t-test:  $p = 0.920$ ), indicating no systematic temporal drift.

Slope distributions did not differ significantly between temperatures (Welch's  $t$ -test:  $p = 0.573$ ). Thus, L2V exhibited higher absolute diffusion at 37 °C while remaining temporally stable at both temperatures.

Mobility-class population trends (Fig. 4.2, Fig. 4.3) showed that the immobile and fast fractions remained within comparatively narrow ranges but with pronounced SLB-to-SLB variability. At 26 °C, the immobile fraction at  $t_0$  ranged from roughly  $\sim 8$ -17% depending on the SLB and exhibited both slight increases and decreases over time (e.g.,  $m = -0.018 \pm 0.01$  to  $m = 0.024 \pm 0.04$  %/min, mean  $\pm$  SEM). The fast fraction was generally smaller at  $t_0$  but could increase substantially in some wells (e.g., up to  $m = 0.057 \pm 0.03$  %/min, mean  $\pm$  SEM). At 37 °C, the fast fraction constituted a substantial part of the trajectory population already at  $t_0$  (typically  $\sim 17$ -29%) and showed bilayer-dependent increases or decreases over time (e.g.,  $m = -0.058 \pm 0.001$  to  $m = 0.10 \pm 0.03$  %/min, mean  $\pm$  SEM). The immobile fraction remained comparatively small (approximately  $\sim 5$ -9%) and likewise displayed SLB-dependent temporal trends. Overall, while mean  $D(t)$  was stable, trajectory-level mobility composition could shift substantially in a bilayer-dependent manner.

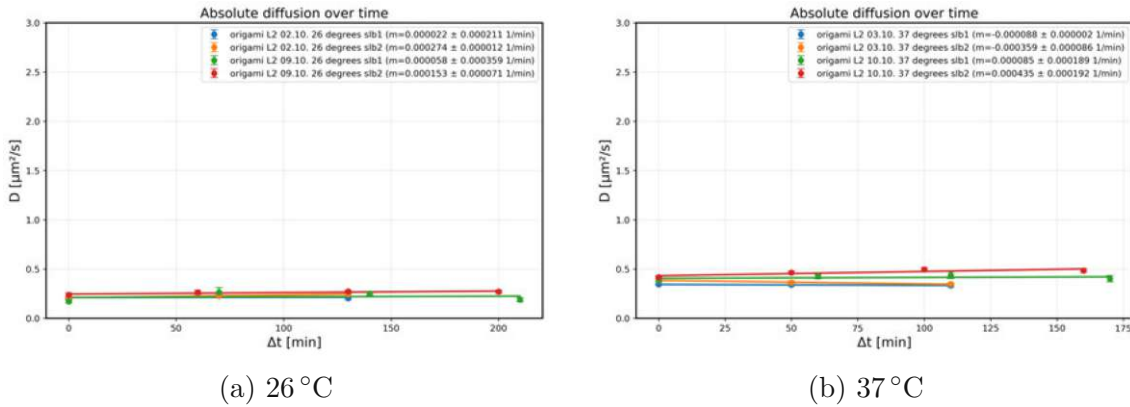
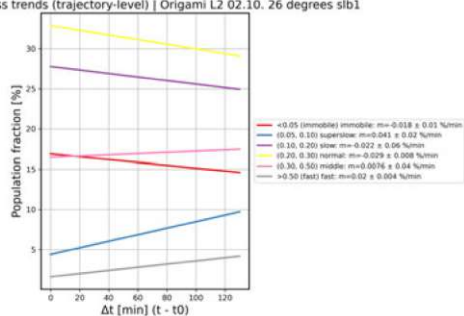


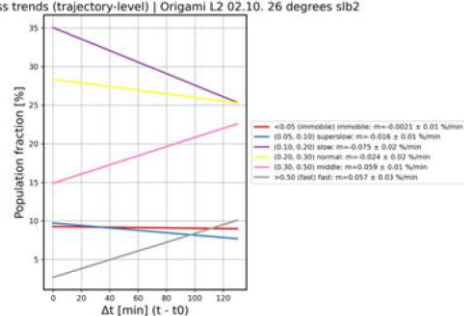
Figure 4.1.: **Absolute diffusion coefficients  $D(t)$  for L2V DNA origami platforms at 26 °C and 37 °C.** Solid lines indicate well-wise linear regressions.

Mobility-class trends (trajectory-level) | Origami L2 02.10. 26 degrees s1b1



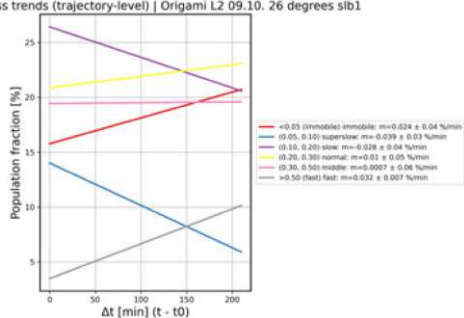
(a) SLB 1, 02/10

Mobility-class trends (trajectory-level) | Origami L2 02.10. 26 degrees s1b2



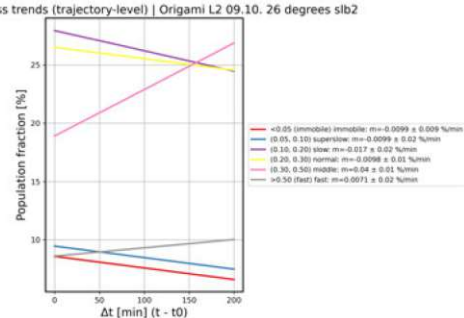
(b) SLB 2, 02/10

Mobility-class trends (trajectory-level) | Origami L2 09.10. 26 degrees s1b1



(c) SLB 1, 09/10

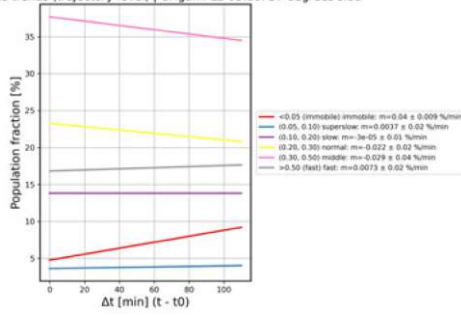
Mobility-class trends (trajectory-level) | Origami L2 09.10. 26 degrees s1b2



(d) SLB 2, 09/10

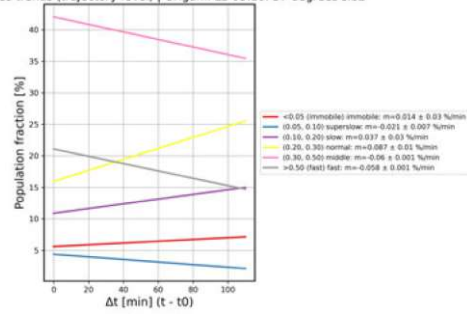
Figure 4.2.: Trajectory-level mobility-class population fractions for L2V at 26 °C across all supported lipid bilayers. Fractions were computed from all trajectories (all positions) at each measurement time point.

Mobility-class trends (trajectory-level) | Origami L2 03.10. 37 degrees sib1



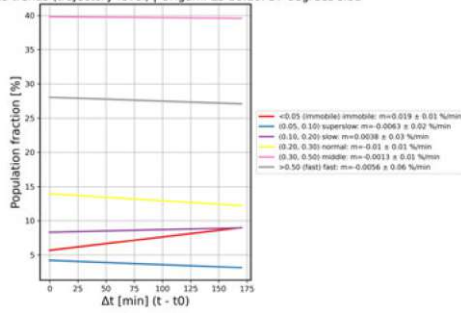
(a) SLB 1, 03/10

Mobility-class trends (trajectory-level) | Origami L2 03.10. 37 degrees sib2



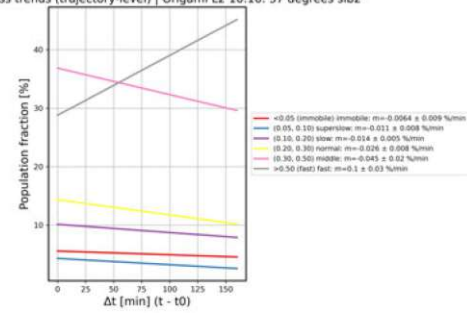
(b) SLB 2, 03/10

Mobility-class trends (trajectory-level) | Origami L2 10.10. 37 degrees sib1



(c) SLB 1, 10/10

Mobility-class trends (trajectory-level) | Origami L2 10.10. 37 degrees sib2



(d) SLB 2, 10/10

Figure 4.3.: **Trajectory-level mobility-class population fractions for L2V at 37°C across all supported lipid bilayers.** Fractions were computed from all trajectories (all positions) at each measurement time point.

#### 4.1.2. L1V

Figure 4.4 shows  $D(t)$  traces and well-wise regressions for L1V platforms.

At 26°C, diffusion coefficients showed a small but consistent increase over time (Fig. 4.4a). Time-averaged well-wise diffusion values (mean  $\pm$  SEM over time points) were  $D = 0.440 \pm 0.016$  and  $0.431 \pm 0.022 \mu\text{m}^2 \text{s}^{-1}$  (overall mean =  $0.435 \pm 0.005 \mu\text{m}^2 \text{s}^{-1}$ ). The mean well-wise slope was  $\bar{m} = 4.09 \times 10^{-4} \mu\text{m}^2 \text{s}^{-1} \text{min}^{-1}$  and differed significantly from zero (t-test:  $p = 0.013$ ,  $n = 2$ ).

At 37°C, diffusion coefficients were more heterogeneous across wells (Fig. 4.4b). Time-averaged well-wise diffusion values (mean  $\pm$  SEM over time points) were  $D = 0.398 \pm 0.014$  and  $0.553 \pm 0.131 \mu\text{m}^2 \text{s}^{-1}$  (overall mean =  $0.476 \pm 0.077 \mu\text{m}^2 \text{s}^{-1}$ ). Slopes were positive on average ( $\bar{m} = 1.38 \times 10^{-3} \mu\text{m}^2 \text{s}^{-1} \text{min}^{-1}$ ) but did not differ significantly from zero ( $p = 0.507$ ,  $n = 2$ ).

Well-wise slope distributions did not differ significantly between temperatures (Welch's t-test:  $p = 0.616$ ). Thus, absolute diffusion was comparable across temperatures, while temporal changes in mean  $D(t)$  remained weak overall, with increased well-to-well variability at 37°C.

Mobility-class population trends (Fig. 4.5, Fig. 4.6) showed that the immobile fraction ( $D < 0.05 \mu\text{m}^2 \text{s}^{-1}$ ) was low at both temperatures (on the order of a few percent). At  $26^\circ\text{C}$ , the immobile fraction decreased slightly over time in both SLBs (SLB1:  $m = -0.0082 \pm 0.005$ ; SLB2:  $m = -0.0074 \pm 0.008 \%$ /min, mean  $\pm$  SEM), while the fast fraction ( $D > 0.50 \mu\text{m}^2 \text{s}^{-1}$ ) increased in both SLBs (SLB1:  $m = 0.055 \pm 0.03$ ; SLB2:  $m = 0.072 \pm 0.03 \%$ /min, mean  $\pm$  SEM). At  $37^\circ\text{C}$ , population trends diverged between SLBs: in SLB1, both immobile and fast fractions changed only weakly (immobile:  $m = 0.0084 \pm 0.03$ ; fast:  $m = 0.0045 \pm 0.05 \%$ /min, mean  $\pm$  SEM), whereas in SLB2 the immobile fraction decreased (SLB2:  $m = -0.027 \pm 0.01 \%$ /min) and the fast fraction increased strongly (SLB2:  $m = 0.13 \pm 0.2 \%$ /min). Overall, population-level mobility composition revealed higher well-to-well variability at  $37^\circ\text{C}$ , ranging from nearly stable immobile/fast fractions (SLB1) to a pronounced shift towards the fast fraction (SLB2).

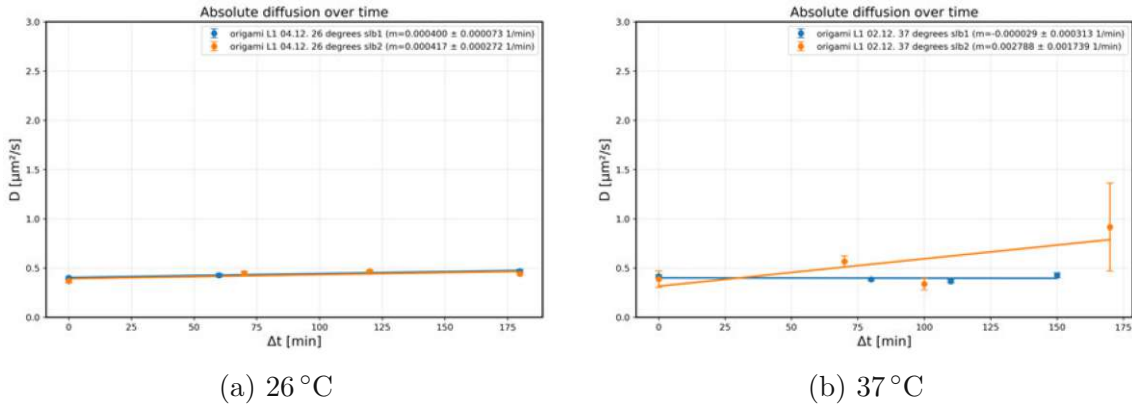


Figure 4.4.: **Absolute diffusion coefficients  $D(t)$  for L1V DNA origami platforms at  $26^\circ\text{C}$  and  $37^\circ\text{C}$ .** Solid lines indicate well-wise linear regressions.

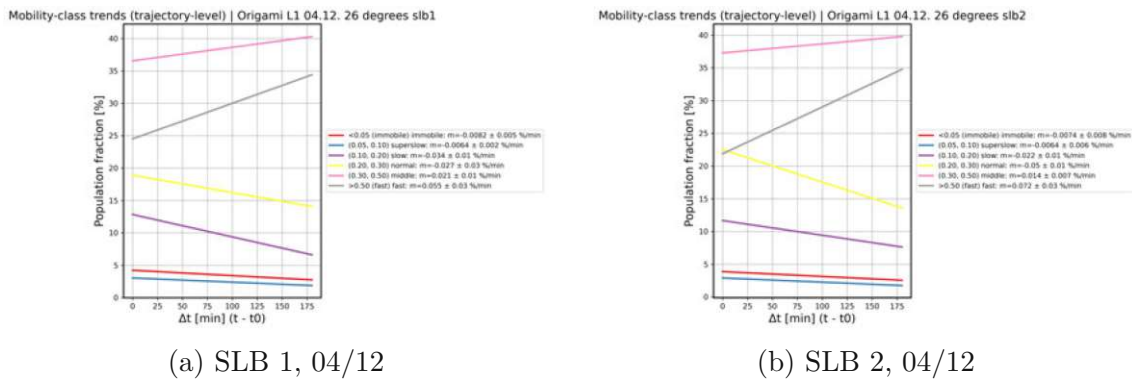
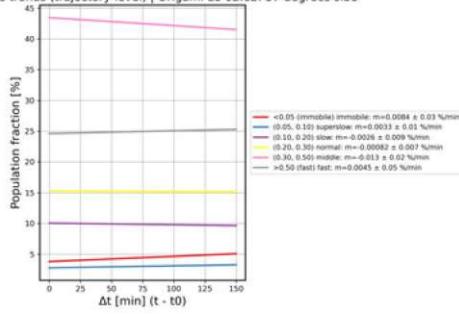


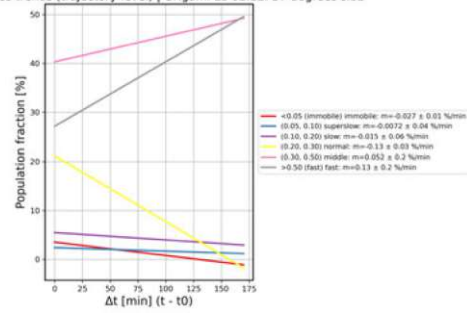
Figure 4.5.: **Diffusion population trends of L1V at  $26^\circ\text{C}$  across all supported lipid bilayers.**

Mobility-class trends (trajectory-level) | Origami L1 02.12. 37 degrees sib1



(a) SLB 1, 02/12

Mobility-class trends (trajectory-level) | Origami L1 02.12. 37 degrees sib2



(b) SLB 2, 02/12

Figure 4.6.: Diffusion population trends of L1V at 37°C across all supported lipid bilayers.

### 4.1.3. pMHC

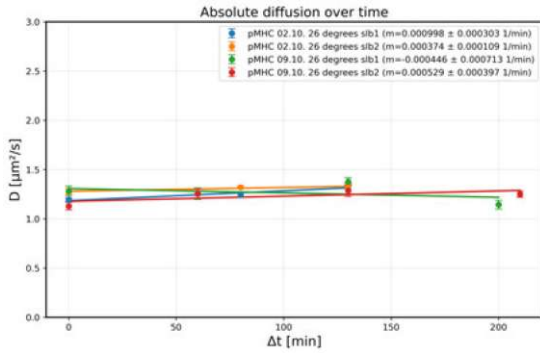
Figure 4.7 shows  $D(t)$  traces and well-wise regressions for pMHC.

At 26°C, diffusion coefficients were stable over time and narrowly distributed across wells (Fig. 4.7a). Mean well-wise diffusion values ranged from 1.23 to 1.31  $\mu\text{m}^2 \text{s}^{-1}$  (overall mean  $\pm SEM = 1.27 \pm 0.02 \mu\text{m}^2 \text{s}^{-1}$ ). Slopes were small and positive on average ( $\bar{m} = 3.64 \times 10^{-4} \mu\text{m}^2 \text{s}^{-1} \text{min}^{-1}$ ) and not significantly different from zero ( $p = 0.313$ ,  $n = 4$ ).

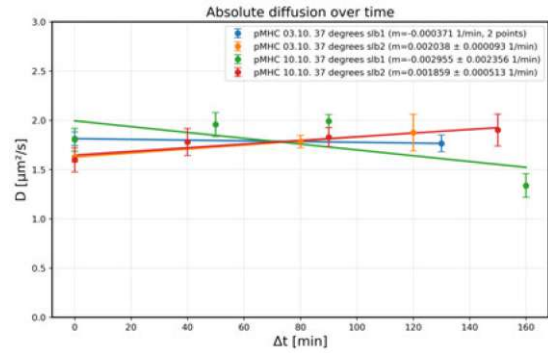
At 37°C, diffusion coefficients were higher (Fig. 4.7b), with mean well-wise values around 1.77-1.78  $\mu\text{m}^2 \text{s}^{-1}$  (overall mean  $\pm SEM = 1.78 \pm 0.01 \mu\text{m}^2 \text{s}^{-1}$ ). Slopes were centered near zero ( $\bar{m} = 1.43 \times 10^{-4} \mu\text{m}^2 \text{s}^{-1} \text{min}^{-1}$ ,  $p = 0.911$ ,  $n = 4$ ), indicating no systematic temporal drift.

Slope distributions did not differ significantly between temperatures (Welch's t-test:  $p = 0.865$ ). Thus, pMHC exhibited consistently higher absolute diffusion at 37°C while remaining temporally stable at both temperatures.

Mobility-class population trends (Fig. 4.8, Fig. 4.9) showed that the immobile fraction was consistently small across all wells (roughly  $\sim 1$ -4%). At 26°C, immobile trajectories were mostly stable to slightly increasing (e.g.,  $m = 0.00077 \pm 0.004$  to  $0.017 \pm 0.01 \%$ /min), while the fast fraction remained low (typically  $\sim 3$ -7%) and changed only weakly, with one well showing a decrease ( $m = -0.014 \pm 0.01 \%$ /min). At 37°C, the immobile fraction remained comparably small but exhibited both weak increases and decreases depending on the well (e.g.,  $m = -0.013 \pm 0.002$  to  $0.017 \pm 0.007 \%$ /min). In contrast, the fast fraction was substantially larger at 37°C (roughly  $\sim 8$ -21%) and showed pronounced well-to-well variability, including clear increases in some wells ( $m = 0.027 \pm 0.02$  and  $0.074 \pm 0.001 \%$ /min) and decreases in others ( $m = -0.053 \pm 0.07$  and  $-0.048 \%$ /min).

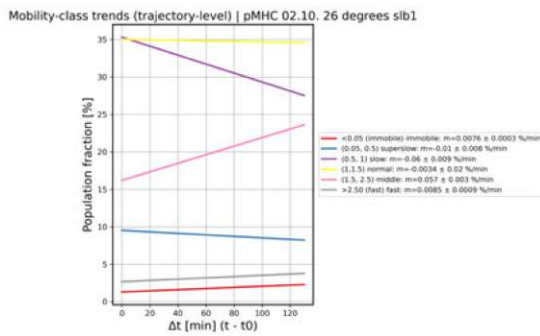


(a) 26 °C

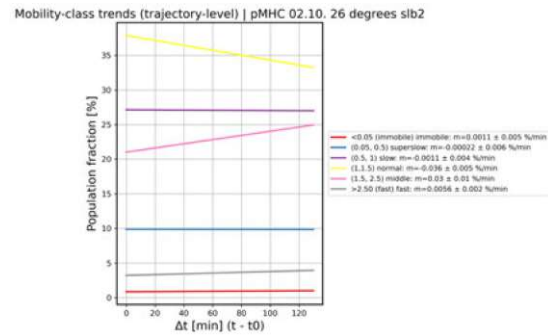


(b) 37 °C

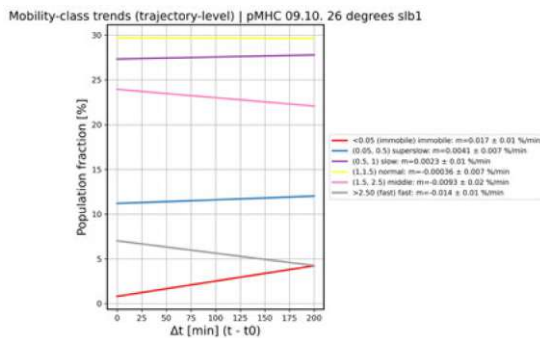
Figure 4.7.: Absolute diffusion coefficients  $D(t)$  for pMHC molecules at 26 °C and 37 °C. Solid lines indicate well-wise linear regressions.



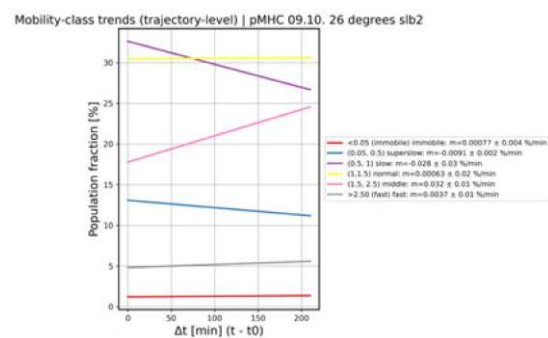
(a) SLB 1, 02/10



(b) SLB 2, 02/10



(c) SLB 1, 09/10



(d) SLB 2, 09/10

Figure 4.8.: Diffusion population trends of pMHC at 26 °C across all supported lipid bilayers.

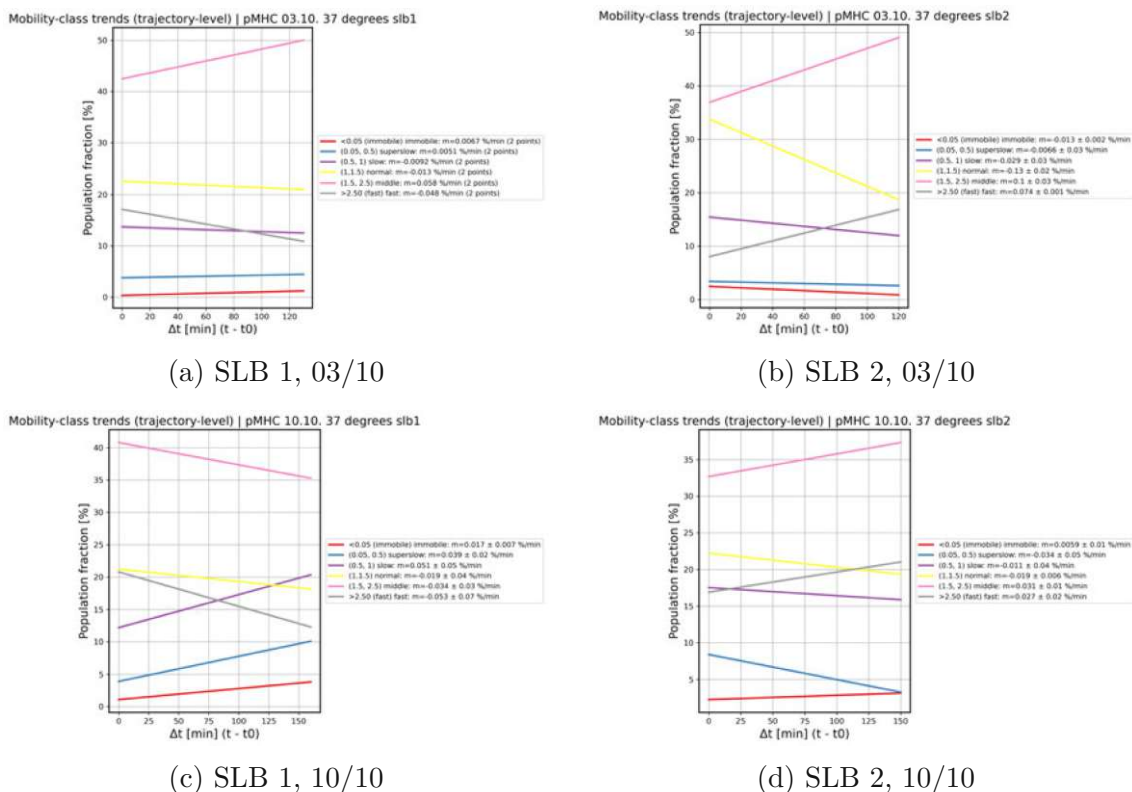


Figure 4.9.: Diffusion population trends of pMHC at 37°C across all supported lipid bilayers.

## 4.2. Temporal stability of intensity

Temporal stability of membrane-associated fluorophores was assessed from mean bulk fluorescence intensities. Intensities were normalized to the initial time point, and temporal trends were summarized per well by the slope of a linear regression of  $I_{rel}(t)$  versus elapsed measurement time. To relate bulk signals to approximate surface coverage, an initial surface density estimate  $\rho(t_0)$  was calculated for each well from the ratio of background-corrected bulk intensity at  $t_0$  to the corresponding single-molecule brightness (Eq. 3.4). Temperature effects were evaluated by comparing the distributions of well-wise slopes between 26°C and 37°C (Welch's t-test). Exemplary fluorescence microscopy images are shown in Fig. 4.10.

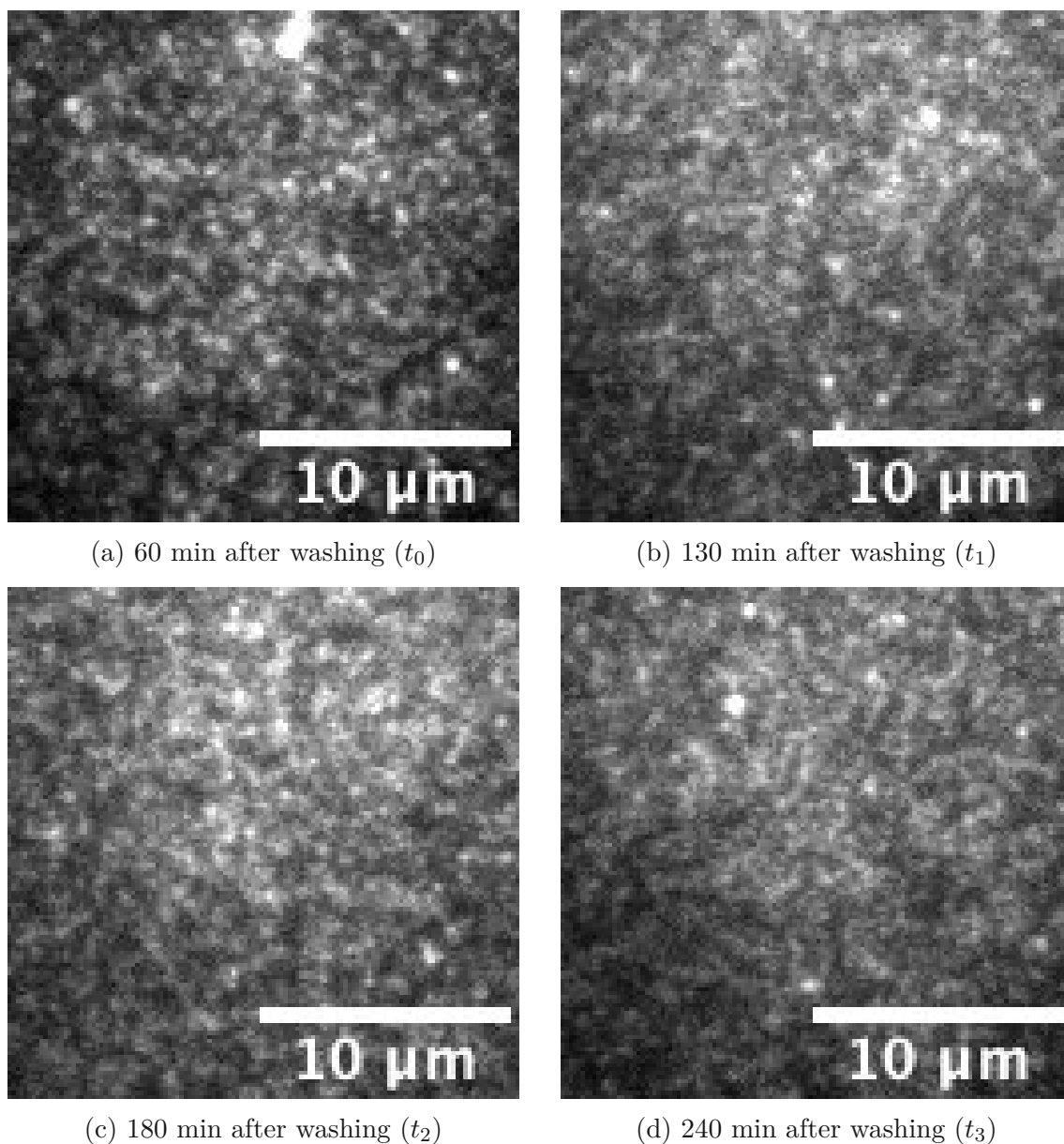


Figure 4.10.: **Pictures of SLB2 seeded with 400 ng L2V at 37°C over time on 10.10.2025.** Each panel shows the first frame of position 1 in the well. Brightness and contrast were adjusted identically across panels for visualization only; quantitative intensity analysis was performed on unadjusted pixel values within the defined ROI.

#### 4.2.1. L2V

Figure 4.11 shows  $I_{\text{rel}}(t)$  and well-wise regressions for L2V platforms.

At 26 °C, initial seeded surface densities ranged from 22.0 to 64.0 molecules/ $\mu\text{m}^2$ , with  $\bar{\rho}(t_0) = 43.1 \pm 8.64$  molecules/ $\mu\text{m}^2$  (mean  $\pm$  SEM,  $n = 4$ ). Normalized intensity decreased consistently across wells (Fig. 4.11a), yielding a mean slope of  $\bar{m} = -1.40 \times 10^{-3} \text{ min}^{-1}$  that differed from zero ( $p = 0.017$ ).

At 37 °C, initial densities showed a broader spread (14.2-55.8 molecules/ $\mu\text{m}^2$ ;  $\bar{\rho}(t_0) = 36.5 \pm 9.2$  molecules/ $\mu\text{m}^2$ ,  $n = 4$ ). Intensity traces exhibited a negative trend on average but varied substantially between wells (Fig. 4.11b); accordingly, the mean slope ( $\bar{m} = -1.18 \times 10^{-3} \text{ min}^{-1}$ ) was not significantly different from zero ( $p = 0.369$ ).

Well-wise slopes did not differ significantly between temperatures (Welch's t-test:  $p = 0.863$ ). Thus, while intensity loss was robust at 26 °C, the data do not indicate a clear temperature dependence of the decay rate.

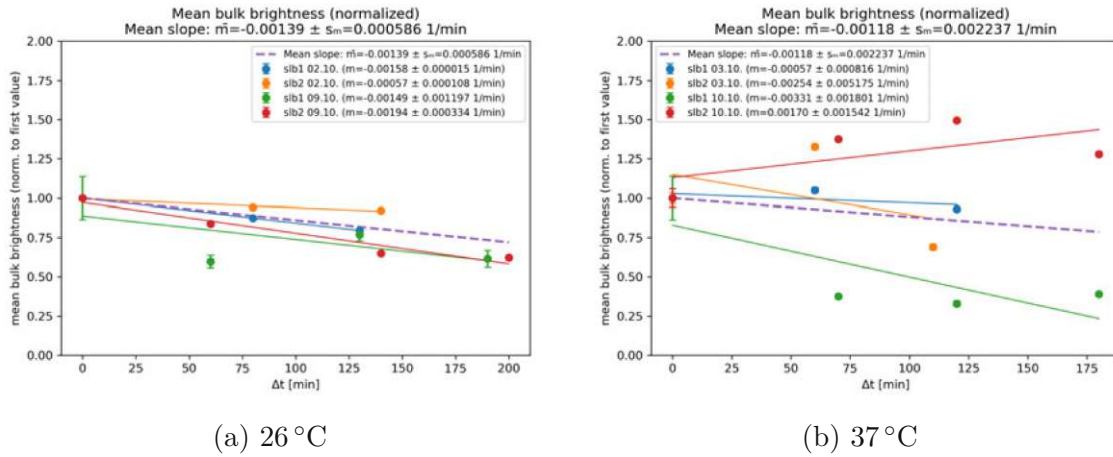


Figure 4.11.: Normalized bulk fluorescence intensity  $I_{\text{rel}}(t)$  for L2V DNA origami platforms at 26 °C and 37 °C. Dashed lines indicate the mean well-wise regression slope per temperature condition.

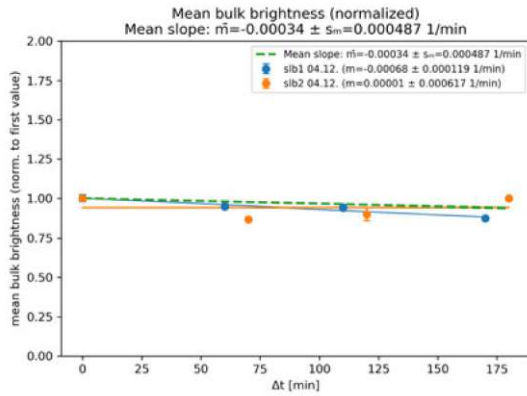
#### 4.2.2. L1V

Figure 4.12 summarizes  $I_{\text{rel}}(t)$  traces for L1V platforms.

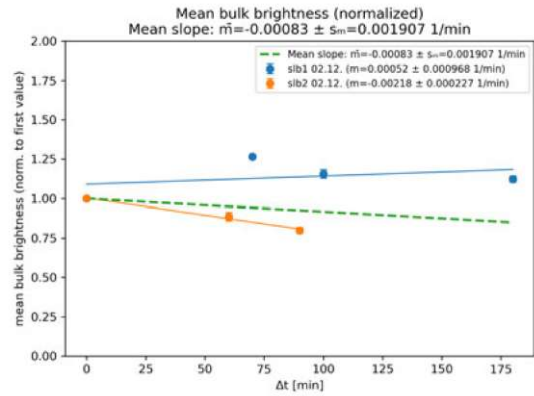
At 26 °C, initial seeded surface densities ranged from 19.7 to 22.5 molecules/ $\mu\text{m}^2$ , yielding  $\bar{\rho}(t_0) = 21.1 \pm 1.4$  molecules/ $\mu\text{m}^2$  (mean  $\pm$  SEM,  $n = 2$ ). Normalized intensity showed only a weak negative trend (Fig. 4.12a), with a mean slope of  $\bar{m} = -3.35 \times 10^{-4} \text{ min}^{-1}$  that did not differ from zero ( $p = 0.51$ ).

At 37 °C, initial densities ranged from 13.5 to 24.6 molecules/ $\mu\text{m}^2$ , with  $\bar{\rho}(t_0) = 19.1 \pm 5.6$  molecules/ $\mu\text{m}^2$  ( $n = 2$ ). No consistent temporal trend was observed across wells (Fig. 4.12b); the mean slope was  $\bar{m} = -8.30 \times 10^{-4} \text{ min}^{-1}$  and was not significant ( $p = 0.65$ ).

Slope distributions did not differ significantly between temperatures (Welch's t-test:  $p = 0.78$ ). Overall, L1V bulk fluorescence remained stable within the measurement variability and sample size.



(a) 26 °C



(b) 37 °C

Figure 4.12.: Normalized bulk fluorescence intensity  $I_{\text{rel}}(t)$  for L1V DNA origami platforms at 26 °C and 37 °C. Dashed lines indicate the mean well-wise regression slope per temperature condition.

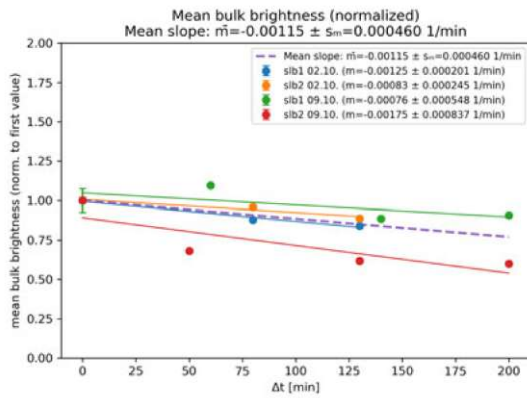
### 4.2.3. pMHC

Figure 4.13 shows  $I_{\text{rel}}(t)$  traces and well-wise regressions for pMHC.

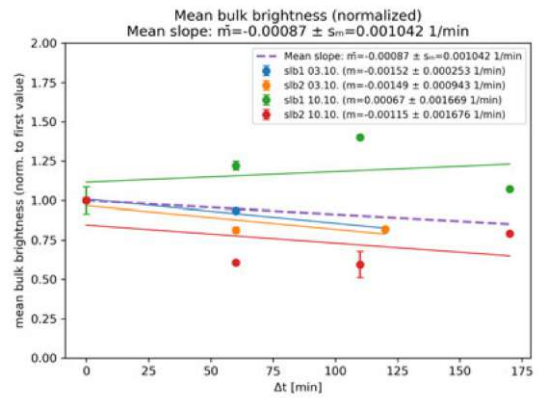
At 26 °C, initial seeded surface densities ranged from 6.1 to 84.1 molecules/ $\mu\text{m}^2$ , with  $\bar{\rho}(t_0) = 31.4 \pm 18.1$  molecules/ $\mu\text{m}^2$  (mean  $\pm$  SEM,  $n = 4$ ). Normalized intensity decreased consistently across wells (Fig. 4.13a), yielding a mean slope of  $\bar{m} = -1.15 \times 10^{-3} \text{ min}^{-1}$  that differed from zero ( $p = 0.015$ ).

At 37 °C, initial surface densities ranged from 2.6 to 22.2 molecules/ $\mu\text{m}^2$ , with  $\bar{\rho}(t_0) = 11.6 \pm 4.9$  molecules/ $\mu\text{m}^2$  ( $n = 4$ ). A negative trend was observed on average but varied between wells (Fig. 4.13b); correspondingly, the mean slope ( $\bar{m} = -8.73 \times 10^{-4} \text{ min}^{-1}$ ) was not significant ( $p = 0.193$ ).

Slope distributions did not differ significantly between temperatures (Welch's t-test:  $p = 0.653$ ). Thus, while pMHC intensity loss was robust at 26 °C, a temperature-dependent difference in decay rate was not supported by the data.



(a) 26 °C



(b) 37 °C

Figure 4.13.: Normalized bulk fluorescence intensity  $I_{rel}(t)$  for pMHC molecules at 26 °C and 37 °C. Dashed lines indicate the corresponding well-wise linear regression.

### 4.3. Temporal trends in single-molecule brightness

Single-molecule (SM) brightness was used as a quality-control readout to probe potential unresolved multi-emitter contributions in the localization data. Mean SM brightness  $I_{SM}$  was evaluated per well and time point from localization intensities, and temporal trends were summarized by well-wise linear regression slopes. Temperature-dependent effects were assessed by comparing slope distributions between 26 °C and 37 °C. Results are reported for L2V, L1V, and pMHC in turn, while detailed brightness-coded diagnostic plots are provided in the Appendix. Exemplary fluorescence microscopy images are shown in Fig. 4.14.

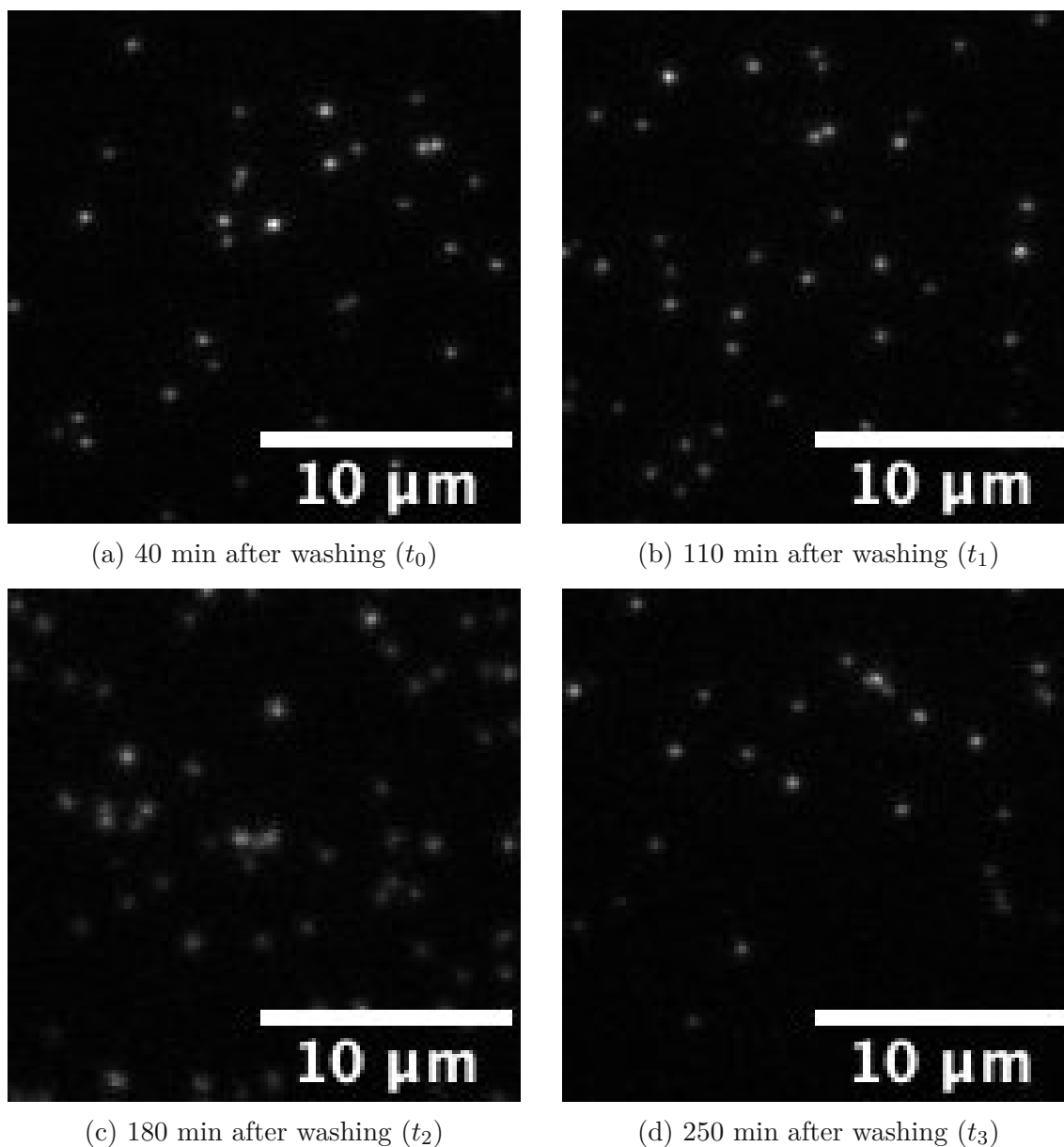


Figure 4.14.: **Pictures of SLB1 seeded with 20 ng L2V at 26 °C over time on 09.10.2025.** Each panel shows the first frame of position 1 in the well. Brightness and contrast were adjusted identically across panels for visualization only; quantitative intensity analysis was performed on unadjusted pixel values within the defined ROI.

### 4.3.1. L2V

Figure 4.15 shows the temporal evolution of mean single-molecule brightness  $I_{SM}$  for L2V platforms at 26 °C and 37 °C together with well-wise linear regressions. In Tab. A.1 and Tab. A.4 mean single-molecule brightness values for each timepoint can be seen.

At 26 °C, absolute mean brightness levels differed substantially between wells

(Fig. 4.15a). However, the well-wise temporal slopes were small, with the exception of SLB1 at the 9.10.2025, which had a highly negative slope of  $m = -8.759$  a.u. min<sup>-1</sup>, and individual mean brightnesses ranging from 4176.45–8969.88 a.u. (see Tab. A.1). The timecourse can be seen in Figure 4.15a. Individual slopes ranged from  $m = -8.759$  to 2.126 a.u. min<sup>-1</sup> (mean  $\bar{m} = -1.925305$  a.u. min<sup>-1</sup>).

At 37 °C, mean brightness values were overall lower than at 26 °C (Fig. 4.15b) and well-wise slopes were mixed but centered near zero, ranging from  $m = -10.37$  to 3.71 a.u. min<sup>-1</sup> (mean  $\bar{m} = -4.20$  a.u. min<sup>-1</sup>).

Overall, L2V measurements showed no systematic increase in mean SM brightness over time at either temperature.

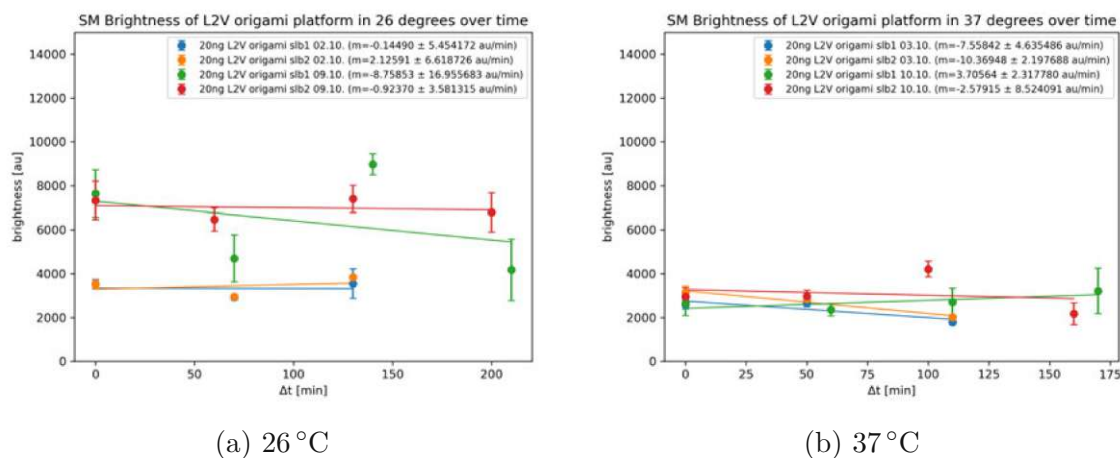


Figure 4.15.: Mean single molecule brightness  $I_{SM}$  of L2V DNA origami platforms at 26 °C and 37 °C. Solid lines indicate well-wise linear regressions.

### 4.3.2. L1V

Figure 4.16 shows the temporal evolution of mean single-molecule brightness  $I_{SM}$  for L1V platforms at 26 °C and 37 °C together with well-wise linear regressions. In Tab. A.2 and Tab. A.5 mean single-molecule brightness values for each timepoint can be seen.

At 26 °C, mean SM brightness values were in the range of  $\sim 8 \times 10^3$ - $1.1 \times 10^4$  a.u. and showed a slight increase over time in both wells (see table A.2 and Fig. 4.16a). The corresponding well-wise slopes were ranging from  $m = 0.23$  to 0.97 a.u. min<sup>-1</sup> (mean  $\bar{m} = 0.60$  a.u. min<sup>-1</sup>).

At 37 °C, mean SM brightness values were markedly lower (approximately  $\sim 1.5 \times 10^3$ - $2.2 \times 10^3$  a.u.; table A.5) and remained stable over time (see Fig. 4.16b). Well-wise slopes were close to zero, ranging from  $m = -1.34$  to 0.059 a.u. min<sup>-1</sup> (mean

$$\bar{m} = -0.64 \text{ a.u. min}^{-1}.$$

Overall, L1V platforms showed no systematic increase in mean SM brightness over time at either temperature.

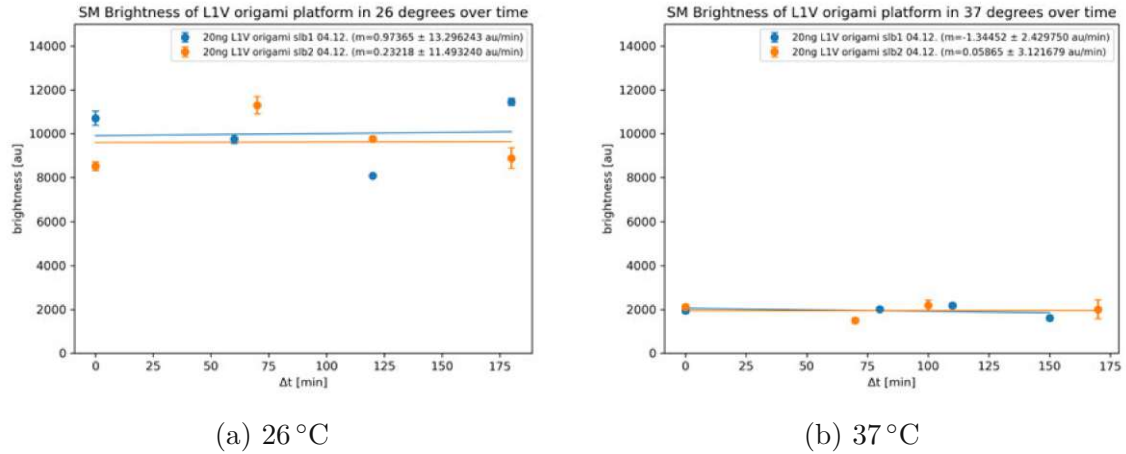


Figure 4.16.: Mean single molecule brightness  $I_{SM}$  of L1V DNA origami platforms at 26°C and 37°C. Solid lines indicate well-wise linear regressions.

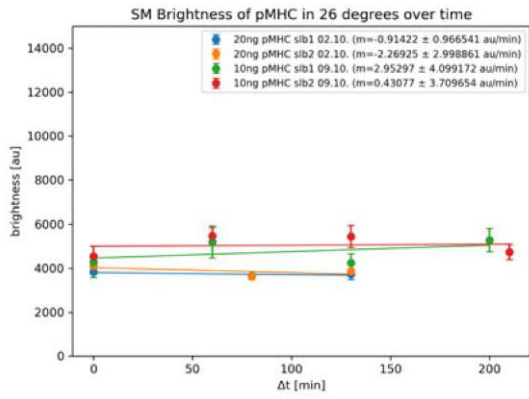
### 4.3.3. pMHC

Figure 4.17 shows the temporal evolution of mean single-molecule brightness  $I_{SM}$  for pMHC at 26°C and 37°C together with well-wise linear regressions.

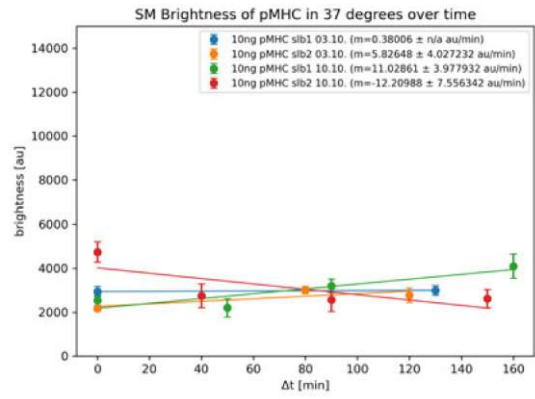
At 26°C, mean SM brightness values were in the range of approximately  $\sim 3.6 \times 10^3$ - $5.5 \times 10^3$  a.u. (Fig. 4.17a). Well-wise slopes were small and not consistently positive, ranging from  $m = -2.27$  to  $2.95 \text{ a.u. min}^{-1}$  (mean  $\bar{m} = 0.05 \text{ a.u. min}^{-1}$ ). Within this dataset, the two 20 ng wells (02/10) showed weakly negative slopes, whereas the two 10 ng wells (09/10) showed weakly positive slopes.

At 37°C, mean SM brightness values spanned approximately  $\sim 2.1 \times 10^3$ - $4.7 \times 10^3$  a.u. (Fig. 4.17b) and temporal slopes were mixed with larger magnitude. Slopes ranged from  $m = -12.21$  to  $11.03 \text{ a.u. min}^{-1}$  (mean  $\bar{m} = 1.26 \text{ a.u. min}^{-1}$ ). Thus, while individual wells exhibited noticeable increases or decreases in  $I_{SM}$  at 37°C, no consistent upward trend was observed across wells.

Overall, pMHC measurements showed no systematic increase in mean SM brightness over time at either temperature.



(a) 26 °C



(b) 37 °C

Figure 4.17.: Mean single molecule brightness  $I_{SM}$  of pMHC at 26 °C and 37 °C. Solid lines indicate well-wise linear regressions.

## 5. Discussion

SLB-based, APC-mimicking membrane model systems were examined with respect to their stability over time and as a function of temperature. Since these models are intended for studying T cell activation, they must remain stable and be able to present membrane tethered ligands with sufficient mobility throughout extended experiments conducted at physiological temperatures. The objective of this thesis was to assess bilayer stability under two distinct temperature conditions and temporal mobility of various ligands used to functionalize the SLBs.

### 5.1. Surface Density of Ligands

Because downstream T cell activation assays rely on defined ligand surface densities, it is important to assess how stable membrane-decorated SLBs remain over the relevant experimental timescales [5]. In this study, stability of surface presentation was evaluated by monitoring fluorescently labeled ligands on SLBs over time under constant acquisition settings. Bulk fluorescence intensity was used as a practical proxy for ligand surface coverage: stable intensities indicate preserved ligand density, whereas systematic changes are consistent with ligand loss, defect formation that reduces the fluorescent area, and/or redistribution within the analyzed region. Intensity trends are therefore interpreted as readouts of functional ligand persistence and are considered alongside diffusion measurements.

#### 5.1.1. L2V

At 26 °C, L2V platforms showed a small but consistent decay in bulk fluorescence intensity over time (Section 4.2.1), compatible with gradual ligand loss and/or minor defect formation that reduces the fluorescent area. At 37 °C, intensity trends were more heterogeneous and did not indicate a systematic acceleration of ligand detachment or bilayer destabilization. Overall, the absence of a clear temperature dependence together with pronounced well-to-well variability suggests that preparation-specific factors can dominate the bulk intensity readout.

### 5.1.2. L1V

At 26 °C, L1V platforms exhibited stable bulk fluorescence intensity over time (Section 4.2.2), consistent with preserved ligand surface coverage and no substantial defect formation within the observation window. At 37 °C, wells showed opposing intensity trends, resulting in no consistent group-level change. Similar to L2V, this pattern argues against a robust temperature-driven increase in ligand loss between 26 °C and 37 °C and highlights the contribution of well-specific variability.

### 5.1.3. pMHC

At 26 °C, pMHC-coated SLBs displayed a consistent decrease in bulk fluorescence intensity over time (Section 4.2.3), indicating a small net loss of surface-associated fluorescence within the measurement window. At 37 °C, intensity trends were heterogeneous across wells and did not reveal a systematic temperature-dependent change in mean intensity behavior. Thus, the present data do not support a temperature-driven acceleration of pMHC detachment or defect formation between 26 °C and 37 °C, while emphasizing preparation-dependent variability at elevated temperature.

A stronger temperature dependence has been reported for I-E<sup>k</sup> pMHC, with faster density loss at 37 °C than at 21 °C in HBSS imaging buffer [9]. Differences in pMHC construct, anchoring strategy, buffer composition, and the smaller temperature interval tested here provide plausible explanations for the differing sensitivity and underline the importance of standardized conditions when comparing stability across studies.

## 5.2. Lateral mobility and functional presentation

Besides stable ligand surface densities, SLBs must preserve lateral mobility to remain functionally relevant for T cell activation assays. As outlined in Section 3.6.2, diffusion facilitates receptor-ligand encounters and supports dynamic reorganization during synapse formation [25], [46], [47]. In the broader project context, SPT-derived diffusion coefficients therefore serve as a practical readout of whether ligands are presented in a mobile, APC-mimicking manner and are interpreted alongside the intensity-based stability analysis (Section 5.1).

### 5.2.1. L2V

L2V platforms remained laterally mobile at both temperatures and showed the expected increase in absolute diffusion at 37 °C (Fig. 4.1). Mean  $D(t)$  exhibited no

systematic temporal drift, arguing against progressive immobilization within the observation window. At the population level, however, the relative abundance of immobile and fast trajectories varied substantially between SLBs (Figs. 4.2 and 4.3), indicating bilayer- and day-dependent redistribution of mobility states. Overall, temperature primarily shifted absolute mobility, whereas the mobility-class composition was dominated by preparation-specific variability.

### 5.2.2. L1V

L1V platforms exhibited robust mobility under both temperature conditions (Fig. 4.4) without evidence for time-dependent immobilization. At 26 °C, diffusion increased slightly over time, consistent with a modest redistribution towards faster trajectories while the immobile fraction remained low. At 37 °C, absolute diffusion was comparable overall but showed pronounced well-to-well variability, ranging from largely stable mobility-class fractions to a strong shift towards fast trajectories (Fig. 4.6). Thus, as for L2V, preparation-specific factors can strongly affect population-level mobility features, particularly at elevated temperature.

### 5.2.3. pMHC

pMHC molecules displayed high mobility and temporal stability at both temperatures, with consistently higher absolute diffusion at 37 °C (Fig. 4.7). Mean  $D(t)$  showed no systematic drift, and the immobile fraction remained small across conditions, indicating predominantly mobile presentation over the investigated timescales. At 37 °C, the fast fraction was larger but varied between SLBs, again highlighting preparation-dependent redistribution of mobility states. In contrast to the observations reported by Gaugutz, no pronounced time-dependent increase of an immobile pMHC fraction consistent with substantial aggregation was detected within the sensitivity of the present analysis [9].

## 5.3. Integrated interpretation of surface presentation and mobility

Taken together, the intensity- and diffusion-based readouts suggest that, within the investigated time window, the dominant stability limitation is not a progressive loss of lateral mobility but rather preparation-dependent changes in effective surface coverage. For L2V and pMHC, diffusion remained stable while bulk fluorescence intensity decreased at 26 °C, which is more consistent with net ligand loss and/or

defect-related loss of fluorescent area than with gradual immobilization. L1V showed stable intensity and robust mobility, indicating a comparatively resilient presentation under the tested conditions. Across all ligand types, the increased heterogeneity at 37 °C points to well- and day-specific factors as major contributors, emphasizing the need for standardized preparation and sufficient replicate numbers when relating SLB readouts to downstream activation thresholds.

## 5.4. Methodological considerations and quality control

### 5.4.1. Quality control: single-molecule brightness

Single-molecule brightness was evaluated as a quality-control metric to assess whether unresolved multi-emitter contributions could systematically bias the localization-based analysis. Across L2V, pMHC, no condition showed a consistent time-dependent increase in mean single-molecule brightness across all wells at either 26 °C or 37 °C (Section 4.3). L1V platforms showed a minimal increase in single molecule brightness over time at 26 °C, which is more likely explained by fluctuations than actual aggregation of molecules and was not visible at 37 °C. This argues against a dominant temperature-driven aggregation process that would manifest as progressively increasing apparent per-localization brightness. Accordingly, the diffusion and intensity trends are interpreted primarily in terms of changes in lateral dynamics and/or ligand surface coverage rather than systematic fluorophore clustering effects.

In practice, mean single-molecule brightness fluctuated noticeably in several datasets (see Section A.3), most prominently for L2V at 26 °C (Tab. A.1). For L2V, construct-specific factors can additionally contribute to apparent brightness variability: platforms nominally carry two fluorophores, and despite using late frames to bias toward single-emitter conditions (Section 3.6.1), residual multi-emitter contributions cannot be excluded in all datasets. Because the fluorophores are in close proximity, two remaining emitters can contribute within one diffraction-limited spot and be recorded as a single localization with elevated apparent brightness.

### 5.4.2. Excitation stability and normalization of intensity trends

A key technical contributor to brightness and bulk-intensity variability is fluctuation of the effective excitation power density at the sample plane. In fluorescence microscopy, measured signal levels depend directly on illumination conditions; thus,

changes in excitation power can translate into changes in measured fluorescence intensity [54]. Day-to-day differences in absolute single-molecule brightness despite identical nominal laser attenuation (e.g., L2V at 26 °C; Tab. A.1) are consistent with variations in effective excitation conditions (e.g., coupling/alignment or optical stability), which were not systematically monitored for all datasets. Measuring laser power (or power density at the sample) before and after each imaging run would therefore be preferable to document drift; in the present work, this was only implemented for the L1V measurements.

To reduce sensitivity to session-to-session fluctuations in absolute fluorescence levels and enable comparison across different days, bulk fluorescence time courses were analyzed in normalized form,  $I_{\text{rel}}(t) = I(t)/I(t_0)$ , i.e., normalized to the initial value at  $t_0$ . This approach emphasizes relative temporal changes within each measurement series that are more plausibly attributable to ligand loss, defect formation, or redistribution.

### 5.4.3. Determination of ligand surface densities

In principle, ligand surface densities can be inferred from quantitative fluorescence microscopy by mapping measured intensities to fluorophore densities under consistent acquisition settings and by comparison to appropriate standards [48]. In this work, surface densities at a given time point could be estimated by dividing background-corrected bulk fluorescence intensities by the corresponding single-molecule brightness according to Eq. 3.4. However, because single-molecule brightness varied substantially over time and between sessions (Section 5.4.1)-and because residual multi-emitter contributions cannot be fully excluded for L2V-density time courses, surface densities ( $\rho(t)$ ) would be sensitive to fluctuations in the brightness scale and could not be interpreted unambiguously as true ligand loss. Therefore, the stability analysis focuses on normalized bulk intensity trends as a practical proxy for relative changes in ligand surface coverage.

### 5.4.4. Verification of sample temperature

Because temperature is a key control parameter in this study, the effective sample temperature was monitored during imaging and is reported in the Appendix (Fig. A.1 and Fig. A.2). For the L2V and pMHC experiments, the temperature on 02.10. remained close to 26 °C throughout the measurement (aside from a brief deviation), whereas on 09.10. the sample was effectively closer to 27 °C with small fluctuations. Likewise, on 03.10. and 10.10. the effective high-temperature condition

was closer to 38 °C rather than 37 °C. For the L1V experiments, manually recorded checkpoints indicated temperatures of approximately 26 °C on 04.12. and around 36 °C on 02.12.

Transient deviations can arise from sample handling (e.g., during reapplication of immersion oil and subsequent mounting) and during the initial warm-up and equilibration phase after placing the sample on the microscope. Moreover, precise temperature control with the Tokai-HIT setup was practically challenging because the sample temperature depends on several individual heating elements that must be tuned jointly; even after setting the controller, the system required additional time to reach a stable equilibrium at the sample plane. Therefore, small deviations between nominal setpoints and effective sample temperatures cannot be fully excluded and may contribute to variability, particularly when interpreting subtle temperature-dependent effects.

# 6. Conclusion & Outlook

## 6.1. Conclusion

This thesis evaluated SLB-based, APC-mimicking membrane model systems with respect to their suitability for extended T cell activation assays, focusing on the functional persistence of ligand presentation over time and under elevated temperature conditions. The investigated membrane systems consisted of supported lipid bilayers composed of 98 % POPC and 2 % Ni-DGS-NTA lipids, which enable the attachment of membrane-tethered ligands while preserving lateral membrane fluidity. In this framework, pMHC molecules were anchored to the bilayer via a polyhistidine tag interacting with Ni-DGS-NTA lipids, whereas DNA origami nanostructures were tethered through cholesterol modifications.

Experiments were performed at 26 °C and 37 °C in 1× DPBS buffer, or in 1× DPBS supplemented with 10 mM MgCl<sub>2</sub> for DNA origami samples. Temporal stability was assessed over observation windows of approximately 120-200 minutes following washing of the SLBs, during which typically three to four measurements were acquired per bilayer.

Across the investigated test systems (L2V and L1V DNA origami platforms, and pMHC), the combined readouts indicate that ligand presentation remains largely stable over the relevant experimental timescales. Bulk fluorescence intensities did not show evidence for rapid or systematic loss of surface coverage, indicating that ligand densities remained largely preserved during the observation period. At the same time, single-particle tracking analysis demonstrated that diffusion coefficients remained stable over time, confirming sustained lateral mobility of membrane-tethered ligands without signs of progressive immobilization. In addition, the single-molecule brightness analysis did not reveal consistent time-dependent increases across wells or temperatures, providing no indication for a systematic build-up of aggregated or unresolved multi-emitter populations within the sensitivity of the present approach.

Conceptually, these findings support the use of the tested SLB-functionalization strategies as stable and mobile ligand display modules in longer-duration assays. The preservation of ligand mobility and the absence of rapid loss of surface coverage indi-

cate that the investigated SLB-based membrane systems provide sufficiently robust and temporally stable ligand presentation over experimentally relevant timescales. This temporal robustness supports their suitability as standardized platforms for T cell activation assays, where controlled surface densities and sustained lateral mobility are essential for probing activation thresholds and the dynamic organization of receptor–ligand interactions at the T cell interface.

## 6.2. Outlook

While the overall picture is consistent with stable and mobile ligand presentation, three limitations constrain the interpretation of subtle temperature-dependent effects in the present dataset. First, effective sample temperatures deviated from nominal setpoints on some measurement days and can fluctuate during handling and equilibration, complicating a strict comparison between “26 °C” and “37 °C” conditions. Second, day-to-day variability in excitation conditions can affect absolute fluorescence and brightness levels even under identical nominal settings, motivating normalized analysis of fluorescence time courses and emphasizing the value of routine laser power measurements at the sample plane. Third, replicate numbers were limited for some conditions, increasing sensitivity to preparation-specific outliers and reducing statistical power to detect small systematic trends.

Future work should therefore focus on increasing replicate numbers and strengthening experimental control and documentation of key boundary conditions. In particular, continuous temperature logging across all datasets and pre-/post-imaging laser power measurements would improve comparability between sessions and temperature conditions. With these controls in place, follow-up experiments could more sensitively test for small temperature effects on ligand persistence, and refine assay workflows to maximize reproducibility of ligand surface densities and mobility for physiological-temperature T cell activation studies.

# Bibliography

- [1] K. Murphy and C. Weaver, “Die angeborene immunität”, in *Janeway Immunologie*, K. Murphy and C. Weaver, Eds., 9th ed., Berlin, Heidelberg: Springer Berlin Heidelberg, 2018, pp. 47–93, ISBN: 978-3-662-56004-4. DOI: 10.1007/978-3-662-56004-4\_2. [Online]. Available: [https://doi.org/10.1007/978-3-662-56004-4\\_2](https://doi.org/10.1007/978-3-662-56004-4_2).
- [2] K. Murphy and C. Weaver, “Antigenerkennung durch b-zell- und t-zell-rezeptoren”, in *Janeway Immunologie*, K. Murphy and C. Weaver, Eds., 9th ed., Berlin, Heidelberg: Springer Berlin Heidelberg, 2018, pp. 177–220, ISBN: 978-3-662-56004-4. DOI: 10.1007/978-3-662-56004-4\_4. [Online]. Available: [https://doi.org/10.1007/978-3-662-56004-4\\_4](https://doi.org/10.1007/978-3-662-56004-4_4).
- [3] B. Alberts et al., *Molecular biology of the cell*, 7th ed. New York: W. W. Norton & Company, 2022, ISBN: 0-393-88485-6.
- [4] J. B. Huppa and M. M. Davis, “The interdisciplinary science of t-cell recognition”, in *Advances in Immunology*, F. W. Alt, Ed., vol. 119, Academic Press, 2013, pp. 1–50, ISBN: 0065-2776. DOI: 10.1016/B978-0-12-407707-2.00001-1. [Online]. Available: <https://www.sciencedirect.com/science/article/pii/B9780124077072000011>.
- [5] J. Hellmeier, “DNA origami as a nanoscale tool for t-cell activation”, Dissertation, Technische Universität Wien, Wien, 2020. DOI: <https://doi.org/10.34726/hss.2020.67861>.
- [6] J. Hellmeier et al., “DNA origami demonstrate the unique stimulatory power of single pMHCs as t cell antigens”, *Proceedings of the National Academy of Sciences*, vol. 118, no. 4, e2016857118, Jan. 26, 2021. DOI: 10.1073/pnas.2016857118. [Online]. Available: <https://doi.org/10.1073/pnas.2016857118>.
- [7] X. Su, J. A. Ditlev, M. K. Rosen, and R. D. Vale, “Reconstitution of TCR signaling using supported lipid bilayers”, *Methods in molecular biology (Clifton, N.J.)*, vol. 1584, pp. 65–76, 2017, ISSN: 1940-6029 1064-3745. DOI: 10.1007/978-1-4939-6881-7\_5.

- [8] J. Hellmeier, R. Platzter, J. B. Huppa, and E. Sevcsik, “A DNA origami-based biointerface to interrogate the spatial requirements for sensitized t-cell antigen recognition”, in *The Immune Synapse: Methods and Protocols*, C. T. Baldari and M. L. Dustin, Eds., New York, NY: Springer US, 2023, pp. 277–302, ISBN: 978-1-0716-3135-5. DOI: 10.1007/978-1-0716-3135-5\_18. [Online]. Available: [https://doi.org/10.1007/978-1-0716-3135-5\\_18](https://doi.org/10.1007/978-1-0716-3135-5_18).
- [9] A. Gaugutz, “Stability of functionalised supported lipid bilayers at ambient and physiological temperatures”, Diplomarbeit, Technische Universität Wien, 2022. DOI: 10.34726/hss.2022.97520.
- [10] Y.-H. M. Chan and S. G. Boxer, “Model membrane systems and their applications”, *Model systems/Biopolymers*, vol. 11, no. 6, pp. 581–587, Dec. 1, 2007, ISSN: 1367-5931. DOI: 10.1016/j.cbpa.2007.09.020. [Online]. Available: <https://www.sciencedirect.com/science/article/pii/S1367593107001457>.
- [11] R. P. Richter, R. Bérat, and A. R. Brisson, “Formation of solid-supported lipid bilayers: an integrated view”, *Langmuir*, vol. 22, no. 8, pp. 3497–3505, Apr. 1, 2006, ISSN: 0743-7463. DOI: 10.1021/la052687c. [Online]. Available: <https://doi.org/10.1021/la052687c>.
- [12] Z. Cournia et al., “Membrane protein structure, function, and dynamics: A perspective from experiments and theory”, *The Journal of Membrane Biology*, vol. 248, no. 4, pp. 611–640, Aug. 1, 2015, ISSN: 1432-1424. DOI: 10.1007/s00232-015-9802-0. [Online]. Available: <https://doi.org/10.1007/s00232-015-9802-0>.
- [13] K. Murphy and C. Weaver, “Wie antigene den t-lymphocyten präsentiert werden”, in *Janeway Immunologie*, K. Murphy and C. Weaver, Eds., 9th ed., Berlin, Heidelberg: Springer Berlin Heidelberg, 2018, pp. 273–326, ISBN: 978-3-662-56004-4. DOI: 10.1007/978-3-662-56004-4\_6. [Online]. Available: [https://doi.org/10.1007/978-3-662-56004-4\\_6](https://doi.org/10.1007/978-3-662-56004-4_6).
- [14] M. L. Dustin, “Supported bilayers at the vanguard of immune cell activation studies”, *Supported Membranes*, vol. 168, no. 1, pp. 152–160, Oct. 1, 2009, ISSN: 1047-8477. DOI: 10.1016/j.jsb.2009.05.007. [Online]. Available: <https://www.sciencedirect.com/science/article/pii/S1047847709001415>.
- [15] A. A. Brian and H. M. McConnell, “Allogeneic stimulation of cytotoxic t cells by supported planar membranes”, *Proceedings of the National Academy of Sciences*, vol. 81, no. 19, pp. 6159–6163, 1984. DOI: 10.1073/pnas.81.19.

6159. [Online]. Available: <https://www.pnas.org/doi/abs/10.1073/pnas.81.19.6159>.

- [16] K. H. Biswas and J. T. Groves, “Hybrid live cell-supported membrane interfaces for signaling studies”, *Annual Review of Biophysics*, vol. 48, pp. 537–562, Apr. 3, 2019, Type: Journal Article, ISSN: 1936-1238. DOI: <https://doi.org/10.1146/annurev-biophys-070317-033330>. [Online]. Available: <https://www.annualreviews.org/content/journals/10.1146/annurev-biophys-070317-033330>.
- [17] D. Axelrod, “Total internal reflection fluorescence microscopy”, in *Methods in Cellular Imaging*, A. Periasamy, Ed., New York, NY: Springer New York, 2001, pp. 362–380, ISBN: 978-1-4614-7513-2. DOI: 10.1007/978-1-4614-7513-2\_21. [Online]. Available: [https://doi.org/10.1007/978-1-4614-7513-2\\_21](https://doi.org/10.1007/978-1-4614-7513-2_21).
- [18] E. T. Castellana and P. S. Cremer, “Solid supported lipid bilayers: From biophysical studies to sensor design”, *Surface Science Reports*, vol. 61, no. 10, pp. 429–444, Nov. 15, 2006, ISSN: 0167-5729. DOI: 10.1016/j.surfrep.2006.06.001. [Online]. Available: <https://www.sciencedirect.com/science/article/pii/S0167572906000616>.
- [19] L. K. Tamm and H. M. McConnell, “Supported phospholipid bilayers”, *Bio-physical journal*, vol. 47, no. 1, pp. 105–113, Jan. 1985, ISSN: 0006-3495 1542-0086. DOI: 10.1016/S0006-3495(85)83882-0.
- [20] J. A. Jackman and N.-J. Cho, “Supported lipid bilayer formation: Beyond vesicle fusion”, *Langmuir*, vol. 36, no. 6, pp. 1387–1400, Feb. 18, 2020, ISSN: 0743-7463. DOI: 10.1021/acs.langmuir.9b03706. [Online]. Available: <https://doi.org/10.1021/acs.langmuir.9b03706>.
- [21] G. van Meer, D. R. Voelker, and G. W. Feigenson, “Membrane lipids: Where they are and how they behave”, *Nature Reviews Molecular Cell Biology*, vol. 9, no. 2, pp. 112–124, Feb. 1, 2008, ISSN: 1471-0080. DOI: 10.1038/nrm2330. [Online]. Available: <https://doi.org/10.1038/nrm2330>.
- [22] A. M. Mørch et al., “The kinase occupancy of t cell coreceptors reconsidered”, *Proceedings of the National Academy of Sciences*, vol. 119, no. 49, e2213538119, Nov. 1, 2022. DOI: 10.1073/pnas.2213538119. [Online]. Available: <https://www.pnas.org/doi/abs/10.1073/pnas.2213538119>.
- [23] “Avanti polar lipids”, 16:0-18:1 PC (POPC). [Online]. Available: <https://avantilipids.com/product/850457>.

- [24] S. Kim and C. Hyeon, “Location of the TEMPO moiety of TEMPO-PC in phosphatidylcholine bilayers is membrane phase dependent”, *Biophysical Journal*, vol. 121, no. 13, pp. 2550–2556, Jul. 5, 2022, ISSN: 0006-3495. DOI: 10.1016/j.bpj.2022.05.044. Accessed: Mar. 9, 2026. [Online]. Available: <https://doi.org/10.1016/j.bpj.2022.05.044>.
- [25] M. Edidin, “Rotational and lateral diffusion of membrane proteins and lipids: Phenomena and function”, in *Current Topics in Membranes and Transport*, F. Bronner, R. D. Klausner, C. Kempf, and J. v. Renswoude, Eds., vol. 29, Academic Press, Jan. 1, 1987, pp. 91–127, ISBN: 0070-2161. DOI: 10.1016/S0070-2161(08)60044-1. [Online]. Available: <https://www.sciencedirect.com/science/article/pii/S0070216108600441>.
- [26] A. Lopez and J. Liu, “DNA oligonucleotide-functionalized liposomes: Bioconjugate chemistry, biointerfaces, and applications”, *Langmuir*, vol. 34, no. 49, pp. 15 000–15 013, Dec. 11, 2018, ISSN: 0743-7463. DOI: 10.1021/acs.langmuir.8b01368. [Online]. Available: <https://doi.org/10.1021/acs.langmuir.8b01368>.
- [27] J. A. Nye and J. T. Groves, “Kinetic control of histidine-tagged protein surface density on supported lipid bilayers”, *Langmuir*, vol. 24, no. 8, pp. 4145–4149, Apr. 1, 2008, ISSN: 0743-7463, 1520-5827. DOI: 10.1021/la703788h. [Online]. Available: <https://pubs.acs.org/doi/10.1021/la703788h>.
- [28] “Avanti polar lipids”, 18:1 DGS-NTA(Ni). [Online]. Available: <https://avantilipids.com/product/790404>.
- [29] K. Terpe, “Overview of tag protein fusions: From molecular and biochemical fundamentals to commercial systems”, *Applied Microbiology and Biotechnology*, vol. 60, no. 5, pp. 523–533, Jan. 1, 2003, ISSN: 1432-0614. DOI: 10.1007/s00253-002-1158-6. [Online]. Available: <https://doi.org/10.1007/s00253-002-1158-6>.
- [30] E. Sulkowski, “Purification of proteins by IMAC”, *Trends in Biotechnology*, vol. 3, no. 1, pp. 1–7, Jan. 1, 1985, ISSN: 0167-7799. DOI: 10.1016/0167-7799(85)90068-X. [Online]. Available: <https://www.sciencedirect.com/science/article/pii/016777998590068X>.
- [31] E. Hochuli, W. Bannwarth, H. Döbeli, R. Gentz, and D. Stüber, “Genetic approach to facilitate purification of recombinant proteins with a novel metal chelate adsorbent”, *Bio/Technology*, vol. 6, no. 11, pp. 1321–1325, Nov. 1, 1988, ISSN: 1546-1696. DOI: 10.1038/nbt1188-1321. [Online]. Available: <https://doi.org/10.1038/nbt1188-1321>.

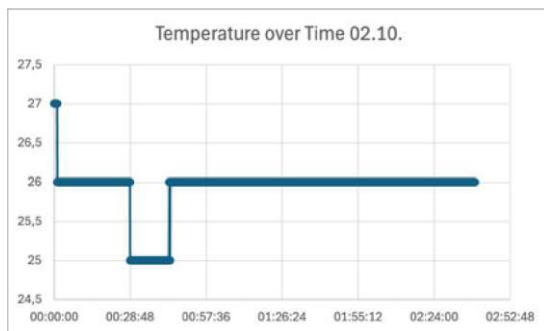
- [32] J. Crowe, H. Döbeli, R. Gentz, E. Hochuli, D. Stüber, and K. Henco, “6xHis-ni-NTA chromatography as a superior technique in recombinant protein expression/purification”, in *Protocols for Gene Analysis*, A. J. Harwood, Ed., Totowa, NJ: Humana Press, 1994, pp. 371–387, ISBN: 978-1-59259-518-1. DOI: 10.1385/0-89603-258-2:371. [Online]. Available: <https://doi.org/10.1385/0-89603-258-2:371>.
- [33] S. Knecht, D. Ricklin, A. N. Eberle, and B. Ernst, “Oligohis-tags: Mechanisms of binding to ni<sup>2+</sup>-NTA surfaces”, *Journal of Molecular Recognition*, vol. 22, no. 4, pp. 270–279, Jul. 1, 2009, ISSN: 0952-3499. DOI: 10.1002/jmr.941. [Online]. Available: <https://doi.org/10.1002/jmr.941>.
- [34] G. Raghunath and R. B. Dyer, “Kinetics of histidine-tagged protein association to nickel-decorated liposome surfaces”, *Langmuir*, vol. 35, no. 38, pp. 12 550–12 561, Sep. 24, 2019, ISSN: 0743-7463. DOI: 10.1021/acs.langmuir.9b01700. [Online]. Available: <https://doi.org/10.1021/acs.langmuir.9b01700>.
- [35] S. Magdeldin and A. Moser, “Affinity chromatography: Principles and applications”, in Mar. 2012, ISBN: 978-953-51-0325-7. DOI: 10.5772/39087.
- [36] D. Schalmer, “Optimizing a DNA origami-based model system to assess t-cell activation”, Diplomarbeit, Technische Universität Wien, Wien, Dec. 3, 2025. DOI: 10.34726/hss.2025.127860.
- [37] A. Czogalla, H. G. Franquelim, and P. Schwille, “DNA nanostructures on membranes as tools for synthetic biology”, *Biophysical Journal*, vol. 110, no. 8, pp. 1698–1707, Apr. 26, 2016, ISSN: 0006-3495. DOI: 10.1016/j.bpj.2016.03.015. Accessed: Mar. 9, 2026. [Online]. Available: <https://doi.org/10.1016/j.bpj.2016.03.015>.
- [38] A. Bunge et al., “Lipid membranes carrying lipophilic cholesterol-based oligonucleotides—characterization and application on layer-by-layer coated particles”, *The Journal of Physical Chemistry B*, vol. 113, no. 51, pp. 16 425–16 434, Dec. 24, 2009, ISSN: 1520-6106. DOI: 10.1021/jp9067747. [Online]. Available: <https://doi.org/10.1021/jp9067747>.
- [39] N. C. Seeman and H. F. Sleiman, “DNA nanotechnology”, *Nature Reviews Materials*, vol. 3, no. 1, p. 17 068, Nov. 8, 2017, ISSN: 2058-8437. DOI: 10.1038/natrevmats.2017.68. [Online]. Available: <https://doi.org/10.1038/natrevmats.2017.68>.

- [40] P. W. K. Rothemund, “Folding DNA to create nanoscale shapes and patterns”, *Nature*, vol. 440, no. 7082, pp. 297–302, Mar. 1, 2006, ISSN: 1476-4687. DOI: 10.1038/nature04586. [Online]. Available: <https://doi.org/10.1038/nature04586>.
- [41] M. Endo, K. Hidaka, T. Kato, K. Namba, and H. Sugiyama, “DNA prism structures constructed by folding of multiple rectangular arms”, *Journal of the American Chemical Society*, vol. 131, no. 43, pp. 15570–15571, Nov. 4, 2009, ISSN: 0002-7863. DOI: 10.1021/ja904252e. [Online]. Available: <https://doi.org/10.1021/ja904252e>.
- [42] E. S. Andersen et al., “Self-assembly of a nanoscale DNA box with a controllable lid”, *Nature*, vol. 459, no. 7243, pp. 73–76, May 1, 2009, ISSN: 1476-4687. DOI: 10.1038/nature07971. [Online]. Available: <https://doi.org/10.1038/nature07971>.
- [43] B. Saccà et al., “Orthogonal protein decoration of DNA origami”, *Angewandte Chemie International Edition*, vol. 49, no. 49, pp. 9378–9383, Oct. 28, 2010. DOI: <https://doi.org/10.1002/anie.201005931>. [Online]. Available: <https://onlinelibrary.wiley.com/doi/abs/10.1002/anie.201005931>.
- [44] S. T. Ross, S. Schwartz, T. J. Fellers, and M. W. Davidson. “Total internal reflection fluorescence (TIRF) microscopy”, [microscopyu.com](https://www.microscopyu.com/techniques/fluorescence/total-internal-reflection-fluorescence-tirf-microscopy). [Online]. Available: <https://www.microscopyu.com/techniques/fluorescence/total-internal-reflection-fluorescence-tirf-microscopy>.
- [45] H. Qian, M. P. Sheetz, and E. L. Elson, “Single particle tracking. analysis of diffusion and flow in two-dimensional systems”, *Biophysical Journal*, vol. 60, no. 4, pp. 910–921, Oct. 1, 1991, ISSN: 0006-3495. DOI: 10.1016/S0006-3495(91)82125-7. [Online]. Available: <https://www.sciencedirect.com/science/article/pii/S0006349591821257>.
- [46] L. J. Edwards, V. I. Zarnitsyna, J. D. Hood, B. Evavold, and C. Zhu, “Insights into t cell recognition of antigen: Significance of two-dimensional kinetic parameters”, *Frontiers in Immunology*, vol. 3, Apr. 20, 2012, ISSN: 1664-3224. DOI: 10.3389/fimmu.2012.00086. [Online]. Available: <https://www.frontiersin.org/journals/immunology/articles/10.3389/fimmu.2012.00086>.
- [47] C.-J. Hsu et al., “Ligand mobility modulates immunological synapse formation and t cell activation”, *PLOS ONE*, vol. 7, no. 2, e32398, Feb. 22, 2012. DOI: 10.1371/journal.pone.0032398. [Online]. Available: <https://doi.org/10.1371/journal.pone.0032398>.

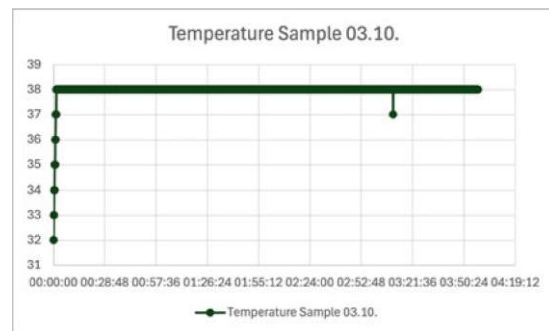
- [48] W. J. Galush, J. A. Nye, and J. T. Groves, “Quantitative fluorescence microscopy using supported lipid bilayer standards”, *Biophysical Journal*, vol. 95, no. 5, pp. 2512–2519, Sep. 1, 2008, ISSN: 0006-3495. DOI: 10.1529/biophysj.108.131540. Accessed: Mar. 9, 2026. [Online]. Available: <https://doi.org/10.1529/biophysj.108.131540>.
- [49] T. Dam, M. Chouliara, V. Junghans, and P. Jönsson, “Supported lipid bilayers and the study of two-dimensional binding kinetics”, *Frontiers in Molecular Biosciences*, vol. 9, Feb. 18, 2022, ISSN: 2296-889X. DOI: 10.3389/fmolb.2022.833123. [Online]. Available: <https://www.frontiersin.org/journals/molecular-biosciences/articles/10.3389/fmolb.2022.833123>.
- [50] P. G. Saffman and M. Delbrück, “Brownian motion in biological membranes”, *Proceedings of the National Academy of Sciences*, vol. 72, no. 8, pp. 3111–3113, Jun. 9, 1975. DOI: 10.1073/pnas.72.8.3111. [Online]. Available: <https://www.pnas.org/doi/abs/10.1073/pnas.72.8.3111>.
- [51] L. Schrangl, *Sdt-python: Python library for fluorescence microscopy data analysis*, 2020.
- [52] H. Babcock, Y. M. Sigal, and X. Zhuang, “A high-density 3d localization algorithm for stochastic optical reconstruction microscopy”, *Optical Nanoscopy*, vol. 1, no. 1, p. 6, Jul. 16, 2012, ISSN: 2192-2853. DOI: 10.1186/2192-2853-1-6. [Online]. Available: <https://doi.org/10.1186/2192-2853-1-6>.
- [53] Y. Gao and M. L. Kilfoil, “Accurate detection and complete tracking of large populations of features in three dimensions”, *Optics Express*, vol. 17, no. 6, pp. 4685–4704, Mar. 16, 2009. DOI: 10.1364/OE.17.004685. [Online]. Available: <https://opg.optica.org/oe/abstract.cfm?URI=oe-17-6-4685>.
- [54] M. A. Digman, R. Dalal, A. F. Horwitz, and E. Gratton, “Mapping the number of molecules and brightness in the laser scanning microscope”, *Biophysical Journal*, vol. 94, no. 6, pp. 2320–2332, Mar. 15, 2008, ISSN: 0006-3495. DOI: 10.1529/biophysj.107.114645. Accessed: Mar. 9, 2026. [Online]. Available: <https://doi.org/10.1529/biophysj.107.114645>.

# A. Supplementary Material

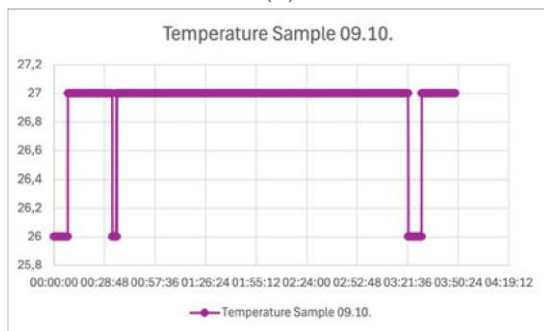
## A.1. Temperature Plots



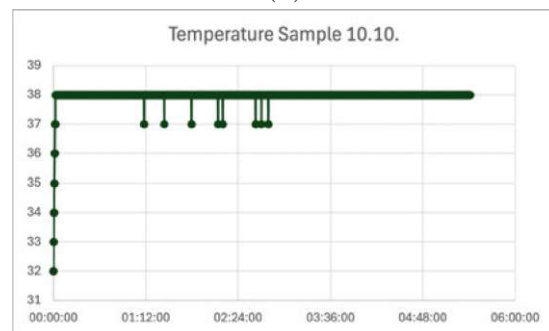
(a)



(b)

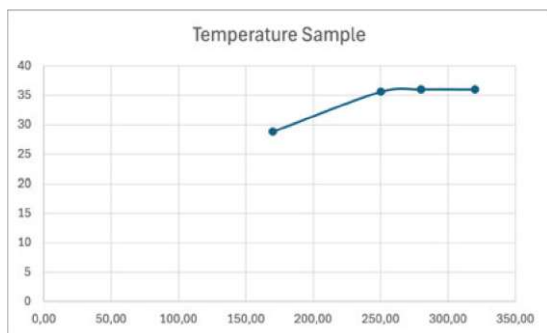


(c)

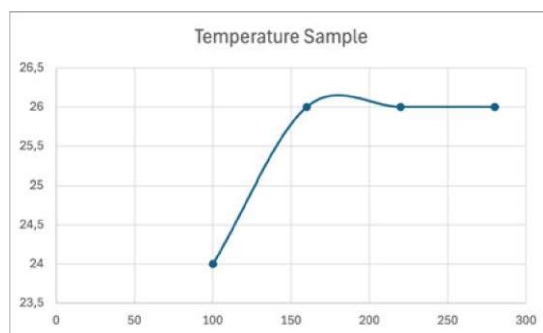


(d)

Figure A.1.: Sample temperatures measured for the experiments with L2V and pMHC. Temperatures were measured every five seconds by Tokai-HIT.



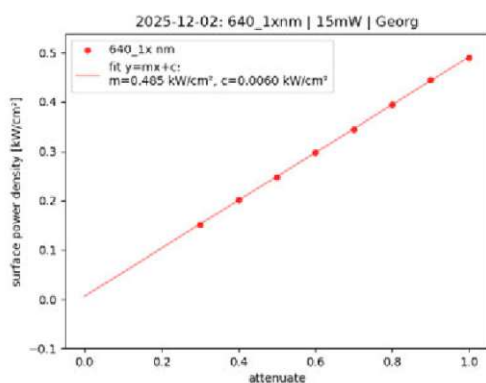
(a)



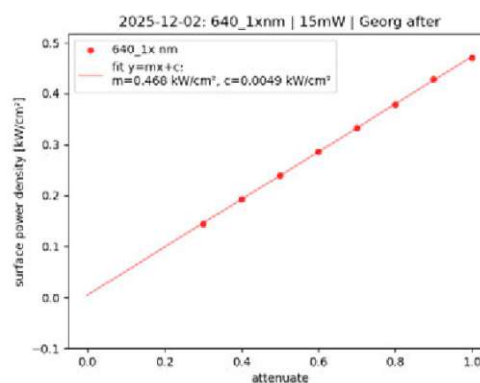
(b)

Figure A.2.: Sample temperatures measured for the experiments with L1V. Temperatures were manually measured before every imaging datapoint.

## A.2. Laser Power Plots

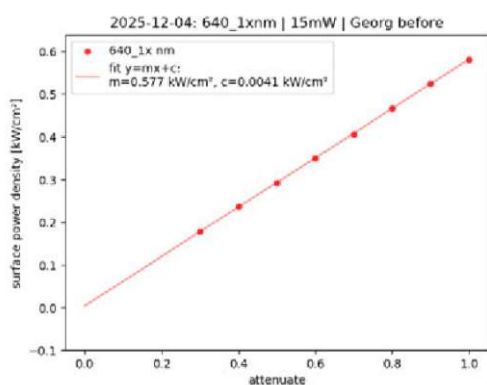


(a)

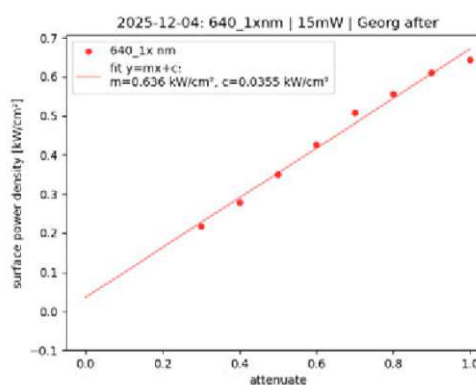


(b)

Figure A.3.: Surface power density of laser light in relation to the attenuate at the 02.12.2025.



(a)



(b)

Figure A.4.: Surface power density of laser light in relation to the attenuation at the 04.12.2025.

## A.3. Mean Single-Molecule Brightness Tables

### A.3.1. 26 Degrees

#### L2V

Date	Frames	imaged positions	Well	Seeding	$t_n$	$\Delta t$ (min)	Mean brightness (a.u.)	SEM (a.u.)	Mean background (a.u.)
02.10	90-99	10	SLB1	20ng	$t_0$	120	3530.36	216.46	258.89
02.10	90-99	10	SLB1	20ng	$t_1$	190	2921.92	124.24	257.77
02.10	90-99	10	SLB1	20ng	$t_2$	250	3543.02	671.43	254.36
02.10	90-99	10	SLB2	20ng	$t_0$	120	3526.22	185.61	261.54
02.10	90-99	10	SLB2	20ng	$t_1$	190	2948.98	108.68	264.85
02.10	90-99	10	SLB2	20ng	$t_2$	250	3840.80	97.63	263.73
09.10	90-99	10	SLB1	20ng	$t_0$	40	7642.22	1078.36	290.10
09.10	90-99	10	SLB1	20ng	$t_1$	110	4703.53	1075.29	274.35
09.10	90-99	10	SLB1	20ng	$t_2$	180	8969.88	478.51	268.18
09.10	90-99	10	SLB1	20ng	$t_3$	250	4176.45	1399.36	291.71
09.10	90-99	10	SLB2	20ng	$t_0$	50	7329.93	874.97	288.01
09.10	90-99	10	SLB2	20ng	$t_1$	110	6469.31	523.51	287.64
09.10	90-99	10	SLB2	20ng	$t_2$	180	7401.35	615.69	284.34
09.10	90-99	10	SLB2	20ng	$t_3$	250	6789.89	891.80	288.60

Table A.1.: Mean single-molecule brightness values for L2V at 26 °C. Values are reported as mean  $\pm$  SEM across localizations per time point.  $\Delta t$  is reported since last wash. Background denotes the mean local background intensity extracted per localization.

## L1V

Date	Frames	imaged positions	Well	Seeding	$t_n$	$\Delta t$ (min)	Mean brightness (a.u.)	SEM (a.u.)	Mean background (a.u.)
04.12	0-99	10	SLB1	20ng	$t_0$	100	10701.10	320.94	316.24
04.12	0-99	10	SLB1	20ng	$t_1$	160	9757.14	209.85	319.34
04.12	0-99	10	SLB1	20ng	$t_2$	220	8074.19	72.37	327.04
04.12	0-99	10	SLB1	20ng	$t_3$	280	11456.81	170.16	296.94
04.12	0-99	10	SLB2	20ng	$t_0$	100	8512.36	198.89	328.73
04.12	0-99	10	SLB2	20ng	$t_1$	170	11300.72	396.42	300.10
04.12	0-99	10	SLB2	20ng	$t_2$	220	9765.63	111.46	313.93
04.12	0-99	10	SLB2	20ng	$t_3$	280	8881.86	473.90	323.17

Table A.2.: **Mean single-molecule brightness values for L1V at 26 °C.** Values are reported as mean  $\pm$  SEM across localizations per time point.  $\Delta t$  is reported since last wash. Background denotes the mean local background intensity extracted per localization.

## pMHC

Date	Frames	imaged positions	Well	Seeding	$t_n$	$\Delta t$ (min)	Mean brightness (a.u.)	SEM (a.u.)	Mean background (a.u.)
02.10	90-99	10	SLB1	20ng	$t_0$	130	3829.88	78.31	277.74
02.10	90-99	10	SLB1	20ng	$t_1$	210	3656.29	64.36	273.92
02.10	90-99	10	SLB1	20ng	$t_2$	260	3727.77	242.14	276.31
02.10	90-99	10	SLB2	20ng	$t_0$	130	4115.98	125.85	271.31
02.10	90-99	10	SLB2	20ng	$t_1$	210	3622.79	121.87	270.26
02.10	90-99	10	SLB2	20ng	$t_2$	260	3872.92	70.60	266.23
09.10	90-99	10	SLB1	10ng	$t_0$	60	4286.73	710.17	287.21
09.10	90-99	10	SLB1	10ng	$t_1$	120	5199.05	736.03	278.04
09.10	90-99	10	SLB1	10ng	$t_2$	190	4246.61	413.69	281.28
09.10	90-99	10	SLB1	10ng	$t_3$	260	5280.72	528.81	281.78
09.10	90-99	10	SLB2	10ng	$t_0$	60	4550.64	458.51	288.99
09.10	90-99	10	SLB2	10ng	$t_1$	120	5473.61	383.34	283.61
09.10	90-99	10	SLB2	10ng	$t_2$	190	5444.89	503.71	280.98
09.10	90-99	10	SLB2	10ng	$t_3$	270	4738.71	344.02	292.36

Table A.3.: **Mean single-molecule brightness values for pMHC at 26 °C.** Values are reported as mean  $\pm$  SEM across localizations per time point.  $\Delta t$  is reported since last wash. Background denotes the mean local background intensity extracted per localization.

## A.3.2. 37 Degrees

### L2V

Date	Frames	imaged positions	Well	Seeding	$t_n$	$\Delta t$ (min)	Mean brightness (a.u.)	SEM (a.u.)	Mean background (a.u.)
03.10	90-99	10	SLB1	20ng	$t_0$	50	2592.00	191.72	257.28
03.10	90-99	10	SLB1	20ng	$t_1$	100	2669.05	178.09	260.51
03.10	90-99	10	SLB1	20ng	$t_2$	160	1787.34	83.07	259.13
03.10	90-99	10	SLB2	20ng	$t_0$	50	3146.22	286.74	257.95
03.10	90-99	10	SLB2	20ng	$t_1$	100	2843.45	98.06	257.64
03.10	90-99	10	SLB2	20ng	$t_2$	160	2018.27	79.00	257.75
10.10	90-99	10	SLB1	20ng	$t_0$	70	2636.43	544.49	274.05
10.10	90-99	10	SLB1	20ng	$t_1$	130	2358.89	281.84	271.88
10.10	90-99	10	SLB1	20ng	$t_2$	180	2711.14	624.66	267.02
10.10	90-99	10	SLB1	20ng	$t_3$	240	3217.28	1037.12	269.22
10.10	90-99	10	SLB2	20ng	$t_0$	80	2948.29	402.94	275.06
10.10	90-99	10	SLB2	20ng	$t_1$	130	2973.18	275.21	283.20
10.10	90-99	10	SLB2	20ng	$t_2$	180	4213.54	356.41	277.31
10.10	90-99	10	SLB2	20ng	$t_3$	240	2171.49	499.71	265.97

Table A.4.: **Mean single-molecule brightness values for L2V at 37 °C.** Values are reported as mean  $\pm$  SEM across localizations per time point.  $\Delta t$  is reported since last wash. Background denotes the mean local background intensity extracted per localization.

### L1V

Date	Frames	imaged positions	Well	Seeding	$t_n$	$\Delta t$ (min)	Mean brightness (a.u.)	SEM (a.u.)	Mean background (a.u.)
03.10	0-99	10	SLB1	20ng	$t_0$	170	1944.77	112.37	254.63
03.10	0-99	10	SLB1	20ng	$t_1$	250	2009.15	83.41	255.86
03.10	0-99	10	SLB1	20ng	$t_2$	280	2170.16	110.80	254.95
03.10	0-99	10	SLB1	20ng	$t_3$	320	1612.74	76.75	253.95
03.10	0-99	10	SLB2	20ng	$t_0$	180	2107.27	107.42	246.47
03.10	0-99	10	SLB2	20ng	$t_1$	250	1492.14	106.93	243.68
03.10	0-99	10	SLB2	20ng	$t_2$	280	2182.63	243.94	247.89
03.10	0-99	10	SLB2	20ng	$t_3$	350	1995.70	433.88	240.75

Table A.5.: **Mean single-molecule brightness values for L1V at 37 °C.** Values are reported as mean  $\pm$  SEM across localizations per time point.  $\Delta t$  is reported since last wash. Background denotes the mean local background intensity extracted per localization.

## pMHC

Date	Frames	imaged positions	Well	Seeding	$t_n$	$\Delta t$ (min)	Mean brightness (a.u.)	SEM (a.u.)	Mean background (a.u.)
03.10	90-99	10	SLB1	10ng	$t_0$	50	2943.20	229.98	261.34
03.10	90-99	10	SLB1	10ng	$t_1$	180	2992.60	222.22	261.48
03.10	90-99	10	SLB2	10ng	$t_0$	60	2168.27	80.70	261.52
03.10	90-99	10	SLB2	10ng	$t_1$	140	3006.40	164.11	258.24
03.10	90-99	10	SLB2	10ng	$t_2$	180	2774.44	320.82	256.24
10.10	90-99	10	SLB1	10ng	$t_0$	100	2533.16	230.76	281.48
10.10	90-99	10	SLB1	10ng	$t_1$	150	2196.88	421.20	269.49
10.10	90-99	10	SLB1	10ng	$t_2$	190	3200.93	309.97	276.57
10.10	90-99	10	SLB1	10ng	$t_3$	260	4093.96	550.14	271.56
10.10	90-99	10	SLB2	10ng	$t_0$	110	4737.54	470.75	276.50
10.10	90-99	10	SLB2	10ng	$t_1$	150	2747.12	546.67	271.31
10.10	90-99	10	SLB2	10ng	$t_2$	200	2561.65	525.96	279.28
10.10	90-99	10	SLB2	10ng	$t_3$	260	2612.05	416.58	269.24

Table A.6.: Mean single-molecule brightness values for pMHC at 37 °C. Values are reported as mean  $\pm$  SEM across localizations per time point.  $\Delta t$  is reported since last wash. Background denotes the mean local background intensity extracted per localization.

## A.4. DNA Origami Mixing Tables

### A.4.1. L2V

Table A.7.: DNA origami mixing platform L2V

Components	DNA strands	Amount [ $\mu$ L]	Final concentration
Scaffold	–	30	30 nM
FoB	–	10	1x
MgCl <sub>2</sub>	–	1.25	12.5 mM
Mastemix	134	40.2	300 nM/strand
Top mix - L2	34	10,2	300 nM/strand
X' mix	6	1.8	300 nM/strand
Z' mix	8	2.4	300 nM/strand
V'V'_L2(#17, #19)	2	0.6	300 nM/strand
V_AF647	2	1.5	750 nM/strand
UP H <sub>2</sub> O	–	2.05	
Total volume	–	100	

## A.4.2. L1V

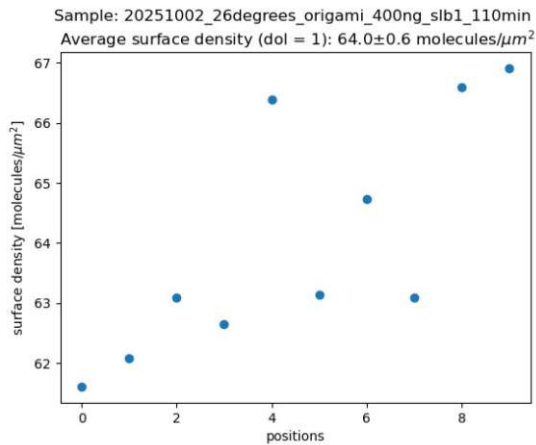
Table A.8.: DNA origami mixing platform L1V

Components	DNA strands	Amount [ $\mu\text{L}$ ]	Final concentration
Scaffold	–	30	30 nM
FoB	–	10	1x
MgCl <sub>2</sub>	–	1.25	12.5 mM
Mastemix	134	40.2	100 nM/strand
Top mix - L1	35	10,5	300 nM/strand
X' mix	6	1.8	300 nM/strand
Z' mix	8	2.4	300 nM/strand
V'V'_L1(#25)	1	0.3	300 nM/strand
V_AF647	1	0.75	750 nM/strand
UP H <sub>2</sub> O	–	2.8	
Total volume	–	100	

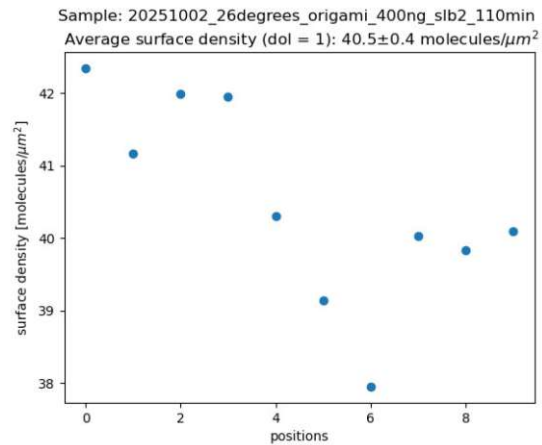
## A.5. Surface Density Plots at $t(0)$

### A.5.1. 26 Degrees

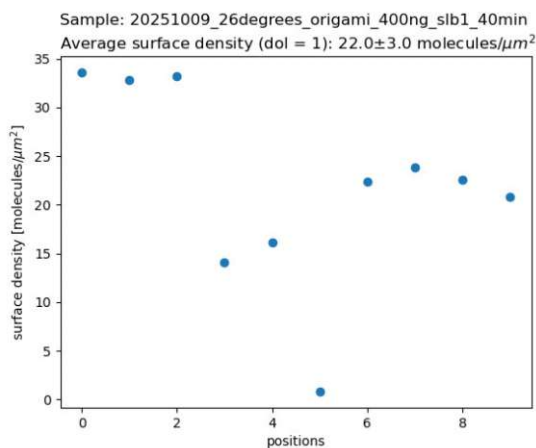
#### L2V



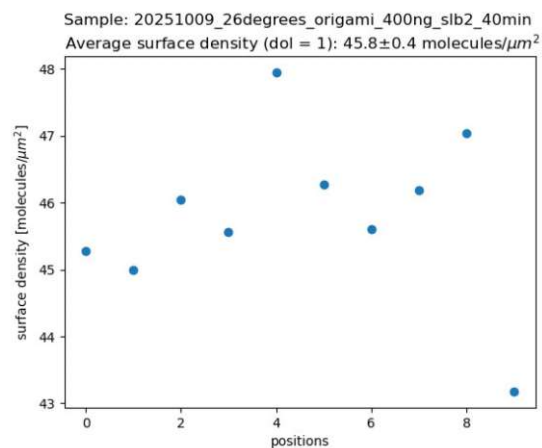
(a) SLB 1, 02/10.  $t_0$  at 110 min



(b) SLB 2, 02/10.  $t_0$  at 110 min



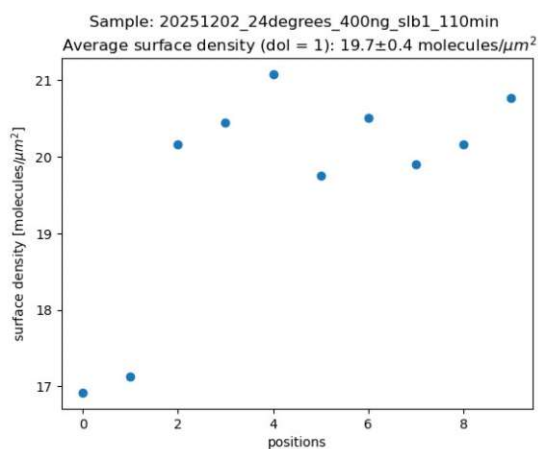
(c) SLB 1, 09/10.  $t_0$  at 40 min



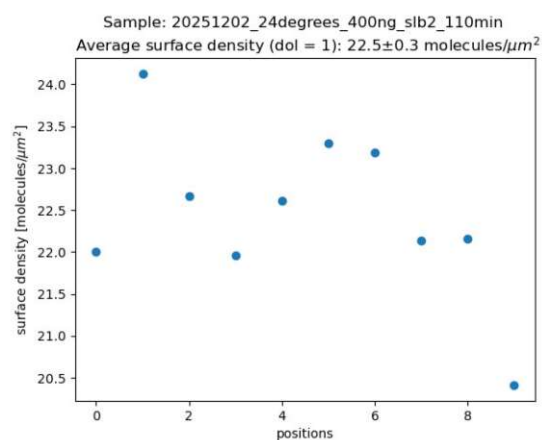
(d) SLB 2, 09/10.  $t_0$  at 40 min

Figure A.5.: Estimated initial surface density  $\rho(t_0)$  for L2V bulk fluorescence wells at 26 °C across imaged positions. Surface densities were calculated from the background-corrected bulk intensity at  $t_0$  divided by the corresponding single-molecule brightness at  $t_0$  (Eq. 3.4).

## L1V



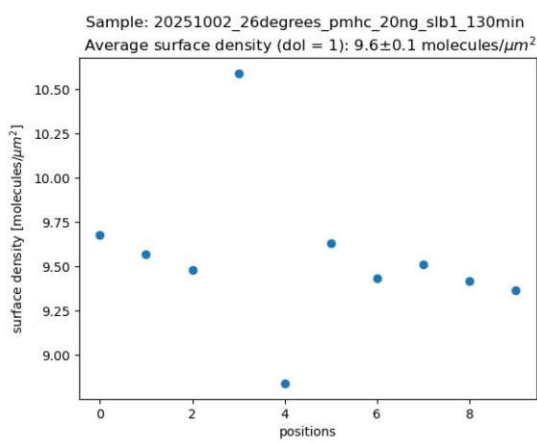
(a) SLB 1, 02/12.  $t_0$  at 110 min



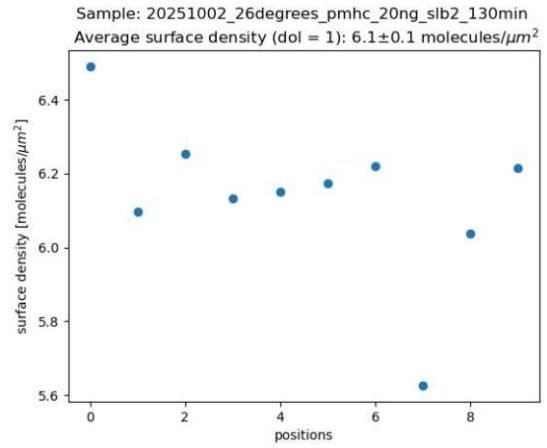
(b) SLB 2, 02/12.  $t_0$  at 110 min

Figure A.6.: **Estimated initial surface density  $\rho(t_0)$  for L1V bulk fluorescence wells at 26 °C across imaged positions.** Surface densities were calculated from the background-corrected bulk intensity at  $t_0$  divided by the corresponding single-molecule brightness at  $t_0$  (Eq. 3.4).

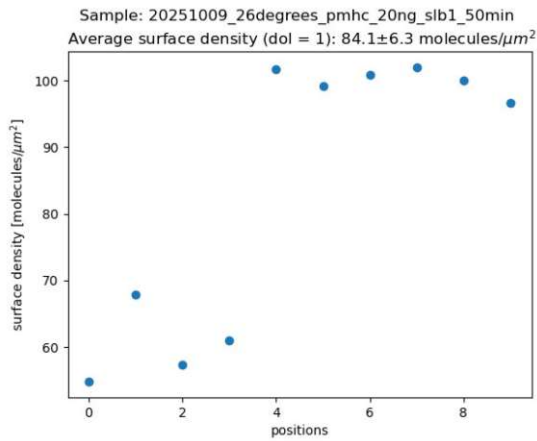
## pMHC



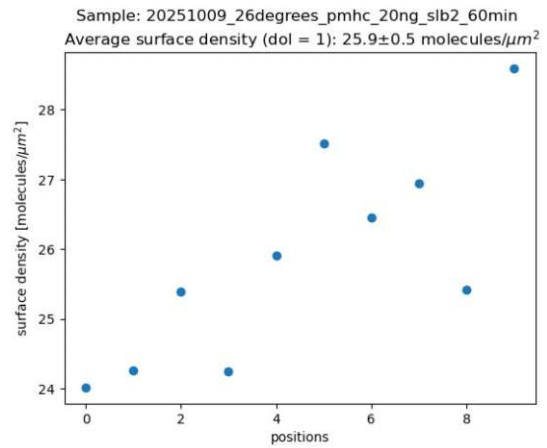
(a) SLB 1, 02/10.  $t_0$  at 130 min



(b) SLB 2, 02/10.  $t_0$  at 130 min



(c) SLB 1, 09/10.  $t_0$  at 50 min

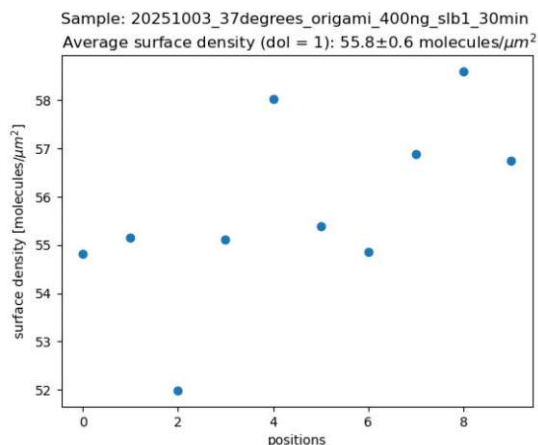


(d) SLB 2, 09/10.  $t_0$  at 60 min

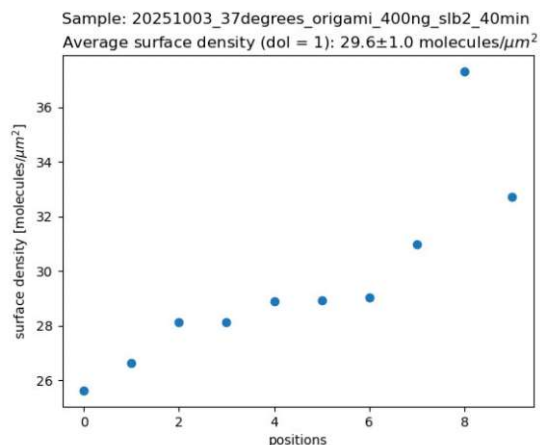
Figure A.7.: **Estimated initial surface density  $\rho(t_0)$  for pMHC bulk fluorescence wells at 26 °C across imaged positions.** Surface densities were calculated from the background-corrected bulk intensity at  $t_0$  divided by the corresponding single-molecule brightness at  $t_0$  (Eq. 3.4).

## A.5.2. 37 Degrees

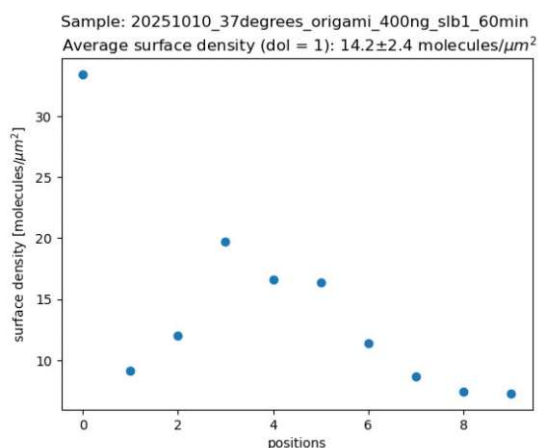
### L2V



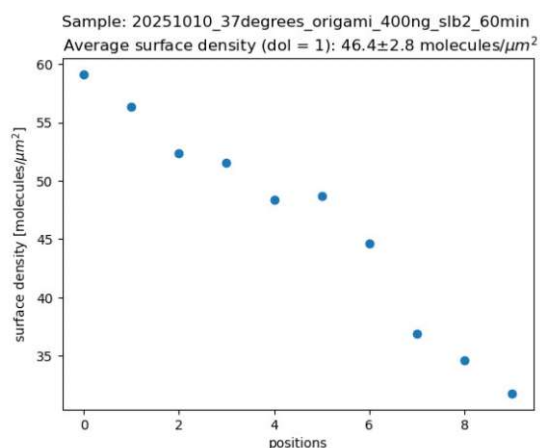
(a) SLB 1, 03/10.  $t_0$  at 30 min



(b) SLB 2, 03/10.  $t_0$  at 40 min



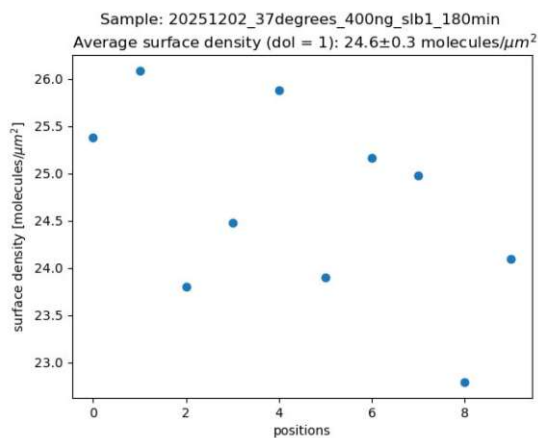
(c) SLB 1, 10/10.  $t_0$  at 60 min



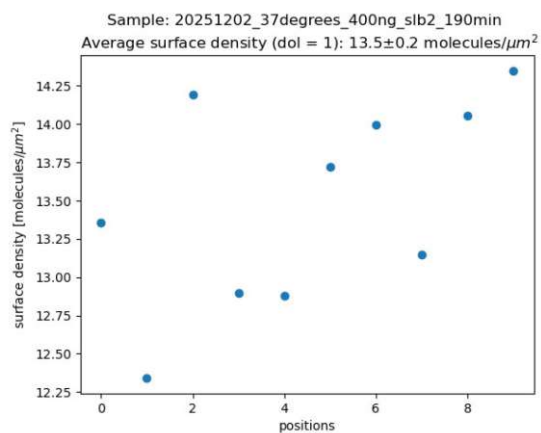
(d) SLB 2, 10/10.  $t_0$  at 60 min

Figure A.8.: **Estimated initial surface density  $\rho(t_0)$  for L2V bulk fluorescence wells at  $37^\circ\text{C}$  across imaged positions.** Surface densities were calculated from the background-corrected bulk intensity at  $t_0$  divided by the corresponding single-molecule brightness at  $t_0$  (Eq. 3.4).

## L1V



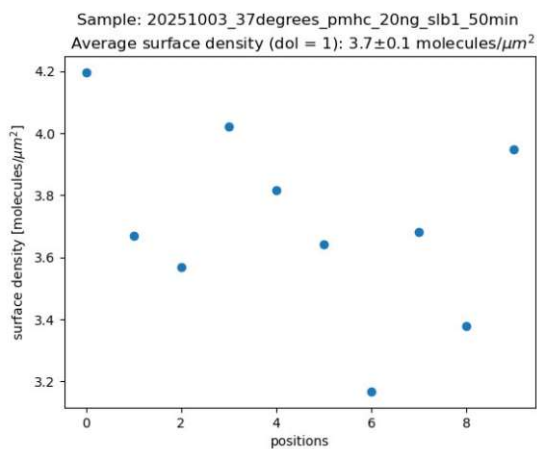
(a) SLB 1, 02/12.  $t_0$  at 180 min



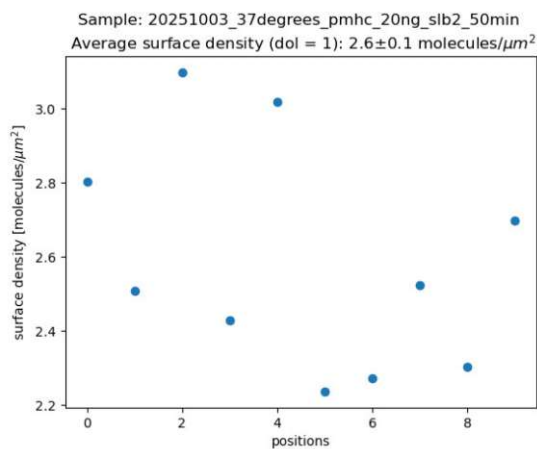
(b) SLB 2, 02/12.  $t_0$  at 190 min

Figure A.9.: **Estimated initial surface density  $\rho(t_0)$  for L1V bulk fluorescence wells at  $37^\circ\text{C}$  across imaged positions.** Surface densities were calculated from the background-corrected bulk intensity at  $t_0$  divided by the corresponding single-molecule brightness at  $t_0$  (Eq. 3.4).

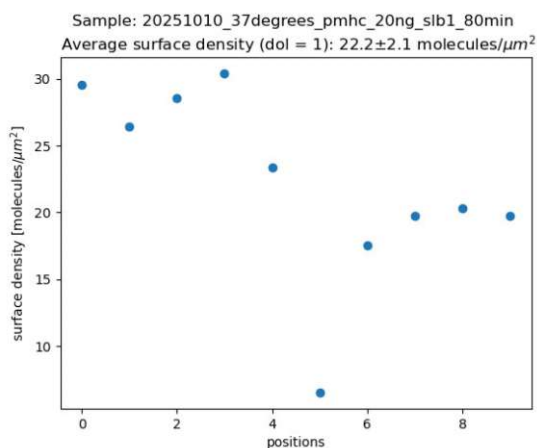
### A.5.3. pMHC



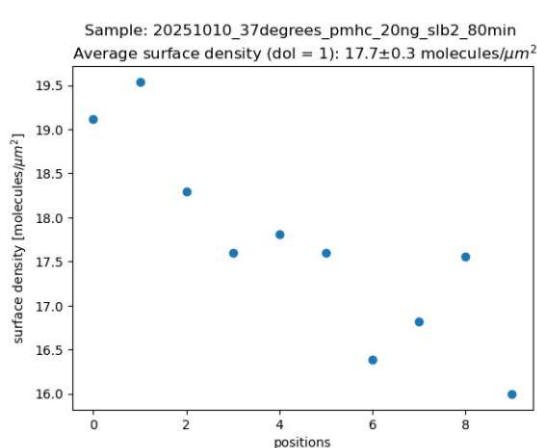
(a) SLB 1, 03/10.  $t_0$  at 50 min



(b) SLB 2, 03/10.  $t_0$  at 50 min



(c) SLB 1, 10/10.  $t_0$  at 80 min



(d) SLB 2, 10/10.  $t_0$  at 80 min

Figure A.10.: **Estimated initial surface density  $\rho(t_0)$  for pMHC bulk fluorescence wells at  $37^\circ\text{C}$  across imaged positions.** Surface densities were calculated from the background-corrected bulk intensity at  $t_0$  divided by the corresponding single-molecule brightness at  $t_0$  (Eq. 3.4).

## B. Use of AI

During the preparation of this thesis, generative artificial intelligence (in particular ChatGPT 5.2) tools were used as a writing aid to improve the linguistic quality of the manuscript. In particular, AI was employed to rephrase sentences, reduce redundancy, and enhance coherence and readability across paragraphs and sections. The scientific content, interpretation of results, selection of literature, and all conclusions were developed by the author. AI assistance was not used to generate or manipulate experimental data, nor to produce figures or statistical analyses. All text suggestions produced with AI were reviewed, edited, and verified by the author before inclusion in the final manuscript.